UNIVERSITY OF CALIFORNIA SAN DIEGO

Coupling of Photonic Resonances with Excitons in 2D Semiconductors for Enhanced Light-matter Interaction

A dissertation submitted in partial satisfaction of the requirements for the degree Doctor of Philosophy

in

Electrical Engineering (Photonics)

by

Wenzhuo Huang

Committee in charge:

Professor Ertugrul Cubukcu, Chair
Professor Zhaowei Liu, Co-Chair
Professor George C. Papen
Professor Daniel F. Sievenpiper
Professor Donald James Sirbuly

2022

The Dissertation of Wenzhuo Huang is approved, and it is acceptable in quality and form for publication on microfilm and electronically.

University of California San Diego

2022

DEDICATION

To my wife and our daughter.

EPIGRAPH

The eternal mystery of the world is its comprehensibility ...
The fact that it is comprehensible is a miracle.

– Albert Einstein

TABLE OF CONTENTS

LIST OF FIGURES

LIST OF TABLES

ACKNOWLEDGEMENTS

First of all, I would like to express my greatest gratitude to my advisor, Professor Ertugrul Cubukcu, for his support and guidance over the years of my graduate career. Not only does he share with me his broad knowledge and physics intuition, but he also constantly performs hands-on instruction in the lab. The most important lesson I learned from him is to think critically and get hands dirty. Besides research, he is also nice and considerate in everyday life. He has been a great model to me as a researcher, scientist and father. I would also like to thank other members of my committee: Prof. Zhaowei Liu, Prof. George Papen, Prof. Daniel Sievenpiper and Prof. Donald Sirbuly as well as my preliminary exam committee member Prof. Boubacar Kanté for their time and support. I have been making myself better from their courses and conversations with them.

I would like to thank my labmate Chawina De-Eknamkul, who will also become a doctor soon, for all the samples she made for me that took her hundreds of hours if not more. She is such a great coworker and friend, who is always ready to help and share ideas. My works wouldn't be possible without her invaluable efforts. I would like to thank Prof. A. T. Charlie Johnson, Prof. Duygu Kuzum, Eric Leewong, Dr. Yundong Ren, Prof. Sefaattin Tongay, Dr. Kedi Wu, Prof. Fei Yi, Xiaojie Zhang, Dr. Xingwang Zhang, Prof. Mengqiang Zhao, and all other collaborators and former group members for their contribution in this dissertation.

I would like to thank Jeonghoon Kim, Sangheon Oh, Zunming Zhang and other colleagues for their help during the work. I would like to thank Dr. Hongye Hu, Zhetao Jia, Dr. Qitong Li, Dr. Yifei Wang, Dr. Lin Xiong, Dr. Yifei Zhang, Dr. Hengyun Zhou and other friends for the insightful discussions. I would also like to acknowledge the staffs in Electrical

and Computer Engineering department, NanoEngineering department, nano3 cleanroom and graduate division at UCSD for their assistance from admission to graduation of my PhD program.

Last but not least, I would like to thank my family, especially my wife Yuwei Li for respecting my every single decision and supporting me in everyday life. Without their help and encouragement, I cannot go this far. I met Yuwei in this beautiful campus, proposed to her using a microscale pattern (shout out to Chawina for her help in fabricating this special sample) that was seen by projection through a homemade microscopic system. And, while I am writing this dissertation, she brought a new family member Journee Zhiying Huang to life, making our life journey more worthwhile. This work is for them.

Chapter 4, in full, is a reprint of the material as it appears in ACS Photonics, 2019, with title "Monolayer excitonic emission for imaging spatial dispersion of photonic crystals", by Wenzhuo Huang, Chawina De-Eknamkul, Xingwang Zhang, Eric Leewong, Meng-Qiang Zhao, AT Charlie Johnson, and Ertugrul Cubukcu. The dissertation author was the primary investigator and author of this paper.

Chapter 5, in full, is currently being prepared for submission for publication of the material with title "Direct observation of polarization vortex on exceptional ring using WS_2 photoluminescence", by Wenzhuo Huang, Chawina De-Eknamkul, and Ertugrul Cubukcu. The dissertation author was the primary investigator and author of this paper.

Chapter 6, in full, is currently being prepared for submission for publication of the material with title "Directing valley-polarized emission of 3L WS_2 by photonic crystal with directional circular dichroism", by Wenzhuo Huang, Chawina De-Eknamkul, and Ertugrul

Cubukcu. The dissertation author was the primary investigator and author of this paper.

Chapter 7, in part, is currently being prepared for submission for publication of the material with title "Directional propagation of self-resonant exciton-polariton in atomically thin WS_2 waveguide", by Chawina De-Eknamkul, Wenzhuo Huang, Xingwang Zhang, and Ertugrul Cubukcu. The dissertation author was the co-investigator and co-author of this paper. Chapter 7, in part, is a reprint of the material as it appears in Advanced Optical Materials, 2020, with title "Ultrathin WS_2-on-glass photonic crystal for self-resonant exciton-polaritonics", by Xingwang Zhang, Xiaojie Zhang, Wenzhuo Huang, Kedi Wu, Mengqiang Zhao, A. T. Charlie Johnson, Sefaattin Tongay, and Ertugrul Cubukcu. The dissertation author was the co-investigator and co-author of this paper.

Wenzhuo Huang

La Jolla, CA

VITA

2016 Bachelor of Science, Peking University

2018 Master of Science, University of California San Diego

2022 Doctor of Philosophy, University of California San Diego

PUBLICATIONS

Chawina De-Eknamkul, Jeonghoon Kim, **Wenzhuo Huang**, Yundong Ren, Madison Wilson, Francesca Puppo, Meena Patne, Alysson R. Muotri, Duygu Kuzum, and Ertugrul Cubukcu. Optical voltage sensing of electrophysiological signals with monolayer MoS_2. *In preparation*, 2022

Wenzhuo Huang, Chawina De-Eknamkul, and Ertugrul Cubukcu. Directing valley-polarized emission of 3L WS_2 by photonic crystal with directional circular dichroism. *In manuscript*, 2022

Chawina De-Eknamkul, **Wenzhuo Huang**, Xingwang Zhang, and Ertugrul Cubukcu. Directional propagation of self-resonant exciton-polariton in atomically thin WS_2 waveguide. *In manuscript*, 2022

Wenzhuo Huang, Chawina De-Eknamkul, and Ertugrul Cubukcu. Direct observation of polarization vortex on exceptional ring using WS_2 photoluminescence. *In manuscript*, 2022

Xingwang Zhang, **Wenzhuo Huang**, Chawina De-Eknamkul, Kedi Wu, Meng-qiang Zhao, Sefaattin Tongay, Alan T Charlie Johnson, and Ertugrul Cubukcu. Azimuthally polarized and unidirectional excitonic emission from deep subwavelength transition metal dichalcogenide annular heterostructures. *ACS Photonics*, 8(10):2861–2867, 2021

Xingwang Zhang, Xiaojie Zhang, **Wenzhuo Huang**, Kedi Wu, Mengqiang Zhao, AT Charlie Johnson, Sefaattin Tongay, and Ertugrul Cubukcu. Ultrathin WS_2-on-glass photonic crystal for self-resonant exciton-polaritonics. *Advanced Optical Materials*, 8(7):1901988, 2020

Wenzhuo Huang, Chawina De-Eknamkul, Xingwang Zhang, Eric Leewong, Meng-Qiang Zhao, AT Charlie Johnson, and Ertugrul Cubukcu. Monolayer excitonic emission for imaging spatial dispersion of photonic crystals. *ACS Photonics*, 6(9):2312–2319, 2019

Chawina De-Eknamkul, Xingwang Zhang, Meng-Qiang Zhao, **Wenzhuo Huang**, Renyu Liu, AT Charlie Johnson, and Ertugrul Cubukcu. MoS_2-enabled dual-mode optoelectronic

biosensor using a water soluble variant of μ-opioid receptor for opioid peptide detection. *2D Materials*, 7(1):014004, 2019

Xingwang Zhang, Nicolas Biekert, Shinhyuk Choi, Carl H Naylor, Chawina De-Eknamkul, **Wenzhuo Huang**, Xiaojie Zhang, Xiaorui Zheng, Dake Wang, AT Charlie Johnson, and Ertugrul Cubukcu. Dynamic photochemical and optoelectronic control of photonic Fano resonances via monolayer MoS_2 trions. *Nano Letters*, 18(2):957–963, 2018

CONFERENCE PROCEEDINGS

Xingwang Zhang, Nicolas Biekert, Shinhyuk Choi, Carl H Naylor, Chawina De-Eknamkul, **Wenzhuo Huang**, Xiaorui Zheng, Dake Wang, AT Charlie Johnson, and Ertugrul Cubukcu. Coupling of photonic Fano resonances with MoS_2 excitons for enhanced light emission and optical modulation. In *2018 Conference on Lasers and Electro-Optics (CLEO)*, pages 1–2. IEEE, 2018

PRE-DOCTORAL PUBLICATIONS

Wenzhuo Huang, Jing Yang, Xiao Xiao, and Jiasen Zhang. Surface plasmon polariton unidirectional nano-launcher based on the strong coupling effects in an asymmetric optical slot nanoantenna pair. *Plasmonics*, 10(6):1551–1556, 2015

ABSTRACT OF THE DISSERTATION

Coupling of Photonic Resonances with Excitons in 2D Semiconductors
for Enhanced Light-matter Interaction

by

Wenzhuo Huang

Doctor of Philosophy in Electrical Engineering (Photonics)

University of California San Diego, 2022

Professor Ertugrul Cubukcu, Chair
Professor Zhaowei Liu, Co-Chair

Semiconductor being the cornerstone of modern technology, has played an indispensable role in electronic and photonic devices that are widely used in both industry and commerce. Recent decades have witnessed the emergence of its two-dimensional (2D) form, i.e. monolayer or few-layer, which was found to exhibit several extraordinary properties than its bulk counterpart owing to quantum confinement. On the one hand, atomically thin semiconductors have reduced dielectric screening effect that increases the band gap and

exciton binding energy, resulting in excitonic emission and absorption in the visible spectrum. Because of the strong electron-hole interaction, they are attractive candidates for optoelectronic applications such as sensors, modulators, solar cells and light emitters. On the other hand, 2D semiconductors as layered crystals offer a superb platform for stacked heterostructures that feature interlayer interactions and more intriguing physics if twisted at an angle. The lack of spatial inversion symmetry in their crystals also opens up valley degree of freedom, offering tremendous opportunities for future information processing devices. However, due to their ultra-thin thickness by nature, conventional photonic devices that function well with bulk semiconductors may not apply to these layered atoms. In this dissertation, by integrating 2D semiconductors with optical resonators, specifically photonic crystals, a substantial spatial overlap between the material and delocalized photonic resonances is achieved. The light-matter interaction is enhanced by increased excitation rate and Purcell effect; in the strong coupling regime, the interaction results in the formation of exciton-polariton, a half-light, half-matter quasiparticle. The interaction between valley-polarized excitons and polarization dependent guided resonances also enables possible valleytronic applications. Through these enhanced light-matter interactions, we are able to manipulate the light emission, absorption and scattering properties in the TMDC-based devices. We believe that these studies can help unveil the unprecedented potential of 2D semiconductors and propel them forward to next-generation photonic and optoelectronic devices with reduced sizes, improved efficiency and advanced functionality.

Part I

Introduction and Background

Chapter 1

Introduction

1.1 Introduction

In 2004, Andre Geim and Konstantin Novoselov at the University of Manchester reported the exfoliation of graphene, a single layer of carbon atoms in honeycomb lattice, from a graphite crystal using an adhesive tape [12]. They were awarded the Nobel Prize in Physics for their ”groundbreaking experiments regarding the two-dimensional material graphene”. Since then, two dimensional (2D) materials have attracted enormous attention owning to their ultra thinness and immense physical implications that come along. Although graphene has Dirac cones [13] in its band structure which brings a lot of unique electronic properties, it's not suitable for semiconductor devices that require materials with intermediate-sized bandgaps.

Transition metal dichalcogenides (TMDCs), a class of 2D semiconductors with a hexagonal lattice, have experienced a rapid development because of the unprecedented electronic, optical and thermal properties they can offer. TMDCs have a chemical formula of MX_2, where M is a transition metal atom such as Molybdenum (Mo) and Tungsten (W) and X is a chalcogen atom such as sulfur (S) and Selenium (Se). They can be synthesized via chemical vapor deposition (CVD) method to produce a layered crystal with large area, which is

optimal for industrial usage; alternatively, monolayer or few-layer flakes can be mechanically exfoliated and transferred later for research purposes.

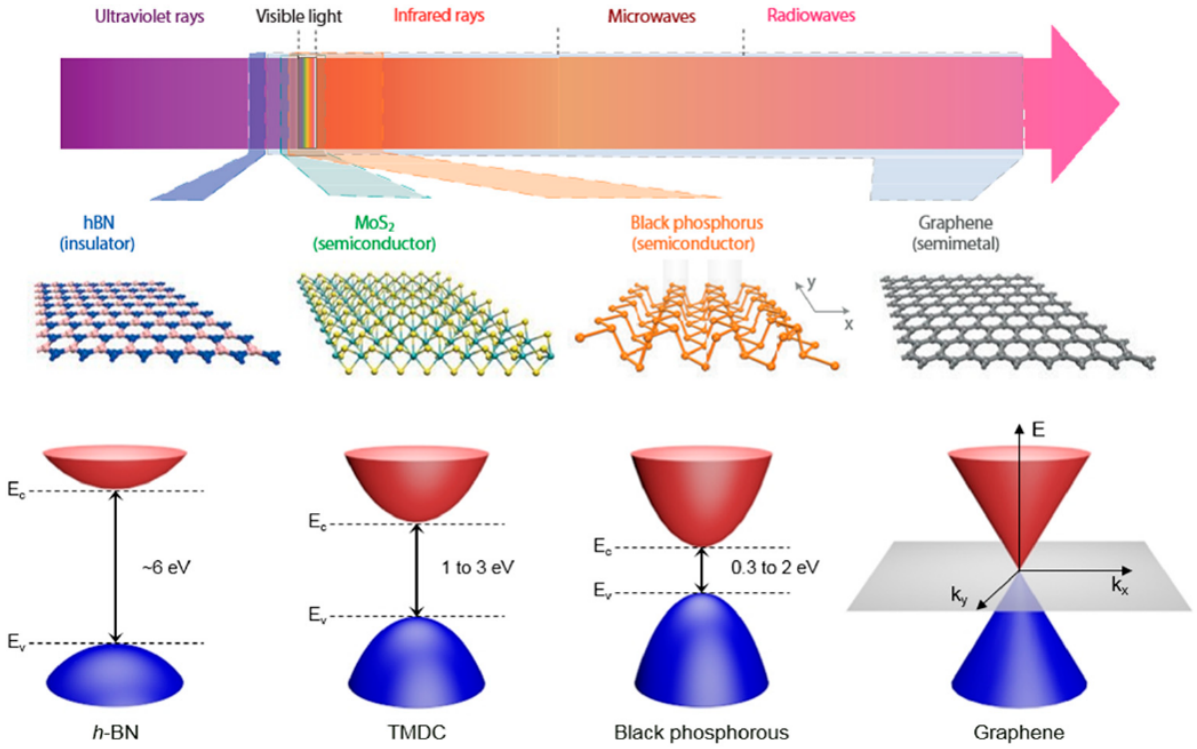

Figure 1.1. Energy spectrum and crystal structures of 2D materials with different electronic band gaps [14].

As TMDCs thin down to monolayers, their indirect bandgaps become energy-degenerate direct bandgaps at K and K' points in the Brillouin zone [15]. The direct bandgaps result in a substantially higher quantum yield (QY) in the monolayer TMDCs, leading to stronger photoluminescence (PL) than their few-layer counterparts [16, 17]. Because of quantum confinement and reduced dielectric screening, excitons in monolayer TMDCs have a strong binding energy that is few hundreds of meV at room temperature [18]. This strong excitonic resonance not only makes them excellent candidates for optoelectronic devices such as excitonic light emitters [19] and optical modulators [20, 21], but also allows them to incorporate with

optical resonators for the studies of exciton-polaritons [22, 23]. Moreover, broken inversion symmetry in monolayer TMDCs have open up the new valley degree of freedom [24], which leads to nonequivalent K and K' valleys with contrasting Berry curvatures and orbital magnetic moments. Because the strong spin-orbit coupling splits the valence bands, band edge electrons at one valley can only be stimulated by circularly polarized photons with corresponding helicity dictated by the optical selection rules. This optical control over the valley excitons plays an indispensable role for future valleytronic devices.

Despite 2D semiconductors, especially TMDCs, have shown such unparalleled advantages, their interaction with light is limited by the atomically thin structures. For example, 1L-MoS_2 only absorbs a little portion of pump beam in the visible range, and its PL is orders of magnitude weaker than that of dye molecules. The excitonic emission from 2D TMDCs can be treated as electric dipole radiation from in-plane emitters with random orientation, which shows poor directionality.

This limited light-matter interaction can be enhanced by incorporating 2D TMDCs with resonant photonic nanostructures, including but not limited to plasmonic nanoantenna (arrays) [25, 26], optical cavities [27, 28], Mie resonators [29, 30], metamaterials [31] and metasurfaces [32, 33, 34], and photonic crystals [35, 36, 37]. Leveraged by these photonic structures, light absorption, emission and scattering properties of 2D TMDCs are significantly improved. This leads to a wide variety of optoelectronic and photonic devices including sensors [38, 39, 40], photo-detectors [41, 42], light emitting diodes [43, 44] and excitonic lasers [45, 46, 47, 48]. Furthermore, the valley degree of freedom in 2D TMDCs can be addressed through photonic structures that response differently to valley pseudo-spin [49, 50, 51], which

provides tremendous opportunities for future valleytronic devices in quantum information. The light-matter interaction in the strong coupling regime gives rise to exciton-polaritons [52], which are of great interest for their physical implications in cavity quantum electrodynamics [53], Bose-Einstein condensates [54] and 2D superfluid behavior [55].

1.2 Motivation

Among all resonant photonic structures, photonic crystals (PhC) have been an ideal platform for enhancing light-matter interaction and manipulating radiation properties. As an optical analogy to solid state crystals, photonic crystals contain a periodic arrangement of unit cells with certain symmetry. Like its electronic counterpart, photonic crystals also support Bloch modes and thus have a band structure. Recent breakthroughs in photonic crystal systems have realized numerous concepts that originate from condensed matter physics, such as photonic topological insulator [56, 57, 58], quantum spin Hall effect [59, 60] and photonic valleytronics [61, 62, 63, 64].

Two dimensional PhC slab is the most common configuration as its finite thickness in vertical direction allows light coupling with the farfield. This makes guided modes in a PhC become farfield attainable guided mode resonances, if the frequency of the guided modes are above the light line. This inherent radiative loss makes PhC slabs a new playground for non-Hermitian physics [65, 66, 67] and bound states in continuum (BICs) [68, 69].

Therefore, by coupling guided mode resonances with excitonic resonances in 2D TMDCs, enhanced light-matter interaction can be realized in the multiple perspectives. First of all, these guided mode resonances have enhanced local field profile which not only boosts the

light absorption, but also increases the spontaneous emission rate of local emitters via Purcell effect. By aligning these resonances with the absorption and/or emission wavelengths, a huge PL enhancement can be achieved [70, 7]. Secondly, because these guided mode resonances feature asymmetric Fano lineshapes whose transmittance/reflectance drastically change within the resonance linewidth, they are suitable for sensor applications as the refractive indices of TMDCs are sensitive to the change of environment [9]. Thirdly, the scattering properties of guided mode resonances can be predicted by the photonic band structures and temporal coupled-mode theory (TCMT), which allow us to manipulate the emission angle and polarization states of the excitonic emission [4]. Notably, PhC slabs that are designed to support circularly polarized states can couple with valley-polarized excitons for valleytronic applications [71, 2]. Finally, 2D TMDCs as dielectric materials can also be made into photonic crystals, where the self-supported guided mode resonances strongly interact with the excitons [72, 3]. This leads to the emergence of self-resonant exciton-polaritons, whose out-of-plane confinement even exceeds that of surface plasmon polaritons [6].

1.3 Overview of this dissertation

The aim of this dissertation is to study the enhanced light-matter interaction from the coupling between photonic resonances and excitonic resonances. The dissertation is organized into three parts.

Part I provides an overview about the topics we will be studying as well as some background information about 2D TMDCs and photonic crystals. Our purpose of this part is to provide necessary information for the remainder of this dissertation, such as basic concepts

and our theoretical and experimental methodologies. The background about monolayer and few-layer transition dichalcogenides is covered in Chapter 2. It contains a review of each facet of the excitonic resonance and our general approaches for acquiring this information in our lab. Details about transfer matrix method and Kramers-Kronig relations are discussed in Appendix A. Chapter 3 is the background about photonic crystals and photonic crystal slabs. The vast majority of the photonic resonances we shall discuss later in this dissertation are the guided mode resonances supported by the photonic crystal slabs. This chapter discusses the approaches in optical simulation, and temporal coupled-mode theory for calculating Fano resonances. The detailed derivations for Fano resonances mentioned in chapters 5 and 6 are in the Appendix B.

Part II includes two papers about controlling excitonic emission from monolayer MoS_2 and WS_2. The first paper (chapter 4) illustrates the relation between photonic band structure of a PhC slab and the radiation properties of the integrated 1L-MoS_2, laying the groundwork for further studies. The second paper (chapter 5) is based on the first one by carefully tuning two photonic resonances into an accidental degeneracy that generates a so-called exceptional point. The excitonic emission is used to reveal the polarization vortex from a BIC which is encircled by a ring of exceptional points. The idea of this work is inspired by the recent advances in BIC, topological photonics and non-Hermitian physics. The dissertation author was the first author of both works.

Part III has two chapters on valleytronics and exciton-polaritonics in multi-layer WS_2. Chapter 6 proposes a PhC slab with broken inversion symmetry that emits circularly polarized light, which can separate valley-polarized excitonic emission from a 3L WS_2. The dissertation author is the first author of this work and a full reprint is used. Chapter 7 proposes self-resonant

exciton-polaritons in photonic crystals made out of a thin WS_2 flake on glass (section 7.2) and a suspended 3L WS_2 (section 7.3). The dissertation author was the co-author of both works and contributed mostly to the photonic simulations and the interpretation of the experimental results. These two works are partially used for the completeness of this dissertation.

Chapter 8 summarizes the dissertation and gives an outlook to future directions.

Appendices work as supplementary information to the concepts or methods mentioned in the main text. Appendix A demonstrates the Transfer Matrix Method and Kramers-Kronig relations, which are used to extract the refractive index of thin films on substrate. Appendix B elaborates on more variation from the temporal coupled-mode theory that is crucial for chapters 5 and 6. It includes the TCMT for a two-channel system and polarization analysis of radiative channels. Appendix C demonstrates the optical measurement techniques that are used throughout the dissertation, including confocal microscopy and angle resolved transmittance measurement.

Chapter 2

2D transition-metal dichalcogenides

2.1 Excitons in 2D TMDCs

In the bulk form, TMDCs are stacked layers of atoms held together by weak interlayer van der Waals forces [73]. When TMDCs transition from bulk to monolayer, the indirect bandgap becomes a direct bandgap at K points (Fig. 2.1a). This leads to enhanced quantum yield and stronger photoluminescence in the monolayer TMDCs than in the bulk. The monolayer or few-layer TMDCs can be obtained by mechanical exfoliation from a TMDC crystal due to the weak van der Waals interlayer interaction (Fig. 2.1b).

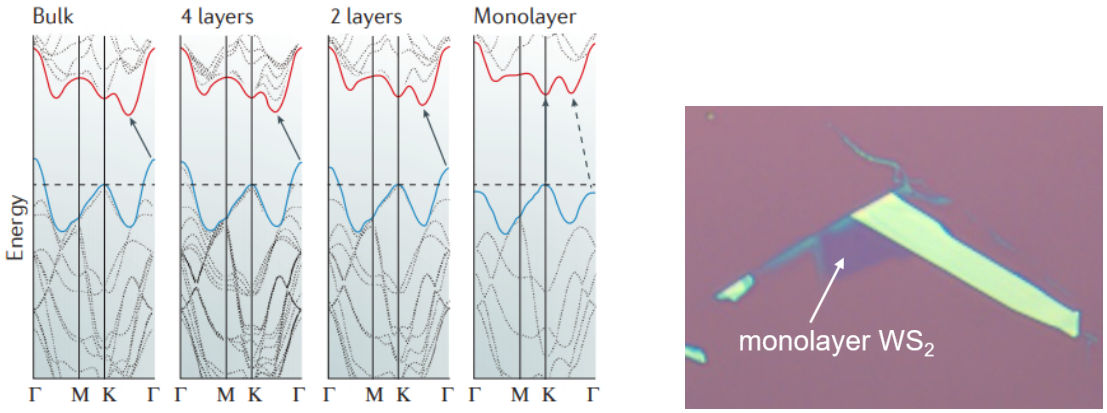

(a) **(b)**

Figure 2.1. (a) Transition of indirect bandgaps in bulk MoS_2 to a direct bandgap at monolayer (first principle calculation) [17]. (b) Mechanically exfoliated monolayer WS_2 in the lab.

The Coulomb attraction between electrons and holes gives rise to the formation of excitons, whose binding energy is much stronger than typical semiconductors (e.g. GaAs) due to the quantum confinement in the 2D TMDCs. This strong binding energy can be reflected through the large Lorentz oscillator strength in refractive index or a narrow emission linewidth. Hence, experimental measurements of refractive index and PL are of great importance in understanding the exciton behaviours in 2D TMDCs.

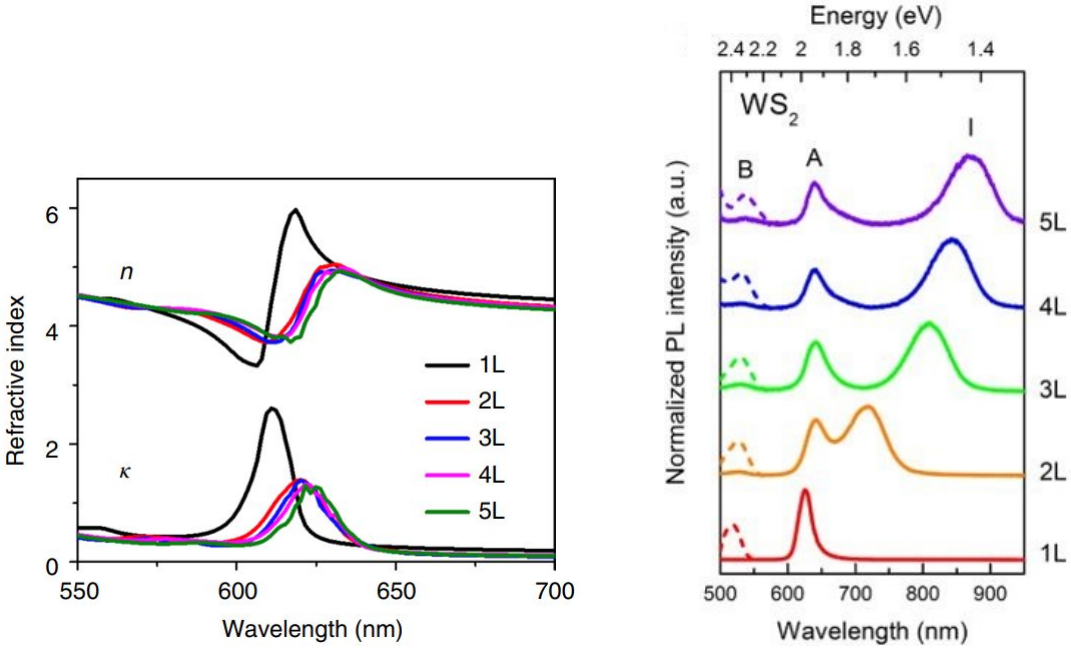

(a) **(b)**

Figure 2.2. (a) Measured real and imaginary parts of refractive indices of 1L to 5L WS_2 [74]. (b) Normalized PL spectra of mechanically exfoliated 1L to 5L WS_2 [75].

There are multiple ways to measure the complex refractive index of a thin film. For homogeneous, isotropic materials with infinite thickness, ellipsometry is the most straightforward technique to extract the index. When it comes to the atomically thin TMDCs,

the complex refractive index can be described by the Lorentz oscillator model

$$\widetilde{\varepsilon}_r(\omega) = \varepsilon_{\text{offset}} + \sum_n \frac{A_n}{\omega_n^2 - \omega^2 - i\gamma_n\omega} \tag{2.1}$$

where A_n, ω_n and γ_n are the strength, central frequency and width of the n^{th} oscillator, respectively. This model automatically guarantees the Kramers-Kronig relations. With measured reflectance, these oscillator parameters can be optimized to generate a calculated reflectance that has the minimum error compared to the measured one. The Transfer Matrix Method (TMM) can be used to calculate the reflectance of a layered structure.

For bulk TMDCs whose refractive index doesn't change with thickness, the refractive index can be extracted at every wavelength through reflectance measurement of multiple samples with known thickness. This is because the reflectance of the bulk TMDC on a substrate solely depends on the crystal's thickness and the complex refractive index. Given reflectance of TMDCs with at least two different thickness, the real and imaginary parts of the index can be regressed. Details about the extraction of complex refractive index are included in Appendix A.

2D TMDCs are also known for their strong spin-orbit coupling (SOC) that splits the valence band (the splitting of conduction band is much smaller, see Table 2.1). This large splitting distinguishes A and B excitons that correspond to lower and higher energy excitation, which can be visualized from the refractive index and the PL spectrum of the TMDCs (see Appendix A). Besides A and B excitons, there also exist charged excitons (trions), localized excitons associated with traps, dark intervalley excitons and other kinds of bound electron-hole states, all of which contribute to the high refractive index of 2D TMDCs.

	Valence band splitting (eV)	Conduction band splitting (eV)
MoS_2	0.148	0.003
WS_2	0.430	0.026
$MoSe_2$	0.184	0.007
WSe_2	0.466	0.038
$MoTe_2$	0.219	0.034

Table 2.1. Theoretical energies of the spin–orbit coupling in monolayer TMDCs [76, 77].

2.2 Valley polarization

Due to the broken inversion symmetry in the TMDC crystals, K and K' valley present opposite orbital magnetic moments, which through SOC are locked with the spin degree of freedom. The optical selection rules for transitions of electronic states with spins now become valley selection rules, where the transitions from the valence band to the conduction band in one valley can only be excited by circularly polarized photons with corresponding helicity. This selective excitation creates coherent excitons whose phase and polarization are the same as the pump photons. If the relaxation process of these coherent excitons is faster than all other nonradiative channels, the valley coherence will be much preserved.

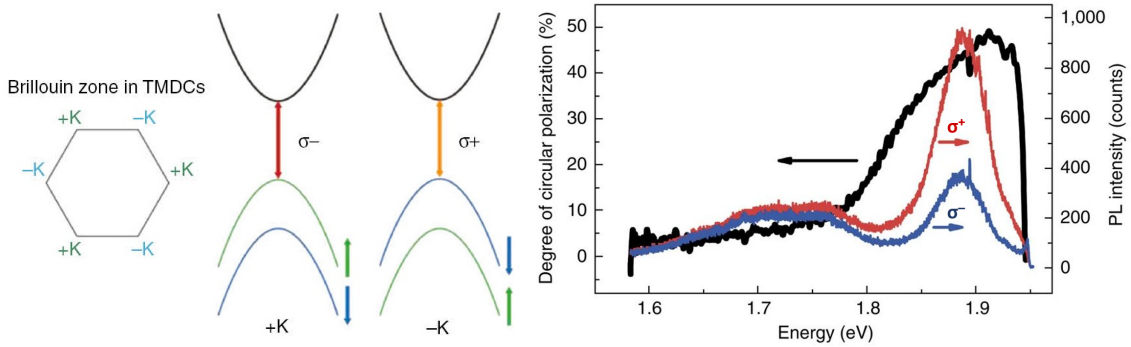

(a) **(b)**

Figure 2.3. (a) Spin splittings and optical selection rules [78]. (b) Circularly polarized PL of 1L-MoS_2 pumped by σ^+ polarized laser at 83 K, and the degree of circular polarization [79].

The degree of valley polarization can be described by

$$P = \frac{|I(\sigma^+) - I(\sigma^-)|}{I(\sigma^+) + I(\sigma^-)} \tag{2.2}$$

where $I(\sigma^+)$ and $I(\sigma^-)$ are the left and right circularly polarized component of PL intensity under a circularly polarized pump. More generally, because the polarization states of emitted photons depend on the annihilation of valley coherent excitons, the degree of valley polarization can be measured using any two orthogonal polarized states via:

$$P = \frac{I_{\text{co}} - I_{\text{cross}}}{I_{\text{co}} + I_{\text{cross}}} \tag{2.3}$$

where I_{co} and I_{cross} are the PL intensity measured in the same and orthogonal polarization as the pump, respectively.

2.3 Exciton-polaritons

As excitons couple with a photonic resonator, the interaction between the dipole moment $\boldsymbol{d}$ of the excitonic emitter and the electrical field $\boldsymbol{E}$ of the resonant mode can be described by $\hbar g = -\boldsymbol{d} \cdot \boldsymbol{E}$, where g is the interaction constant (also referred to the coupling strength). Therefore, in this coupled system with two oscillators, the Hamiltonian is written as

$$\mathscr{H} = \begin{pmatrix} \omega_{\text{ex}} - i\gamma_{\text{ex}} & g \\ g & \omega_{\text{ph}} - i\gamma_{\text{ph}} \end{pmatrix} \tag{2.4}$$

where $\widetilde{\omega}_{ex} = \omega_{ex} - i\gamma_{ex}$ and $\widetilde{\omega}_{ph} = \omega_{ph} - i\gamma_{ph}$ are the complex eigenfrequencies of the excitonic and photonic resonances. $\widetilde{\omega}_{ph}$ could be written as $\widetilde{\omega}_{ph}(\boldsymbol{k})$ if the photonic resonator has a spatial dispersion. The hybridization of two resonances yields two new eigenstates of the Hamiltonian with eigenvalues given by

$$E^{\pm} = \frac{\omega_{ex} + \omega_{ph}}{2} - i\frac{\gamma_{ex} - \gamma_{ph}}{2} \pm \sqrt{g^2 + \frac{1}{4}\left[(\omega_{ex} - \omega_{ph}) - i(\gamma_{ex} - \gamma_{ph})\right]^2} \tag{2.5}$$

The splitting of the eigenmodes at zero detuning is the Rabi frequency $\Omega = E^+ - E^- = \sqrt{4g^2 - (\gamma_{ex} - \gamma_{ph})^2}$. In the strong coupling regime, Rabi frequency has a real value, which means that $2g > |\gamma_{ex} - \gamma_{ph}|$ needs to be satisfied. One signature of the strong coupling is the avoided crossing of the two hybrid eigenstates as one resonance frequency is tuned.

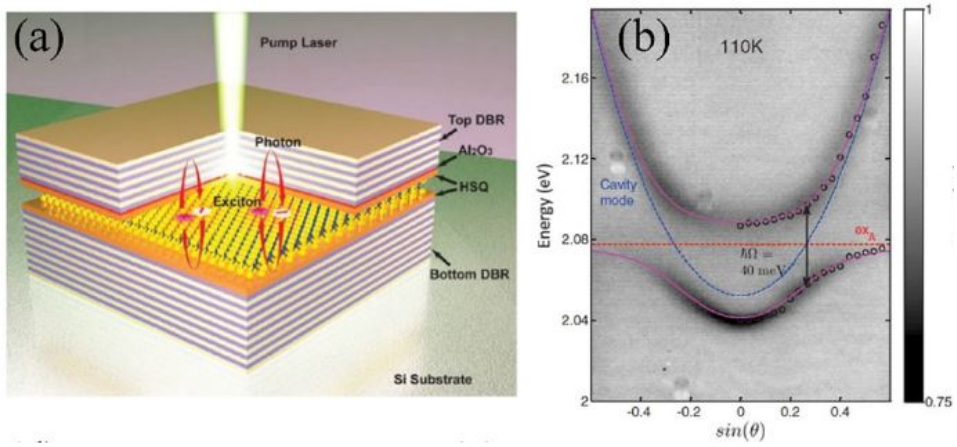

Figure 2.4. (a) Monolayer WS_2 inside a photonic cavity. (b) Angle-resolved reflectivity measured at 110 K showing a Rabi splitting of ~ 40 meV at $\sin(\theta) = 0.25$ [80].

2.4 Prospects

Excitons in 2D semiconductors have shown rich physical implications thanks to the quantum confinement and reduced dielectric screening at monolayer limit. The large binding

energy, unique optical and valley selection rules, and interaction capabilities make 2D TMDCs a comprehensive platform for the study of semiconductor physics and the development of optoelectronic devices. Besides what we have mentioned above, 2D TMDCs are also the building blocks for van der Waals heterostructures and twistronic devices, which could lead to endless possibilities for new physics and devices.

Chapter 3

Photonic crystal

3.1 Band structure and photonic simulations

A solid state crystal manifests itself as a periodic arrangement of atoms or molecules. This repeated lattice creates a periodic potential for the propagating electrons, whose wave function can be described by a Bloch state $\psi(\boldsymbol{r}) = e^{i\boldsymbol{k}\cdot\boldsymbol{r}}u(\boldsymbol{r})$, where $\boldsymbol{k}$ is the wavevector. The eigenvalues of the Schödinger equation at each $\boldsymbol{k}$ point altogether yield the electronic band structure. Photonic crystal as an analogy to solid state crystal, was first proposed to create a photonic bandgap that prohibits the propagation of photons within certain frequency range. As electromagnetic waves being modulated by the periodic dielectric features in the photonic crystal, the $\boldsymbol{k}$ dependent photonic bands also form a photonic band structure.

	Quantum Mechanics	*Electrodynamics*
Field	$\psi(\boldsymbol{r},t) = \psi(\boldsymbol{r})e^{-iEt/\hbar}$	$\boldsymbol{H}(\boldsymbol{r},t) = \boldsymbol{H}(\boldsymbol{r})e^{-i\omega t}$
Eigenvalue problem	$\hat{H}\psi = E\psi$	$\hat{\Theta}\boldsymbol{H} = \left(\frac{\omega}{c}\right)^2\boldsymbol{H}$
Hermitian operator	$\hat{H} = -\frac{\hbar^2}{2m}\nabla^2 + V(\boldsymbol{r})$	$\hat{\theta} = \nabla\times\frac{1}{\varepsilon(\boldsymbol{r})}\nabla\times$

Table 3.1. Comparison between quantum mechanics and electrodynamics [81].

In electromagnetic simulations, Maxwell's equations:

$$\nabla \cdot \boldsymbol{B} = 0 \qquad \nabla \times \boldsymbol{E} + \frac{\partial \boldsymbol{B}}{\partial t} = 0 \tag{3.1}$$

$$\nabla \cdot \boldsymbol{D} = \rho \qquad \nabla \times \boldsymbol{H} - \frac{\partial \boldsymbol{D}}{\partial t} = \boldsymbol{J}. \tag{3.2}$$

are solved in frequency domain or time domain depending on the material, structure and the actual problem. To find photonic band structures, finite-element methods (FEM) [82] and finite-difference time-domain (FDTD) methods [83, 84] are the typical ones to use. Besides, the transfer matrix method (TMM) [85] is popular for 2D and 3D structures especially with lossy materials. For layered and periodic dielectric structures, rigorous coupled-wave analysis (RCWA) [86, 87] is fast and efficient.

Below we introduce the fundamentals about the wave equation for solving the eigenvalues in frequency domain and the FDTD method.

3.1.1 Wave equation

In frequency domain, we separate spatial and time dependence of the fields by using a set of Harmonic modes and solve for each mode at a time

$$\boldsymbol{H}(\boldsymbol{r},t) = \boldsymbol{H}(\boldsymbol{r})e^{-i\omega t} \tag{3.3}$$

$$\boldsymbol{E}(\boldsymbol{r},t) = \boldsymbol{E}(\boldsymbol{r})e^{-i\omega t}. \tag{3.4}$$

Then we can replace $(\partial/\partial t)$ by $(-i\omega)$, and reduce the equations using $\boldsymbol{B}(\boldsymbol{r}) = \mu_0 \boldsymbol{H}(\boldsymbol{r})$,

$\boldsymbol{D}(\boldsymbol{r}) = \varepsilon_0 \varepsilon_r(\boldsymbol{r})\boldsymbol{E}(\boldsymbol{r})$, $\rho = 0$ and $\boldsymbol{J} = 0$ in a pure dielectric environment:

$$\nabla \times \boldsymbol{E}(\boldsymbol{r}) - i\omega\mu_0 \boldsymbol{H}(\boldsymbol{r}) = 0 \tag{3.5}$$

$$\nabla \times \boldsymbol{H}(\boldsymbol{r}) + i\omega\varepsilon_0 \varepsilon_r(\boldsymbol{r})\boldsymbol{E}(\boldsymbol{r}) = 0. \tag{3.6}$$

By eliminating $\boldsymbol{E}(\boldsymbol{r})$ in the above equations, we get the wave equation for our system:

$$\nabla \times \left(\frac{1}{\varepsilon(\boldsymbol{r})} \nabla \times \boldsymbol{H}(\boldsymbol{r}) \right) = \left(\frac{\omega}{c} \right)^2 \boldsymbol{H}(\boldsymbol{r}) \tag{3.7}$$

and the electrical field is given by

$$\boldsymbol{E}(\boldsymbol{r}) = \frac{i}{\omega\varepsilon_0 \varepsilon_r(\boldsymbol{r})} \nabla \times \boldsymbol{H}(\boldsymbol{r}). \tag{3.8}$$

For each $\boldsymbol{k}$ point, $\boldsymbol{H}(\boldsymbol{r})$ is represented by a Bloch state $\boldsymbol{H}_{\boldsymbol{k}}(\boldsymbol{r}) = e^{i\boldsymbol{k}\cdot\boldsymbol{r}} \boldsymbol{u}_{\boldsymbol{k}}(\boldsymbol{r})$, and the wave equation now takes the form:

$$(i\boldsymbol{k} + \nabla) \times \left[\frac{1}{\varepsilon(\boldsymbol{r})} (i\boldsymbol{k} + \nabla) \times \boldsymbol{u}_{\boldsymbol{k}}(\boldsymbol{r}) \right] = \left[\frac{\omega(\boldsymbol{k})}{c} \right]^2 \boldsymbol{u}_{\boldsymbol{k}}(\boldsymbol{r}) \tag{3.9}$$

where $\omega(\boldsymbol{k})$ gives the photonic band structure.

3.1.2 FDTD method

In time domain, Maxwell's equations are solved numerically on a mesh and the field components are calculated at grid points spaced Δx, Δy, and Δz apart. This discretization is known as a Yee lattice [88].

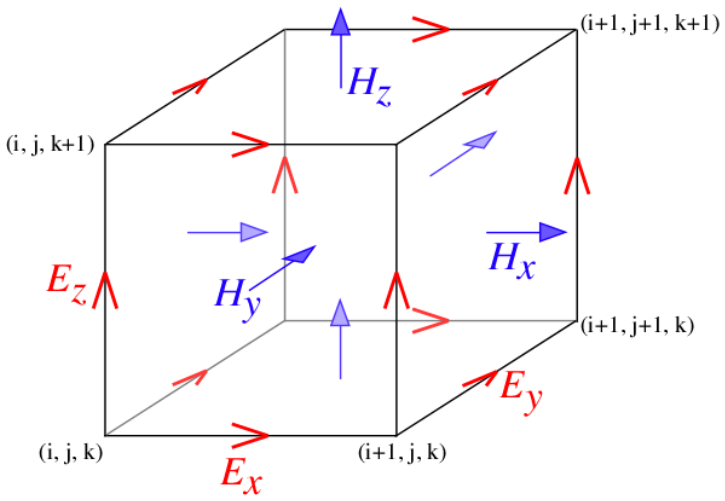

Figure 3.1. Field components in a Yee lattice. The $\boldsymbol{E}$ components are in the middle of the edges and the $\boldsymbol{H}$ components are in the center of the faces [89].

Maxwell's equations are rewritten into the scalar form for each field components:

$$\frac{\partial B_x}{\partial t} = \frac{\partial E_y}{\partial z} - \frac{\partial E_z}{\partial y} \tag{3.10}$$

$$\frac{\partial B_y}{\partial t} = \frac{\partial E_z}{\partial x} - \frac{\partial E_x}{\partial z} \tag{3.11}$$

$$\frac{\partial B_z}{\partial t} = \frac{\partial E_x}{\partial y} - \frac{\partial E_y}{\partial x} \tag{3.12}$$

$$\frac{\partial D_x}{\partial t} = \frac{\partial H_z}{\partial y} - \frac{\partial H_y}{\partial z} - J_x \tag{3.13}$$

$$\frac{\partial D_y}{\partial t} = \frac{\partial H_x}{\partial z} - \frac{\partial H_z}{\partial x} - J_y \tag{3.14}$$

$$\frac{\partial D_z}{\partial t} = \frac{\partial H_y}{\partial x} - \frac{\partial H_x}{\partial y} - J_z. \tag{3.15}$$

Each grid point with coordinate $(i\Delta x, j\Delta y, k\Delta z)$ is labeled as (i, j, k), and time $n\Delta t$ is

labeled as superscript ^{n}. As an example, Eq. 3.12 can be written in the discrete form:

$$\frac{B_z^{n+1/2}(i+\frac{1}{2},j+\frac{1}{2},k)-B_z^{n-1/2}(i+\frac{1}{2},j+\frac{1}{2},k)}{\Delta t} = \frac{E_x^n(i+\frac{1}{2},j+1,k)-E_x^n(i+\frac{1}{2},j,k)}{\Delta y} - \frac{E_y^n(i+1,j+\frac{1}{2},k)-E_y^n(i,j+\frac{1}{2},k)}{\Delta x} \tag{3.16}$$

where the time derivative of the magnetic field can be calculated by the electrical field components of the neighboring grid points. Alternatively, electrical field can be calculated by the neighboring magnetic field after $\Delta t/2$ (Eq. 3.13):

$$\frac{D_x^{n+1}(i+\frac{1}{2},j,k)-D_x^n(i+\frac{1}{2},j,k)}{\Delta t} = \frac{H_z^{n+\frac{1}{2}}(i+\frac{1}{2},j+\frac{1}{2},k)-H_z^{n+\frac{1}{2}}(i+\frac{1}{2},j-\frac{1}{2},k)}{\Delta y} - \frac{H_y^{n+\frac{1}{2}}(i+\frac{1}{2},j,k+\frac{1}{2})-H_y^{n+\frac{1}{2}}(i+\frac{1}{2},j,k-\frac{1}{2})}{\Delta z} + J_x^{n+\frac{1}{2}}(i+\frac{1}{2},j,k). \tag{3.17}$$

A practical way to get the photonic band structure using time-domain method is to convert time domain responses into frequency domain using Fourier transform. First, excite the PhC resonances via a randomly placed dipole emitter. The location of the dipole emitter should avoid high symmetry lines so that all resonances can be possibly excited. The input signal should be a short pulse to cover a wide frequency spectrum. Secondly, use a near field monitor to record the field amplitude as a function of time. Because light can couple with the

guided mode resonances, the energy stored in the resonances should slowly leak out and have a decaying amplitude of the field. Thirdly, analyze the Fourier spectrum of the time signal. The peaks and linewidths should correspond to the complex eigenfrequencies of the guided mode resonances. For better results, multiple emitters and monitors should be used in the simulation.

3.2 Fano resonances and temporal coupled-mode theory

In addition to the in-plane waveguiding, photonic crystal slabs can also couple with the free-space plane waves as the guided modes go above the light line via band folding. These bound modes become guided mode resonances with radiative loss. The coupling between the broadband Fabry-Pérot resonance and the narrow band scattering features results in an asymmetric lineshape in the transmission and reflection spectrum, which is also known as the Breit-Wigner-Fano lineshape. Because the Fabry-Pérot background of a photonic crystal slab can be calculated by direct scattering from an effective dielectric slab (see Appendix A for transfer matrix method), the Fano resonance in the photonic crystal slab is well described by the temporal coupled-mode theory (TCMT).

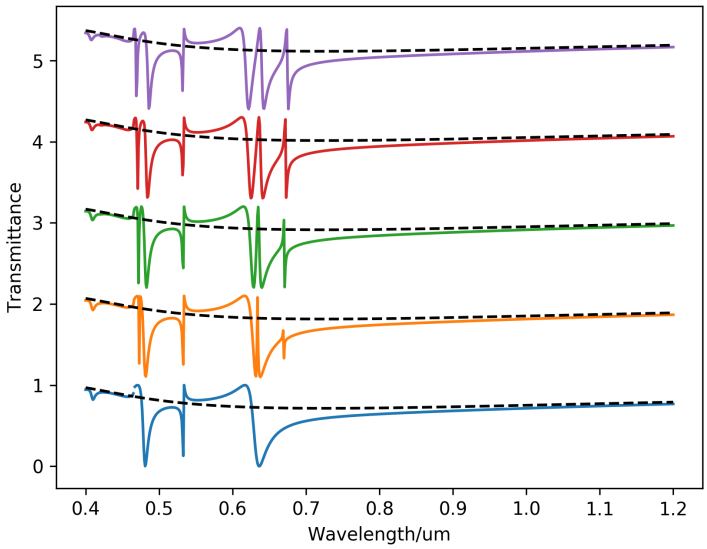

Figure 3.2. Example of Fabry-Pérot background (dashed lines) and Fano resonances in a PhC slab.Transmittance are simulated at different incidence angles.

3.2.1 Single resonance without non-radiative loss

We start with a single mode resonator that couples with m ports. The dynamic equations for the single resonance are given by[1]

$$\frac{da}{dt} = (j\omega_0 - \gamma)a + (\langle\kappa|^*)|s_+\rangle \tag{3.18}$$

$$|s_-\rangle = C|s_+\rangle + a|d\rangle, \tag{3.19}$$

where a is the resonance amplitude, ω_0 the resonant frequency, and γ the decay rate of the radiative loss. The amplitude is normalized such that $|a|^2$ is the energy stored inside the resonance. The resonance is excited by the incoming waves $|s_+\rangle = (s_{1+}, s_{2+}, ..., s_{m+})^T$, and the outgoing waves are $|s_-\rangle = (s_{1-}, s_{2-}, ..., s_{m-})^T$. Column vectors $\langle\kappa|^*$ and $|d\rangle$ contains

[1]Here we use the engineering notation $j = -i$ to be consistent with the physical oscillator representation $a = a_0 e^{-i\omega t}$.

the coupling coefficients from the resonance to the incoming/outgoing channels: $\langle\kappa|^* = (\kappa_1, \kappa_2, ..., \kappa_m)^T$, $|d\rangle = (d_1, d_2, ..., d_m)^T$. C is a scattering matrix describing the direct (non-resonant) response and can be calculated from a homogeneous slab. For excitation at frequency ω, we can define the scattering matrix S by combining Eqs. 3.18 and 3.19:

$$|s_-\rangle \equiv S|s_+\rangle = \left[C + \frac{|d\rangle\langle\kappa|^*}{j(\omega-\omega_0)+\gamma}\right]|s_+\rangle. \tag{3.20}$$

By energy conservation, when $|s_+\rangle = 0$,

$$\frac{\mathrm{d}|a|^2}{\mathrm{d}t} = -2\gamma|a|^2 = -\langle s_-|s_-\rangle = -|a|^2\langle d|d\rangle, \tag{3.21}$$

which requires

$$\langle d|d\rangle = 2\gamma. \tag{3.22}$$

By time-reversal symmetry and reciprocity (see Appendix B, section B.2.1), following constraints need to be satisfied:

$$|\kappa\rangle = |d\rangle, \tag{3.23}$$

$$C|d\rangle^* = -|d\rangle. \tag{3.24}$$

With these constraints we can verify that the scattering matrix S, like the direct scattering

matrix C, is unitary:

$$\begin{aligned} SS^{\dagger} =& CC^{\dagger} + \frac{2\gamma|d\rangle\langle d|}{(\omega-\omega_0)^2+\gamma^2} + \frac{C|d\rangle^*\langle d|}{-j(\omega-\omega_0)+\gamma} + \frac{|d\rangle\langle d|^* C^{\dagger}}{j(\omega-\omega_0)+\gamma} \\ =& CC^{\dagger} + \frac{2\gamma|d\rangle\langle d|}{(\omega-\omega_0)^2+\gamma^2} + \frac{-|d\rangle\langle d|}{-j(\omega-\omega_0)+\gamma} + \frac{-|d\rangle\langle d|}{j(\omega-\omega_0)+\gamma} \\ =& CC^{\dagger} = I. \end{aligned} \tag{3.25}$$

Here we apply the scattering matrix to the most simple case, a photonic crystal slab with up-down symmetry and in-plane mirror symmetry. Two ports are at the normal angle for transmission and reflection. The scattering matrix for direct transport can be written as

$$C = \begin{bmatrix} r_d & t_d \\ t_d & r_d \end{bmatrix}, \tag{3.26}$$

where r_d, t_d are the complex reflection and transmission coefficients that have $\pi/2$ phase difference and $|r_d|^2 + |t_d|^2 = 1$. Combining with Eqs. 3.22 and 3.24, we can derive the scattering matrix S for the system:

$$S = \begin{bmatrix} r & t \\ t & r \end{bmatrix} = \begin{bmatrix} r_d - \frac{\gamma(r_d \pm t_d)}{j(\omega-\omega_0)+\gamma} & t_d - \frac{\gamma(t_d \pm r_d)}{j(\omega-\omega_0)+\gamma} \\ t_d - \frac{\gamma(t_d \pm r_d)}{j(\omega-\omega_0)+\gamma} & r_d - \frac{\gamma(r_d \pm t_d)}{j(\omega-\omega_0)+\gamma} \end{bmatrix}, \tag{3.27}$$

where "+" denotes the even mode and "−" the odd mode.

The transmissivity and reflectivity are given by

$$R = |t|^2 = \left| r_d - \frac{\gamma(r_d \pm t_d)}{j(\omega - \omega_0) + \gamma} \right|^2 = \frac{|r_d|^2(\omega - \omega_0 + j\gamma t_d/r_d)^2}{(\omega - \omega_0)^2 + \gamma^2} \tag{3.28}$$

$$T = |r|^2 = \left| t_d - \frac{\gamma(t_d \pm r_d)}{j(\omega - \omega_0) + \gamma} \right|^2 = \frac{|t_d|^2(\omega - \omega_0 + j\gamma r_d/t_d)^2}{(\omega - \omega_0)^2 + \gamma^2} \tag{3.29}$$

If we compare these with the general form of a Fano lineshape

$$f(x; A, \mu, \sigma, q) = \frac{A(q\sigma/2 + x - \mu)^2}{(\sigma/2)^2 + (x - \mu)^2}, \tag{3.30}$$

the correspondence for reflectivity is $A = |r_d|^2$, $q = jt_d/r_d$, $\sigma = 2\gamma$, and for transmissivity $A = |t_d|^2$, $q = jr_d/t_d$,$\sigma = 2\gamma$. Because t_d and r_d have $\pi/2$ phase difference, the parameter q is always real.

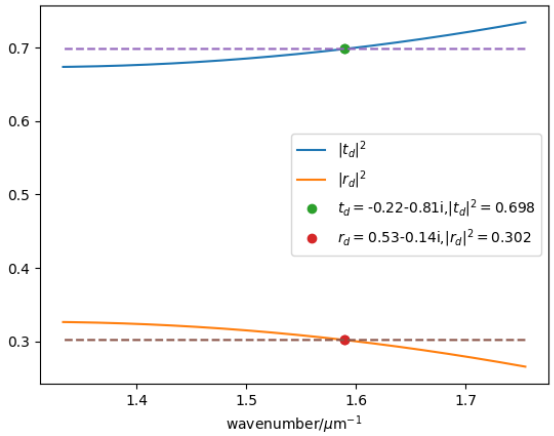

(a) Direct transmission and reflection.

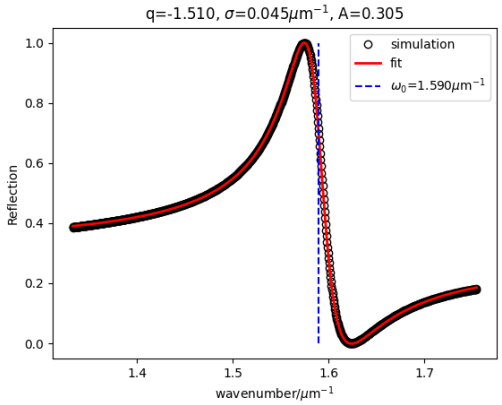

(b) Reflection spectrum.

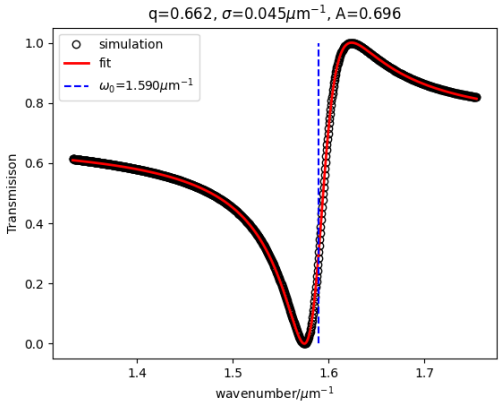

(c) Transmission spectrum.

Figure 3.3. (a) Direct scattering from a homogeneous slab with effective index. Fitting (b) reflection and (c) transmission spectra of a PhC slab by Fano lineshapes.[2].

Here we show an example of a PhC slab with single resonance around $1.6\mu m^{-1}$. The reflection and transmission spectra are simulated by Rigorous Couple Mode Analysis (RCWA) method [86] with a freely available software package [90]. By fitting the spectra with Fano lineshapes, both of them yield the same $\omega_0 = 1.590\mu m^{-1}$ and $\gamma = 0.023\mu m^{-1}$. The fitted resonance amplitudes $A_{ref} = |r_d|^2 = 0.305$ and $A_{tra} = |t_d|^2 = 0.696$ are very close to the calculated values in Fig. 3.3a. It can also be verified that $q = jt_d/r_d$ for reflection and

$q = jr_d/t_d$ for transmission.

3.2.2 Single resonance with non-radiative loss

For single resonance case, we can also derive the transmission and reflection spectra with non-radiative loss. This is of great importance to this dissertation, because the integration of 2D TMDCs on PhC slab introduces material absorption to the guided mode resonances. Moreover, the fabrication imperfections and the limited size of PhC slabs also add up to the non-radiative loss through unpredictable scattering.

With non-radiative loss, the eigenvalue of the guided resonance $\widetilde{\omega}_0 = \omega_0 - j\gamma_r$ becomes $\widetilde{\omega}_0 = \omega_0 - j(\gamma_r + \gamma_{nr})$. The non-radiative process will increase the total linewidth, but should not affect the radiative lifetime. The scattering matrix in Eq. 3.27 is modified as

$$S' = \begin{bmatrix} r' & t' \\ t' & r' \end{bmatrix} = \begin{bmatrix} r'_d - \frac{\gamma_r(r'_d \pm t'_d)}{j(\omega-\omega_0)+\gamma_r+\gamma_{nr}} & t'_d - \frac{\gamma_r(t'_d \pm r'_d)}{j(\omega-\omega_0)+\gamma_r+\gamma_{nr}} \\ t'_d - \frac{\gamma_r(t'_d \pm r'_d)}{j(\omega-\omega_0)+\gamma_r+\gamma_{nr}} & r'_d - \frac{\gamma_r(r'_d \pm t'_d)}{j(\omega-\omega_0)+\gamma_r+\gamma_{nr}} \end{bmatrix}, \tag{3.31}$$

where t'_d and r'_d are the direct scattering coefficients. Because the direct scattering also experience the non-radiative loss, we define $A_d = 1 - |r_d|^2 - |t_d|^2$ as the non-radiative loss in the direct scattering process.

Then the reflection and transmission spectra can be written as

$$R' = |t'|^2 = \frac{|r'_d|^2(\omega - \omega_0 + j\gamma_r t'_d/r'_d)^2}{(\omega-\omega_0)^2 + (\gamma_r+\gamma_{nr})^2} + \frac{|r'_d|^2\gamma_{nr}^2}{(\omega-\omega_0)^2 + (\gamma_r+\gamma_{nr})^2} \tag{3.32}$$

$$T' = |r'|^2 = \frac{|t'_d|^2(\omega - \omega_0 + j\gamma_r r'_d/t'_d)^2}{(\omega-\omega_0)^2 + (\gamma_r+\gamma_{nr})^2} + \frac{|t'_d|^2\gamma_{nr}^2}{(\omega-\omega_0)^2 + (\gamma_r+\gamma_{nr})^2} \tag{3.33}$$

where both spectra are represented by the sum of a Fano lineshape and a Lorentzian lineshape.

We can also calculate the absorption spectrum from

$$A' = 1 - R' - T' = A_d + \frac{2\gamma_r \gamma_{nr}}{(\omega - \omega_0)^2 + (\gamma_r + \gamma_{nr})^2}, \tag{3.34}$$

which includes a broad background from the direct scattering process and a Lorentzian absorption peak.

3.2.3 Overview

TCMT is a powerful tool in understanding resonances in optical resonators. In this section, we introduced two simple cases where there is only one resonance to consider. In the later chapters, TCMT will be used in more complex systems. In Chapter 5, two coupled resonances are tuned to an accidental degeneracy. The coalesced eigenvalues and eigenstates of the non-Hermitian system is the so-called exceptional point, which gives rise to a lot of unique properties and phenomena. In Chapter 6, we will use TCMT to analyze the polarization properties of the outgoing waves. Because of the broken symmetry in the PhC slab, there will be two nonequivalent directions and two polarizations, or four ports in total. The dependence of radiation properties in these ports allows us to generate circularly polarized states in the farfield, which can be used to separate valley-polarized emission. The derivations continue in Appendix B.

Part II

Controlling excitonic emission in monolayer TMDCs

Chapter 4

Directional enhancement of MoS_2 PL at photonic band edges

4.1 Abstract

Spatial dispersion of a photonic crystal manifests itself as an angle dependent optical response. Here, we use the emerging two-dimensional transition metal dichalcogenides (TMDCs) as a photon source to directly image the spatial dispersion in the reciprocal space. Excitonic emission from a monolayer MoS_2 is coupled to the delocalized Fano resonances supported by the photonic crystal slab, recreating isofrequency contours in the far-field. This integration of monolayer TMDCs and photonic crystal not only reveals the band structure of a photonic crystal but also provides a new route to controllable and directional excitonic light sources.

4.2 Introduction

Two-dimensional (2D) transition-metal dichalcogenides (TMDCs) have shown extraordinary photonic and electronic properties as atomically thin semiconductors with a direct band gap [17, 16]. The excitonic emission in the visible or near-infrared regimes from

these 2D materials is promising for light-emitting devices both in the quantum (e.g., single-photon light sources [91, 92]) and classical (e.g., light-emitting diodes [93, 19] and excitonic lasers [94, 45, 46, 36]) domains. These monolayer TMDCs can be mechanically exfoliated from bulk thanks to the weak interlayer van der Waals (vdW) forces. The out-of-plane vdW interactions also enable their convenient integration with optoelectronic devices and stacking into heterostructures of multiple 2D materials [14]. The integration of monolayer TMDCs with excitonic photoluminescence (PL) and photonic nanostructures has led to both enhancement and dynamic control of light-matter interactions in such hybrid systems [95, 96, 97, 98, 35, 99, 100, 101, 70, 30, 28, 102]. The excitonic emission of monolayers from these systems thus carries important information about the dispersive properties of the coupled photonic structures. This makes the atomically thin monolayer TMDCs a unique tool for probing the optical physics of the underlying nanostructures into which they are incorporated.

To this end, by integrating monolayer MoS_2 with a silicon nitride (SiN) photonic crystal (PhC) slab in this work, we use the excitonic PL as a near-field photon source for imaging the photonic crystal spatial dispersion in the far-field (Figure 4.1). Monolayer semiconductors such as MoS_2 can be easily transferred onto the photonic crystal after the fabrication process, offering a convenient way to examine the spatial dispersion of periodic dielectric structures without resorting to angle-resolved spectroscopy using tunable supercontinuum sources. By changing the structural parameters of the PhC slab, we spectrally tune different regions of the PhC dispersion to MoS_2 excitonic emission. The spectral overlap allows us to reveal, in the far-field Fourier domain, a range of isofrequency contours of dielectric PhCs in good agreement

with electromagnetic calculations.

Dielectric PhCs have been of interest primarily for offering large field enhancement and high extraction efficiency for local light emitters [103, 104, 105]. They can also modify the absorption and emission properties of nearby light emitting materials through efficient light-matter coupling. Here, this interaction is strictly in the weak coupling regime. Specifically, instead of directly emitting photons into the free-space, monolayer MoS_2 excitons radiate through delocalized PhC Fano resonances [106], which provide fairly uniform spatial overlap with the entire MoS_2 material. Such Fano resonances supported by PhC are also known as guided mode resonances that arise from the excitation of a waveguide mode by the introduction of a periodicity of the order-of-wavelength to achieve momentum matching. The periodic nature causes the guided mode dispersion, which normally lies below the light line, to fold back along the edges of the Brillouin zone. As a result, these modes reside above the light line, becoming accessible from the far-field and exhibiting a Fano line shape determined by radiative loss. Via reciprocity, photons generated inside the PhC and emitted into these guided resonances will scatter into the far field, allowing us to observe the PhC spatial dispersion. The conservation of in-plane momentum stipulates that the emitted photons satisfy $\boldsymbol{k}_{\parallel}^{o} = \boldsymbol{k}_{\parallel}^{i} + \boldsymbol{K}$, where $\boldsymbol{k}_{\parallel}^{o}$ and $\boldsymbol{k}_{\parallel}^{i} = (k_x, k_y)$ are the parallel (i.e., in-plane) wave-vector components of the scattered and guided photons determined by the PhC dispersion relation $\omega = \omega(k_x, k_y)$, and $\boldsymbol{K}$ is an arbitrary reciprocal lattice vector. The out-of-plane wave-vector for the far-field radiation is then determined by $k_{\perp} = \sqrt{\left(\frac{\omega}{c}\right)^2 - |\boldsymbol{k}_{\parallel}{}^{o}|^2}$. Hence, directionality of the far-field radiation can be used to extract dispersion information on a photonic crystal.

In light of these, we identify in our work three major steps involved in the

photoluminescence process: (1) absorption of excitation pump photons and generation of excitons; (2) coupling of emitted photons generated from exciton recombination into the guided resonances; and (3) resonant out-coupling of photons into the free-space. Much research has shown the important role played by photonic crystals in steps 1 and 2 to achieve overall PL enhancement from 2D TMDCs [100, 70]. In this scheme, resonances determined by transmission or reflection measurements at normal incidence are engineered to overlap with both the pump wavelength and the emission spectrum such that a multiplicative enhancement is achieved. Nevertheless, to unveil the spatial dispersion of photonic crystal using the monolayer excitonic emission, more work should be focused on step 3, i.e., the radiation process. Here, in a PhC/MoS_2 hybrid structure, we theoretically predict and experimentally control the excitonic radiation properties including the frequency, polarization, and emission pattern. We found, in the back focal plane image, that the emission pattern recreates the isofrequency contours which correspond to the overlap between the excitonic emission spectrum and the 2D PhC dispersion surface (i.e., the photonic analog of Fermi surface).

4.3 Experiment

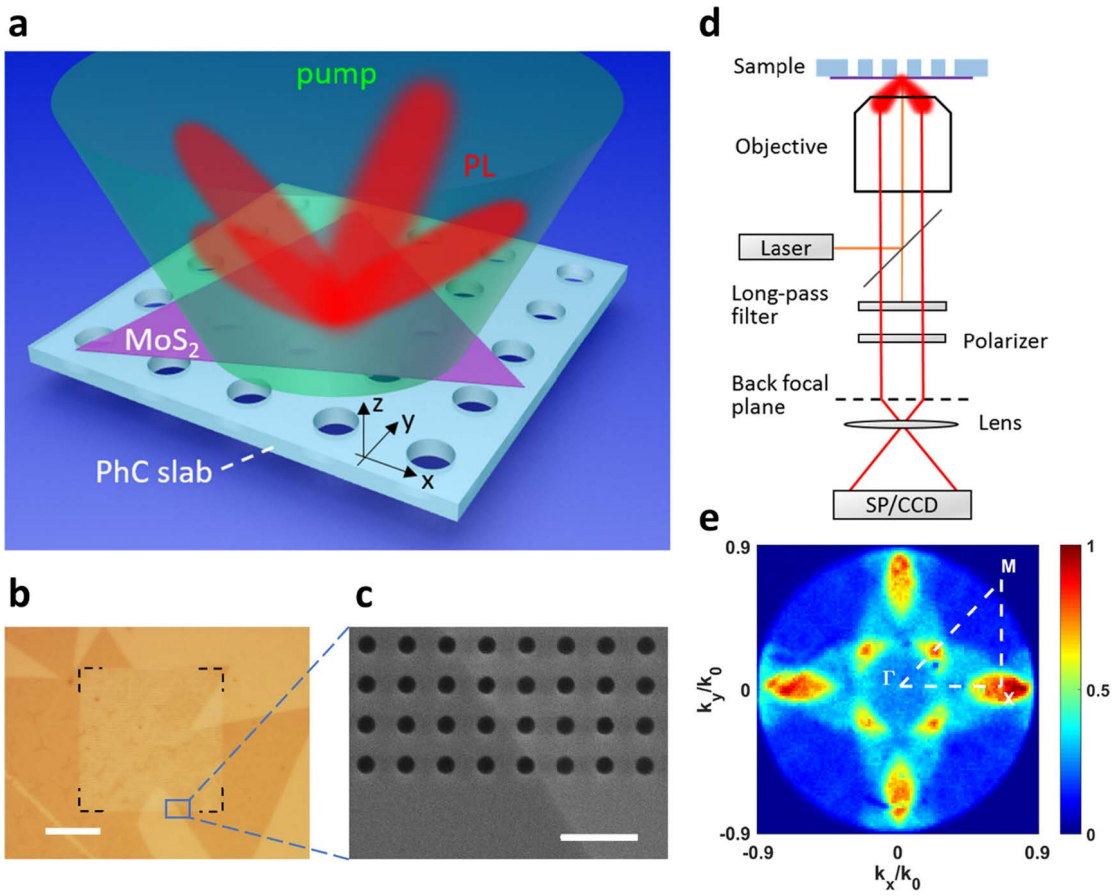

Figure 4.1. (a) Schematic of the sample. A monolayer MoS_2 is transferred onto a SiN PhC slab with square lattice of circular holes (a = 520 nm, R = 110 nm). (b) Optical microscope image of the device. The black dashed square denotes the area of PhC lattice. The darker part is covered with monolayer MoS_2. The scale bar is 10 μm. (c) SEM image of the boundary of the PhC lattice. The right half is covered by monolayer MoS_2, which appears to be brighter in this image. The scale bar is 1 μm. (d) Experimental setup for the back focal plane imaging system. SP/CCD: spectrometer equipped with a charge-coupled device. For simplicity, a series of lens for enlarging the real-space image is omitted. (e) Normalized far field PL measured at the back focal plane. Irreducible Brillouin zone is indicated by the white dashed lines using peak PL wavelength of 654 nm and lattice constant 520 nm.

The schematic of our structure is shown in Figure 4.1a. The PhC slab is fabricated by electron beam lithography on a commercially available SiN (n = 2.17) membrane of 100 nm

thickness, followed by reactive ion etching (RIE). CVD-grown monolayer MoS_2 crystals are then dry-transferred onto the fabricated PhC slab. Figure 4.1b shows the optical microscope images of a square lattice PhC consisting of 50 periods that can support delocalized guided resonances with a Fano line shape. An MoS_2 coverage of $>95\%$ on the PhC is achieved during the transfer process. Figure 4.1c shows a scanning electron microscope (SEM) image taken at the boundary of the PhC slab. The lattice constant here is a = 520 nm, and hole radius is R = 110 nm. The refractive index of monolayer MoS_2 is extracted from the reflection measurements on an unpatterned substrate by fitting to a Lorentz oscillator model (see Supporting Information S1). The monolayer MoS_2 on top of the PhC slab can be treated as a perturbation to the original photonic modes due to its atomic scale thickness. The real part of the refractive index of MoS_2 monolayer slightly increases the effective index of the PhC modes, resulting in a red-shift of the resonant wavelengths compared to those of the bare PhC samples. The imaginary part of the refractive index leads to nonradiative loss in the guided resonances, which increases the line width of the resonance peaks and lowers the overall Q factor. Although this perturbation on different modes may vary depending on the dispersion of the refractive index and the modal overlap with the monolayer, the changes of the photonic bands are relatively small (see Supporting Information S2). Therefore, the photonic band structure of the hybrid device can be used to characterize the pristine PhC slab without losing generality. In the optical measurement setup (Figure 4.1d), the 633 nm excitation line of a He-Ne laser is focused through a 0.9 NA 100× objective onto the samples. The light emission from the hybrid structures is collected through the same objective. A long-pass emission filter is used to remove the reflected stray pump photons. The back focal plane is imaged by a Bertrand lens onto the entrance slit of a

spectrometer equipped with an electron-multiplying chargecoupled device (CCD). Real-space imaging and spectroscopy are also possible in this setup using an alternative lens (detailed in Supporting Information S3). Figure 1e shows the far-field radiation pattern imaged in the back focal plane. Photons emitted with the same momentum ($k_{\parallel}^{o}$, $k_{\perp}$) impinge on the same point in the image plane. The excitonic emission is redistributed along the high symmetry directions (Γ-X and Γ-M) of the square PhC. This is consistent with the expected 90-degree rotational symmetry (C_{4z}) and reflection symmetry (IC_{2x}) of a suspended square-lattice PhC slab in the *x*-*y* plane.

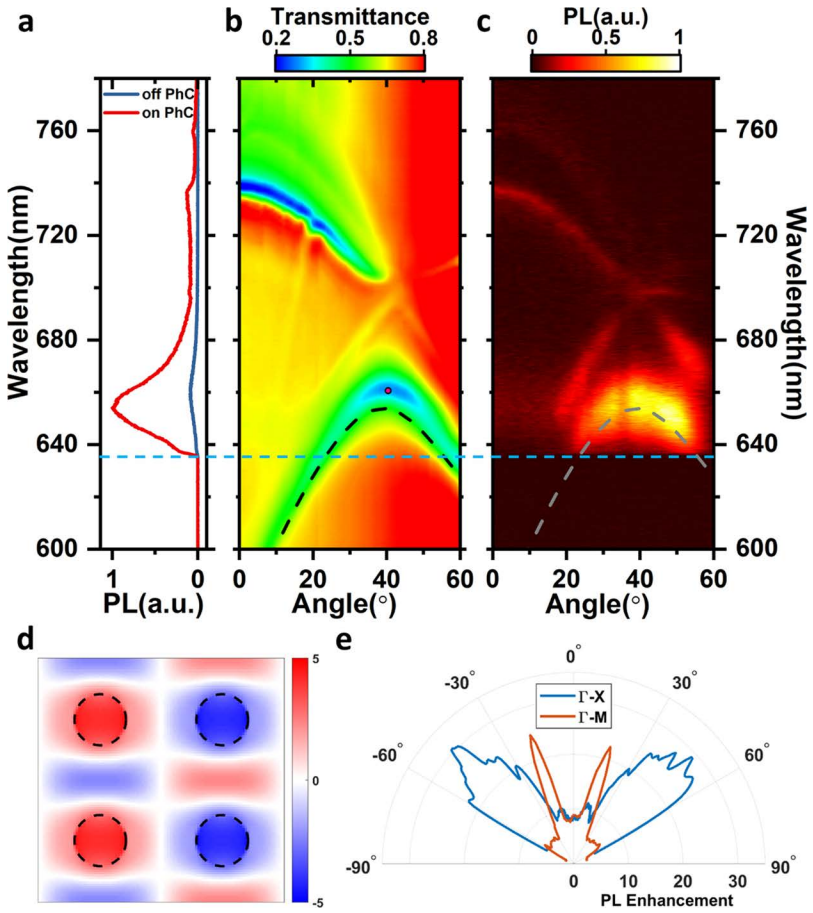

Figure 4.2. (a) Monolayer MoS_2 PL spectra on and off the PhC collected in the back focal plane with a narrow aperture centered at $k_x = 0$. At each wavelength, photons with all perpendicular momentum components k_y are averaged out. The blue dashed line shows the cutoff of the long-pass filter. (b) Angle-resolved transmittance along the Γ-X direction for p-polarized light. The angular resolution is 1°. The transmission resonances closely follow the calculated photonic dispersion (black dashed line). Pink circle denotes the photonic band-edge at the X point corresponding to the E_x field profile in (d). (c) Angle-resolved PL obtained in the back focal plane with the same aperture in (a). The gray dashed line corresponds to the same photonic band shown in (b). (d) Simulated (FDTD) E_x field profile at the top surface of the PhC slab at the X point. The black dashed lines show the boundary of the air holes. (e) Angular enhancement of PL on the PhC along the Γ-X and Γ-M directions, respectively.

The PL measurements of monolayer MoS_2 are taken in the back focal plane with a narrow aperture restricted to $k_x = 0$ (see Supporting Information S4). PL spectra on the PhC and on the bare SiN slab (i.e., off PhC) as a control are shown in Figure 4.2a. An enhancement

factor of 11 for peak PL intensity is observed. The peak position of PL on the PhC is blue-shifted compared to that off the PhC as a result of different excitonic contributions to the spectrum[107, 9, 108, 109]. The monolayer MoS_2 on the SiN substrate is n-doped, so the negatively charged excitons (i.e., A^- trions) with a peak at $\sim$1.86 eV dominate the excitonic emission. Meanwhile, the PL from suspended regions of monolayer MoS_2 is dominated by the A excitons with an emission peak of $\sim$1.90 eV. Both the exciton and trion contributions can be extracted by deconvolution of the realspace PL spectrum (Supporting Information S5). Moreover, the large spatial overlap between monolayer MoS_2 and the PhC allows for efficient coupling between excitonic emission and photonic Fano resonances, which results in an extended emission spot in the real-space PL images due to finite in-plane propagation of the Fano modes (Supporting Information S3). This coupling largely modifies the PL spectrum as we will discuss below.

Among all resonances in the PhC, those near the photonic band-edges are of greater interest, as they tend to have higher density of photonic states (DOS). At a photonic band-edge, a small frequency range corresponds to a wide range of wavevectors, which means that more photons generated from the active material can couple into the guided resonance. Also, a small group velocity near the photonic band-edge typically implies a longer interaction time between the photonic modes and the material, leading to an increase in light absorption and emission. Further, the extreme points on the equifrequency surface are typically located at the corner or along the edges of the irreducible Brillouin zone. These points are highly symmetric such that the photonic Hamiltonian around them remains unchanged upon rotation, reflection, and/or inversion operations, which is important to the study of symmetry and topology in

a photonic system. With this in mind, we start by engineering the PhC slab such that the photonic resonance at the X point ($k_X = \pi/a$) overlaps with the PL spectrum of MoS_2. The resonance of the PhC can be characterized by angleresolved transmission measurements as shown in Figure 2b. The p-polarized (i.e., electric field is in the incident plane) transmittance is measured along the Γ-X direction between 0° (normal incidence) to 60° in 1° steps with a 0.5 NA long working distance objective. The photonic band-edge appears around a wavelength of λ = 660 nm and at an incident angle of θ = 40° (indicated by the pink circle), which lies within the measured PL spectrum. The black dashed line shows the ppolarized photonic band of the pristine PhC calculated by MIT Photonic Bands (MPB) [110], which follows a similar trend as the experiment. The in-plane wave vector at the turning point calculated by $k_{\|} = 2\pi \sin\theta/\lambda \approx 6.12\mu\mathrm{m}^{-1}$ corresponds to the X point ($k_X = \pi/a = 6.04\mu\mathrm{m}^{-1}$) of the irreducible Brillouin zone.

To further elucidate the coupling between excitonic emission and the photonic resonances especially at the bandedges, we perform angle-resolved PL measurements with a 0.9 NA ($\approx \sin 64°$) objective. The same narrow aperture is used as in Figure 4.2a, followed with one single spectroscopic imaging experiment on the CCD camera. This allows us to directly record the angular distribution of the PL spectrum in the y direction (i.e., k_y vs λ at $k_x = 0$) as shown in Figure 4.2c. The horizontal axis in Figure 4.2c corresponds to $\theta = \sin^{-1}(k_y/k_0)$. The excitonic emission is drastically modified in good agreement with the photonic band structure revealed in the transmission spectra (Figure 4.2b). Large PL enhancement occurs at the angles where the PL spectrum spectrally overlapswith the photonic band-edges. This modification can also be seen in the spectrum of each lobe in the far-field

emission pattern (Supporting Information S4).

To reveal the underlying details of the light-matter interaction, we calculate the electric field profile of the resonance at the photonic band-edge using finite-difference time-domain (FDTD) method (Figure 4.2d). Since the bandedge is at the X point, the electric field on resonance has a discrete translational symmetry every two unit-cells ($k_X \cdot 2a = 2\pi$). In the simulation, the PhC slab with 2×2 unit cells is illuminated by a plane wave whose incident angle is determined by the Bloch boundary condition $k_x = \pi/a$ and $k_y = 0$. A field monitor is placed at the upper surface of the PhC slab coinciding with the plane of the suspended MoS_2 monolayer. One can see a large local field enhancement in the air holes accompanied by a chemical enhancement of the excitonic quantum yield in the suspended monolayers as reported earlier experimentally [70, 9]. Owing to the boundary conditions, the electric field in the neighboring cells along the x-direction has a 180° phase difference. This phase difference results in a destructive interference of excitonic emission in the normal direction but constructive interference at around ±40° to the surface normal. The maximum angular PL enhancement is measured to be about 30 times along the Γ-X direction (Figure 4.2e) compared with MoS_2 on the bare SiN substrate. In addition, we observe 24 times enhancement in PL at ±18° along the Γ-M direction (angle-resolved transmittance see Supporting Information S6). The angular distribution of the far-field pattern is determined by the spectral line width of the guided resonance, the group velocity near the photonic bandedge, and the overlap between MoS_2 PL and the photonic resonance. For the resonance at the X point, the emission angle ranges from 30° to 60° because the PL at shorter wavelengths can also couple into this photonic band both inside and outside the first Brillouin zone. We will later show that the farfield

radiation pattern is indeed determined by the isofrequency contours of the photonic band structure.

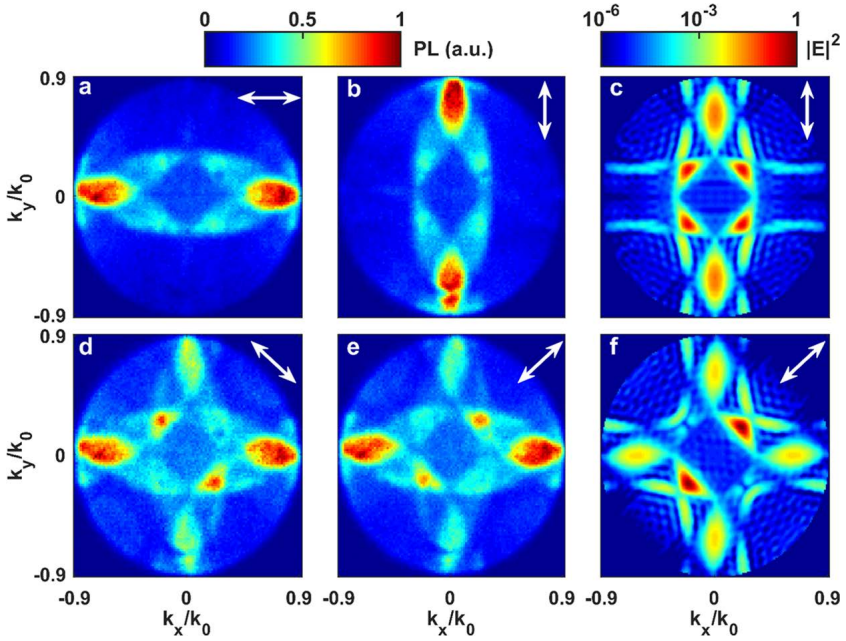

Figure 4.3. Polarization dependence of the normalized far-field PL patterns at the back focal plane. The polarizer placed between the microscope and the CCD camera is at (a) 0°, (b) 90°, (c) -45°, and (d) 45° to the *x*-axis, as indicated by the white arrows. The direction of the far-field excitonic emission is in the same plane as the polarization, presenting p-polarized states. Numerical simulation (FDTD) of far-field intensity for an electric dipole oriented at (c) 90° and (f) 45° to the *x*-axis positioned at the center of top surface of the air hole.

The photonic resonances lying within the radiation continuum can be excited by free-space plane wave with same in-plane wave-vector and polarization. Inversely, due to reciprocity, photons emitted into these resonances in the near field can also couple into the free-space with the same properties as the excitation plane wave. In Figure 4.3, we show that the far-field PL is also p-polarized; i.e., the polarization directions are within the plane of incidence. By rotating the polarizer between the microscope and the CCD camera, we observe different radiation patterns in the far-field. In Figures 3a and 3b, the degree of polarization calculated

by $(I_x - I_y)/(I_x + I_y)$ is around 0.85 for directional emission along the Γ-X directions, where $I_{x,y}$ is the light intensity at the X point with x and y-polarizations, respectively. When the polarizer is rotated to $\pm 45°$, as shown in Figures 3d and 3e, the directional emission in the Γ-M direction also exhibits p-polarization. The small discrepancy of light intensity in the Γ-X and Γ-Y directions in these two figures is due to reflection surfaces in the imaging system. Additional experiments show no valley coherence in our system at room temperature (Supporting Information S7), which means the far-field pattern is independent of the incident laser polarization. Far-field intensities for electric dipoles polarized along the Γ-X and Γ-M directions are simulated by the FDTD method in Figures 3c and 3f, respectively. Due to the limitations of our computational resources, we neglect the monolayer and use a pristine PhC with 31×31 unit cells. In each figure, a TE-polarized (i.e., in-plane) dipole source is placed on the PhC top surface to emulate the luminescent excitons in the monolayer MoS_2. The field profile calculated in Figure 2d implies a significant enhancement of the field inside the hole area, which allows us to simplify the model by placing the single electric dipole source right at the center of the air hole. The simulated far fields are plotted on a logarithmic scale for better visualization of the details. In the experiment, the sharp far-field features are averaged out, because the far-field emission pattern comes from excitons located all over the surface and consists of different wavelength components. Fabrication imperfections and inhomogeneity in the quality of monolayer MoS_2 further exacerbate this. Nevertheless, the simulated far-field patterns agree quite well with the experiments. This polarization selectivity has the potential to enable the detection of certain polarization states and active control over the angular emission profile for light emitting devices.

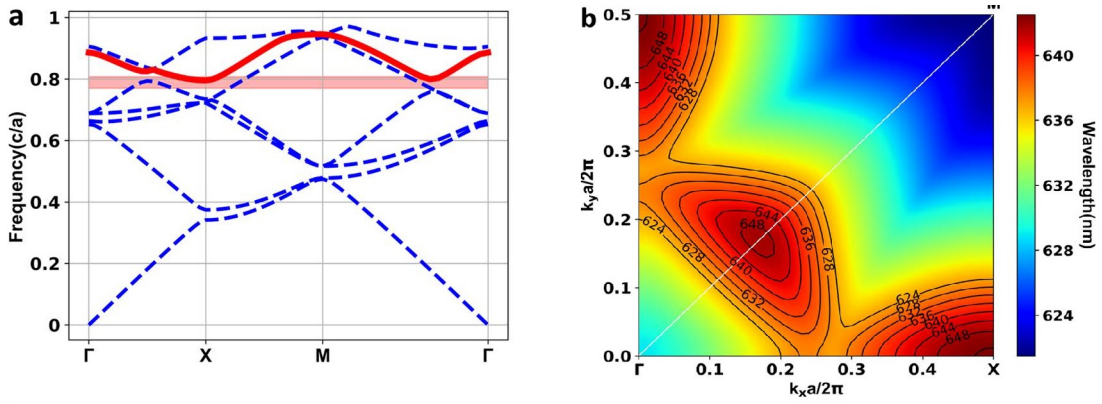

Figure 4.4. (a) Photonic band structure of the PhC slab with $a = 520$ nm and $R = 110$ nm. The spectral range of PL (red region) overlaps with the photonic band-edge of the mode in the red solid line. (b) Isofrequency contours of the PhC band structure in the quadrant of the first Brillouin zone. The numbers labeled on the contour lines are the corresponding wavelengths. Two distinct peaks of this band appear at the X point and along the Γ-M axis.

Besides the directional enhancement and polarization control achieved at the photonic band-edge, we investigate the interaction between the excitonic emission and the photonic band structure in a more general way. Since the excitonic dipoles lie within the x-y plane, emitted photons couple mostly into the transverse electric (TE)-like modes whose electric field is an even function in the z-direction. The photonic band structure for these even modes is calculated by MPB in Figure 4.4a. The red line indicates the sixth band whose band-edge overlaps with the PL spectrum indicated by the light red region (frequency converted with a = 520 nm). We note that another TE-like band also overlaps with the PL spectrum, but its directional emission is limited by both quality factor and field profile (Supporting Information S8), resulting in a negligible contribution to the back focal plane image. The dispersion relation of the highlighted band is plotted in Figure 4.4b in the first quadrant of the first Brillouin zone. The intersection of constant wavelength planes with the dispersion surface, i.e., the isofrequency contours, is plotted in the black solid lines. The peak positions for this band agree well with the far-field

pattern measured at the back-focal plane in Figure 4.1e.

We then verify that the far-field PL pattern can image the isofrequency contours of PhC slabs with different parameters. By changing the PhC lattice constant a, we can shift the photonic bands so that the isofrequency contour at the PL wavelength takes different shapes. Figure 4.5 shows different back focal plane images corresponding to increasing periods from 520 to 540 nm. Here, we only show the x-polarization component of the far-field PL patterns for visual convenience. For the PhC slab with a = 520 nm, the PL spectrum overlaps with the photonic band-edge, resulting in solid emission patterns both at the X point and along the Γ-M direction shown in Figure 4.5a. Because the PhC dispersion surface is redshifted with increasing periods, the isofrequency contours at PL wavelength will expand and move away from the photonic band-edges. This leads to larger hollow emission patterns in Figures 4.5b and 4.5c. By comparing these emission patterns with the MPB calculated results, we find that they perfectly fit the isofrequency contours at 649 nm, which are partially outlined as solid lines in the same figures. This wavelength also shows quantitative agreement with the PL peak wavelength of 654 nm, considering the small perturbation (a few nanometer redshift) to the pristine photonic band structure due to the refractive index of monolayer MoS_2. From Figures 4.5d to 4.5e, FDTD simulated far-field intensity also agrees well with the experiments for increasing periods. Thus, the spatial dispersion of PhC can be extracted from the isofrequency contours in the far-field excitonic emission patterns.

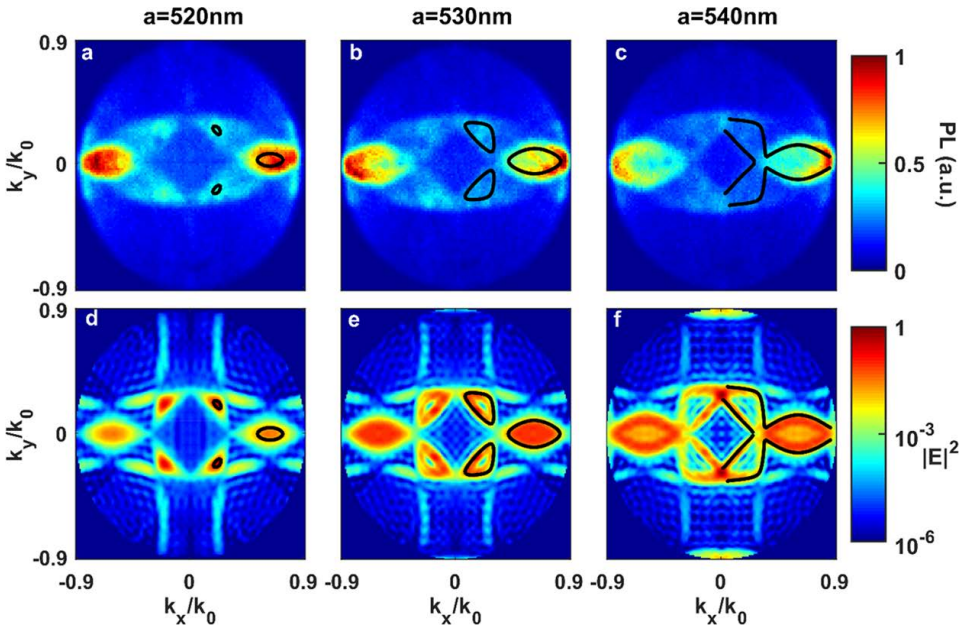

Figure 4.5. Imaging spatial dispersion of PhC with different periods: (a) 520 nm, (b) 530 nm, and (c) 540 nm. All the far-field patterns are measured for *x*-polarization. Calculated (MPB) isofrequency contours (partially outlined by the black solid lines) at 649 nm show best fit with the experimental results. With the increasing PhC period, the emission patterns expand determined by the PhC dispersion. (d-f) Simulated (FDTD) far-field intensity map for *x*-polarized dipoles placed in the air hole. The same calculated isofrequency contours (black solid lines) are shown in each column for visual guidance.

4.4 Discussion & Conclusion

In this work, we have both theoretically and experimentally demonstrated a method that utilizes monolayer excitonic emission to image the spatial dispersion of a PhC. This integration of 2D TMDC and dielectric periodic structures can benefit future research and potential applications. First, unlike other luminescent materials that may require additional host media (e.g., dye molecules) or complicated fabrication (e.g., quantum wells), monolayer MoS_2 can be conveniently transferred onto the photonic crystal after the fabrication process and will introduce minimal perturbation to the device. The luminescent excitons in monolayer MoS_2 are confined within a few angstroms, where the in-plane excitonic dipoles can only

couple into specific TE modes, allowing for direct observation of the spatial dispersion. Second, one may also use different monolayer TMDCs (e.g., $MoSe_2$, WS_2, etc.) to image within the corresponding PL spectra. Since the PL of monolayer TMDCs can be tuned by mechanical [111], electrical [19], and photochemical [9] mechanisms, it is possible to detect the spatial dispersion in a larger wavelength range. The intriguing optoelectronic properties of TMDCs such as the observation of exciton-polaritons [112], second-harmonic generation [113], and valley degree of freedom [114] can be further explored using the TMDC-coupled photonic structure. Lastly, imaging PhC isofrequency contours via monolayer TMDCs is a promising tool for far-field shaping of the radiation pattern of TMDC-based light emitting devices. The directionality and polarization of excitonic emission pattern can be further tailored via judicious design of the PhC and controlled by dynamic spectral tuning of the monolayer TMDCs [19, 9, 111]. The polarization dependence of the excitonic PL can be used to generate certain optical states, such as a polarization vortex near a bound state in continuum [115].

In conclusion, we achieved direct imaging of the spatial dispersion of PhC slabs via excitonic emission from an integrated monolayer MoS_2. The monolayer excitonic emission both spectrally and spatially overlaps with the delocalized Fano resonances, showing isofrequency contours of the photonic band structure in the far-field. We also verified that the measured isofrequency contours match quantitatively with the simulation for PhC slabs with different parameters. This work presents a potential application of 2D TMDCs for exploiting radiative properties of photonic resonances. It also offers a general route to designing 2D controllable light sources with enhanced and directional emission.

4.5 Acknowledgments

Chapter 4, in full, is a reprint of the material as it appears in ACS Photonics, 2019, with title “Monolayer excitonic emission for imaging spatial dispersion of photonic crystals”, by Wenzhuo Huang, Chawina De-Eknamkul, Xingwang Zhang, Eric Leewong, Meng-Qiang Zhao, AT Charlie Johnson, and Ertugrul Cubukcu. The dissertation author was the primary investigator and author of this paper.

Chapter 5

Observing polarization vortex on exceptional ring via WS_2 PL

5.1 Abstract

Optical bound states in the continuum (BICs) have recently been found as topological singularities in momentum space, which act as vortex cores of far-field polarization vectors. This opens up possibilities for generating optical vortex using BICs in photonic structures. However, light extraction from a BIC vortex source is hindered by the non-radiative nature of the BICs. Here, by tuning a BIC and a radiative channel in a photonic crystal slab into an accidental degeneracy, we created a flat band that encircles the BIC with a ring of coalesced eigenmodes which are also known as exceptional points. This ring of exceptional points is directly observed via photoluminescence from a monolayer WS_2 and exhibits winding polarization field that corresponds to the topological charge of the BIC. This work not only proposes a potential design for vortex sources, but also provides new perspectives for the study of Non-Hermitian physics and light-matter interactions.

5.2 Introduction

Recent decades have witnessed increasing interests in singularities in the fields of optics and photonics due to their rich mathematical and physical significance [116]. One definition of singularity is a point at which a given quantity is not well-defined. In the radiation continuum, photonic resonances typically have finite lifetimes due to their coupling to the far-field; however, there are exceptions in the momentum space where quality factors are infinitely large. These resonances are the so-called optical bound states in continuum (BICs) and manifest themselves as topological singularities that are decoupled from the far-field [68]. These localized states also act as vortex cores of the winding polarization field vector, which have been reported for the generation of optical vortices [117, 118, 69, 119]. Another kind of singularities relate to the branch points in a complex system. Exceptional points (EPs) in non-Hermitian systems are singularities at which two or more eigenstates and their eigenvalues are degenerate. EPs have been explored lately in non-conservative photonic systems thanks to the tunability of photonic resonances and the controllability over their gain/loss and coupling strengths. In the vicinity of an EP, both real and imaginary parts of the eigenvalues split into multiple branches, which leads to a number of intriguing phenomena, such as loss-induced transparency, enhanced sensing and topological waveguiding [118, 120].

Here, we experimentally observed a polarization vortex around a BIC encircled by a ring of EPs in a photonic crystal (PhC) slab, with the emerging two-dimensional (2D) transition metal dichalcogenide (TMD) as a near field light source. A photonic crystal slab is known to support guided mode resonances whose frequencies are within the radiation continuum. Among

those resonances with finite lifetimes, BICs can be found at certain k points on the photonic bands due to momentum mismatch or symmetry protection [121]. Because of their topological nature, the polarization vortices around them are robust under continuous perturbations and imperfections [122]. The idea of generating optical vortex using PhC slabs can be integrated with structures like photonic crystal surface emitting laser (PCSEL), which is potential for applications in optical communication, optical tweezers and laser beam shaping. However, because far-field excitation and radiation are intrinsically prohibited right at the BIC, a realistic BIC vortex source must radiate through its close vicinity in the momentum space whose quality factor is large but finite (i.e. quasi-BICs). The exact emission angle and wavelength will deviate from that of BIC depending on the spatial and spectral dispersions of the structure, even if the BIC itself is located at a band edge. This lack of controllability limits the practical design of BIC vortex sources, not to mention the fact that the quasi-BICs are mostly confined to the near field whose local density of states is contributed mostly by evanescent component, which is not optimal for building an out-of-plane light source [123].

On the other hand, photonic crystal slabs have provided an ideal platform for the study of non-Hermitian physics and exceptional points. Exceptional points have gained much interest ever since the quantum mechanical realization of real spectra in non-Hermitian Hamiltonians with parity-time (PT) symmetry. Later, research on non-Hermitian optics have focused on PT symmetric systems in which gain and loss are balanced; the phase transition between PT-symmetric regime and broken-PT regime happens at an exceptional point [124]. Recently, PhC slabs have been used as an optical analogy of a parity-time (PT) symmetric system where radiation rates from different channels can simulate the difference between gain and loss. By

adding a constant damping background, the broken-PT and PT-symmetric regimes can be viewed as the weak- and strong- coupling regimes of two coupled oscillators, respectively [125]. With the ease of manipulating photonic resonances in a PhC slab through parameter tuning, isolated or continuous EPs can be created depending on the exact configuration [65, 66]. The exotic dispersion relations associated with the EPs can incorporate with the aforementioned polarization vortex, providing zero dispersion and enhancement of local density of states that benefits the performance of the device as a potential light source [126, 127].

In this work, we manipulate the photonic resonances in a PhC slab to reach accidental degeneracy so that a BIC is located inside an effective broken-PT regime where a flat band is enclosed by a ring of exceptional points. The polarization vortex around the symmetry-protected BIC core is inherited by the degenerate eigenstates at the exceptional points. We experimentally observed this dispersion and the polarization vortex around the BIC with the aid of a monolayer WS_2 through its photoluminescence (PL). The flat band and branching behavior at the EPs can be seen from the angle-resolved PL measurement; the far field emission pattern follows the isofrequency contour of the exceptional ring in the momentum space, showing a winding polarization field. This combination of polarization vortex and EP utilizes peculiar topological and symmetrical properties of singularities in a PhC slab, shedding lights on singular optics, light-matter interactions in non-Hermitian systems, and potential applications of vortex light sources.

5.3 Concept

Photonic crystal slab as an open system supports guided mode resonances which are radiative due to the coupling to the extended plane waves. These resonances can be described by complex frequencies where the imaginary part represent the radiative losses. In a squared lattice PhC slab, we consider a dipolar mode and a quadrupolar mode with complex frequencies $\widetilde{\omega}_{1,2} = \omega_{1,2} + i\gamma_{1,2}$ respectively at the Γ point. At $k = (0,0)$ in the Brillouin zone, the quadrupole mode cannot couple to the far-field due to symmetry mismatch; therefore, it is a symmetry-protected BIC and the radiative loss $\gamma_2 = 0$. As $|\boldsymbol{k}|$ increases, the perturbation creates a non-zero modal overlap between the dipole-like mode and the quadrupole-like mode. Under first order approximation, the coupling strength is linearly proportional to $|\boldsymbol{k}|$, so we can write the effective Hamiltonian as

$$\mathscr{H} = \begin{pmatrix} \widetilde{\omega}_1 & \beta|\boldsymbol{k}| \\ \beta|\boldsymbol{k}| & \widetilde{\omega}_2 \end{pmatrix} \tag{5.1}$$

where β is the linear coefficient. The complex eigenvalues of this Hamiltonian are given by

$$\widetilde{\omega}_{\pm} = \frac{\omega_1 + \omega_2}{2} + i\frac{\gamma_1}{2} \pm \sqrt{\left(\frac{\omega_1 - \omega_2}{2} + i\frac{\gamma_1}{2}\right)^2 + \beta^2|\boldsymbol{k}|^2} \tag{5.2}$$

The exemplar dispersion relations of these two bands along one momentum axis (e.g. k_x) are plotted in Fig. 5.1. The dimensionless parameters we use here are $\omega_1 = 1$, $\gamma_1 = 0.1$ and $\beta = 0.2$. The real parts of the eigenvalues are shown as the solid lines, whereas the imaginary parts are proportional to the widths of these lines. When $\omega_1 \neq \omega_2$ (Figs. 4.1a and 4.1c), the real parts of the eigenvalues are separated by a bandgap equal to $|\omega_1 - \omega_2|$. Specifically, at

$k = 0$, the quadrupole-like mode has zero linewidth as a BIC. As we continuously tune the intrinsic frequency ω_2 across the fixed ω_1, the bandgap closes and reopens. At accidental degeneracy condition where $\omega_1 = \omega_2$ (Fig. 5.1b), both bands have zero dispersion within $|\boldsymbol{k} < k_{\mathrm{EP}}$ ($k_{\mathrm{EP}} = \gamma_1/2\beta$). As their eigenvalues share the same real parts, the imaginary parts are given by $\gamma_{1,2}/2 \pm \sqrt{(\gamma_1/2)^2 - \beta^2|\boldsymbol{k}|^2}$, one of which is still equal to 0 at the Γ point. This means the BIC is preserved at the accidental degeneracy, which leads to a polarization vortex circling around the Γ point as mentioned. At $|\boldsymbol{k}| = k_{\mathrm{EP}}$, both resonances coalesce to the same eigenmode which is the branch point of the dispersion curve. These branch points form a continuous ring in the two-dimensional momentum space, i.e. the exceptional ring. The coalesced eigenmodes on the exceptional ring inherit the topological charge of the encircled BIC, hence the winding polarization field is robust to the perturbations and imperfections. Moreover, the existence of such EPs is guaranteed in a realistic PhC slab whose Hamiltonian can deviate from this simple form, as long as a band flip can be observed through parameter tuning. Through an adiabatic encircling of an EP, the band flip results in switching of the eigenstates, which indicates that the accidental degeneracy separates two topologically distinct phases [128].

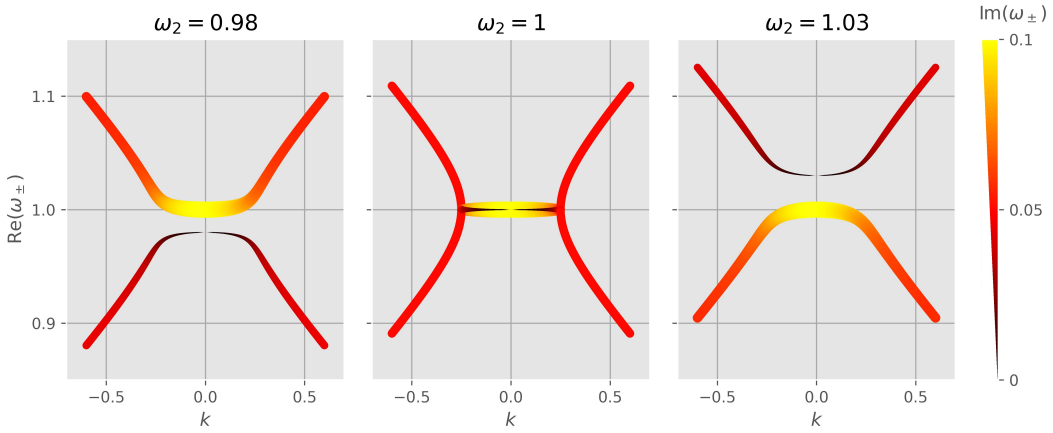

Figure 5.1. Band dispersions of the non-Hermitian Hamiltonian under conditions (a) $\omega_1 > \omega_2 = 0.98$; (b) $\omega_1 = \omega_2 = 1$; and (c) $\omega_1 < \omega_2 = 1.03$, respectively. The dimensionless frequency of the dipole mode is fixed at $\omega_1 = 1$ and $\gamma_1 = 0.2$. The band structure exhibits an avoided crossing when $\omega_1 \neq \omega_2$, whereas a flat band is formed when accidental degeneracy is reached.

In PhC slabs, transmissivity of guided resonances generally presents asymmetric Fano lineshapes that arise from the coupling between the scattering from the periodic features and the non-zero transmission background (see Chapter 3 Subsection 3.2.1).

$$T(\omega) = \frac{A\,(q\sigma/2 + \omega - \mu)^2}{(\sigma/2)^2 + (\omega - \mu)^2} = \frac{A(\omega - \varepsilon)^2}{|\omega - \widetilde{\omega}|^2} \tag{5.3}$$

where μ, σ are the resonance frequency and linewidth, respectively, q is the Fano parameter and A is the amplitude which is determined by the transmission background. We can rewrite the Fano lineshape in terms of the complex eigenfrequency $\widetilde{\omega} = \mu + i\sigma/2$ and a real parameter $\varepsilon = \mathrm{Re}(\widetilde{\omega}) - q \cdot \mathrm{Im}(\widetilde{\omega})$. The complex eigenvalue of the resonance corresponds to the frequency and the linewidth of the Fano lineshape. In regard to two resonances couple near an EP, the combined lineshape is more complicated and the eigenvalues are implicit in the transmission or reflection spectra. In Appendix B, Subsection B.1.2, we show that the transmission spectrum

of two coupled resonances can be deconvoluted into two independent Fano lineshapes that are characterized by the eigenvalues of the non-Hermitian Hamiltonian,

$$T(\omega) = C + \frac{A_+(\omega - \varepsilon_+)^2}{|\omega - \widetilde{\omega}_+|^2} + \frac{A_-(\omega - \varepsilon_-)^2}{|\omega - \widetilde{\omega}_-|^2} \tag{5.4}$$

where C is a constant background and $\widetilde{\omega}_\pm$ are the complex eigenvalues. Note that these are collective eigenvalues $\widetilde{\omega}_\pm$ of the Hamiltonian, distinct from the complex frequencies $\widetilde{\omega}_{1,2}$ of the individual modes. More generally, the combined Fano lineshapes can incorporate with the material loss (and gain) and be used to predict the absorption (and emission).

To better characterize the dispersion of the PhC slab with realistic parameters, we perform electromagnetic simulations using Rigorous Coupled Wave Analysis (RCWA)[90] and compared it with the theoretical predictions from the coupled mode theory. The PhC slabs in this paper are made of 100 nm thick commercially available Si_3N_4 membrane, with a squared lattice of cylindrical air holes with lattice constant a and radius r (Fig. 5.2a). The dielectric constant of Si_3N_4 used in the simulation is 2.17. The photonic resonances in a PhC slab overall depend on its periodic feature defined by the lattice constant a. In general, increasing the lattice constant a can redshift the band structure as a whole. Furthermore, tuning the radius r of the air holes can affect the dipole mode and quadrupole mode differently, which enables a continuous change on $\omega_1 - \omega_2$. Therefore, by tuning the lattice constant a and radius r simultaneously, one can realize accidental degeneracy at any wavelength within a wide range. This allows us to prepare a PhC slab that has an EP within the excitonic emission range of the emitter. Here, we find through simulation that a PhC slab with $a = 446$ nm and $r = 137.5$ nm has an accidental

degeneracy of dipole mode and quadrupole mode at 607 nm, which is ideal for the integration with the monolayer WS_2. Fig. 5.2b shows the simulated angle-resolved transmission spectra of the proposed PhC slab along two high-symmetry directions Γ – X and Γ – M, with s- and p-polarizations, respectively. These are polarization directions of the dipole and quadrupole bands that we are interested in. A sharp resonance with shrinking linewidth at Γ point is the BIC from the quadrupole mode. Using the combined lineshape of Fano resonances, we can extract the complex eigenvalues from the transmission spectra at each k point. The real parts of the eigenvalues of two interested transpose electric (TE)-like bands are shown in Fig. 5.2c, which exhibits a flat plate encircled by a ring of exceptional points. The polarization states of the eigenmodes are extracted from polarization dependent transmission spectra (Supplement 3). The quadrupole-like band that encircles the at-Γ BIC has a linear polarization state inside the exception ring. The polarization directions of the coalesced eigenmodes are labeled on top of the projected exceptional ring in green color. If we take a clockwise close loop around the Γ point by 2π azimuthal angle, the polarization vector of the quadrupole mode will rotate counter-clockwisely by 2π. This indicates a topological charge of -1 for the vortex around the BIC.

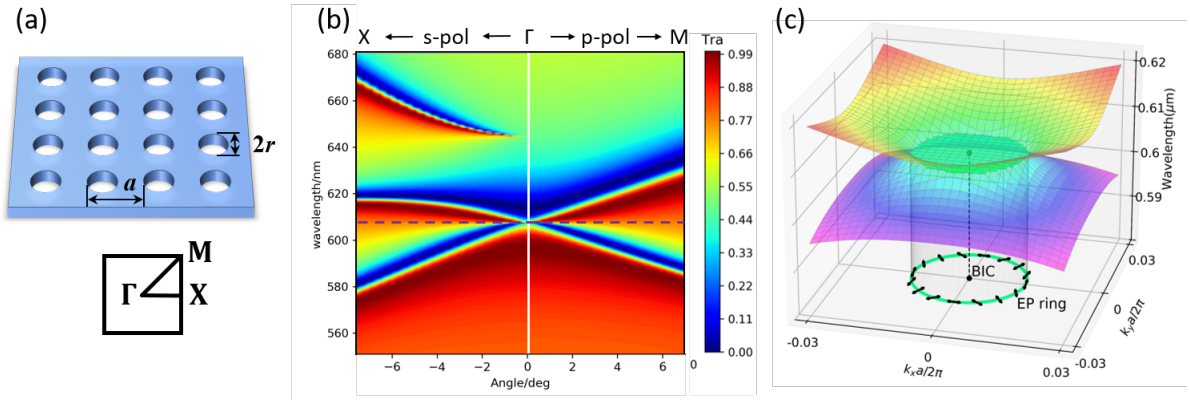

Figure 5.2. (a) Schematic of the PhC slab and the first Brillouin zone in the momentum space. (b) Simulated angle-resolved transmission spectra along Γ – X direction in s-polarization and Γ – M direction in p-polarization. Accidental degeneracy happens at Γ point with wavelength of 607 nm. (c) Simulated band structure of the PhC slab around the Γ point. The flat band with a BIC at the center is encircled by the exceptional ring.

5.4 Experiment

To experimentally realize EP at the emission wavelength of monolayer WS_2, we perform a wide search in the parameter space to find accidental degeneracy between the dipole and quadrupole modes. Transmission spectra of multiple samples with same period $a = 442$ nm and radii from 124 nm to 133 nm (1 nm interval) are measured at normal incidence angle in Fig. 5.3a (Experiment setup in Appendix C). Even though the quadrupole mode is a BIC at Γ point, the neighboring quasi-BICs are detectable as a small bulge in the transmission spectra due to the beam divergence and the inevitable disorder in the sample. This feature allows us to extract the eigenvalues of both the broad dipole mode and narrow quadrupole mode (described below). In Fig. 5.3b, with increasing radii of the air holes, the filling factor decreases and so do the effective indices of both modes. Nevertheless, the quadrupole mode blueshifts faster than the dipole mode, and the crossing happens at $r = 130$ nm. A detailed characterization of this sample is shown by the angle-resolved transmission spectra in Fig. 5.3b, which agree well with

the simulation results.

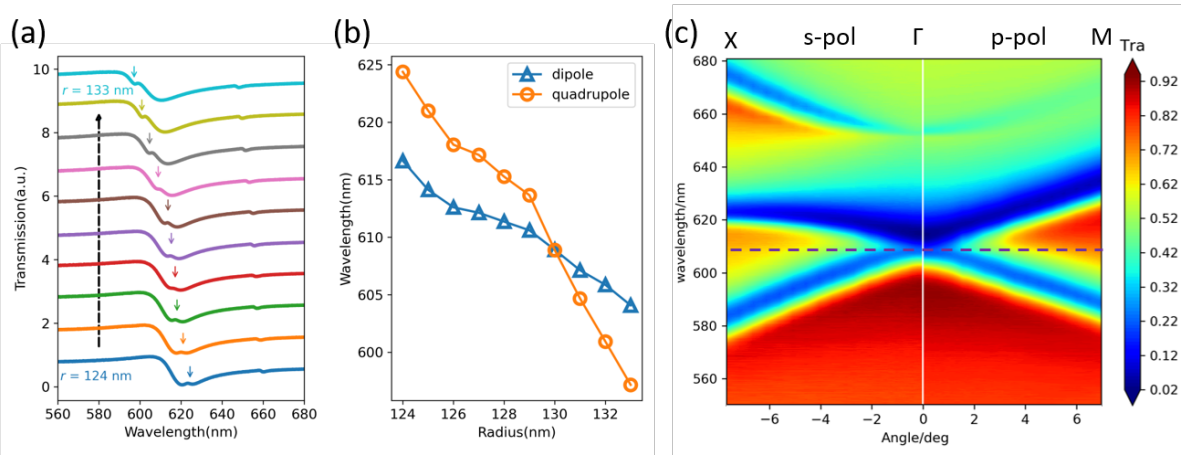

Figure 5.3. (a) Transmission spectra of PhC slabs with different radii. The lattice constant of these PhC slabs are the same $a = 442$ nm. The small arrows indicate the real parts of the eigenvalues (in nanometer) of the quasi-BICs. (b) Eigenmode wavelengths versus the radius of air holes. The accidental degeneracy is found in the sample with $r = 130$ nm. (c) Experimental result of angle-resolved transmission spectra of the sample with $r = 130$ nm. The measurements are along Γ – X direction with s-polarized plane wave and Γ – M direction with p-polarized plane wave. The accidental degeneracy at 608 nm is labeled by the dashed line.

As mentioned above, we fit the transmission spectra using the combined Fano lineshape. The real and imaginary parts of extracted eigenvalues are plotted in Fig. 5.4a. Within 0.5° range away from the Γ point, the real parts of the eigenvalues are almost flat, whereas the imaginary parts have a significant dispersion that separates the dipole mode and the quadrupole mode. Ideally, the BIC and nearby quasi-BICs have sharp spectral features with diminishing linewidths; however, due to the scattering from the sample disorder and a finite angular collection width, these sharp features become small bulges inside the broad dipole background. Inside the exceptional ring, these bulges cannot even be found as local extrema, but they are still observable under the fit. In Fig. 5.4b, we show three exemplar fits at different angles of interest. The data and the fitted curves are plotted in solid lines, and the two Fano components are plotted

in dashed lines. The thin vertical lines represent the real parts of the eigenvalues. An additional Fano component much away from the two modes is omitted for visual convenience but its contribution to the fit is already considered. As two eigenmodes approaching the coalesced state, each Fano component can have diverging height that are greater than 1, yet most of them are cancelled and the combined lineshape is still finite [129].

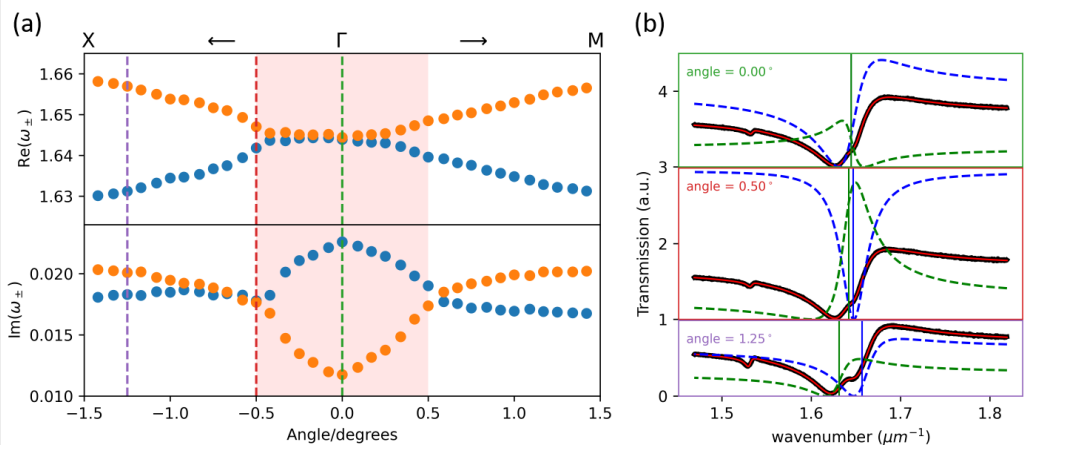

Figure 5.4. (a) Extracted complex eigenvalues from the experimental results of angle-resolved transmission spectra. The step size is 5 minutes of arc (1°/12). The branching behavior at around 0.50° implies the position of the EP. (b) Example fits of transmission spectra at 0° (green), 0.50° (red) and 1.25° (purple). Black solid lines: experimental data; red solid lines: fitted transmissivity curves; Blue and green dashed lines: Fano components of the fits; Blue and green solid lines: real parts of the eigenvalues.

After we verify the existence of EP in the PhC slab, the monolayer WS_2 is transferred onto the sample. Fig. 5.5a shows the optical image of the device, and Fig. 5.5b gives the PL spectrum of the integrated WS_2/PhC pumped with a 594 nm laser. The PL peak is around 617 nm, which aligns with the accidental degeneracy after considering the redshift caused by the monolayer and minimal PDMS residue during the transfer. The angle-resolved transmission spectra of the WS_2/PhC are measured along Γ-M direction with p-polarized light in Fig. 5.5c. Due to the excitonic absorption from the monolayer WS_2, both dipole and quadrupole modes

exhibit higher non-radiative losses. As a result, transmissivity of the WS_2/PhC becomes broader compared with that of the bare PhC sample. In Fig. 5.5d, we simulate the angle-resolved transmissivity along the same direction for WS_2/PhC. The refractive index of monolayer WS_2 used here was measured experimentally from our previous work [74]. The simulated transmissivity shows excellent agreement with the experimental results in terms of the spectral broadening. Interestingly, we find that the dipole mode is more affected by the non-radiative loss and exceptional points are moved further away from the Γ point (Supplement 5). In Fig. 5.5e, we show the dispersion of the hybrid device through angle-resolved WS_2 photoluminescence along Γ-M direction with a step size of 10 minutes of arc. A branching behavior of the PL spectra can be seen at around 3°, where a flat band starts to split into two. This is in accordance with the simulated absorption spectra in the same angular range shown in Fig. 5.5f. Notably, the experimental PL also exhibit higher intensity near the branching point, which follows the theoretical prediction of LDOS enhancement at an EP [126]. Under a uniform non-radiative background, such enhancement can also be seen in the simulated absorption spectra.

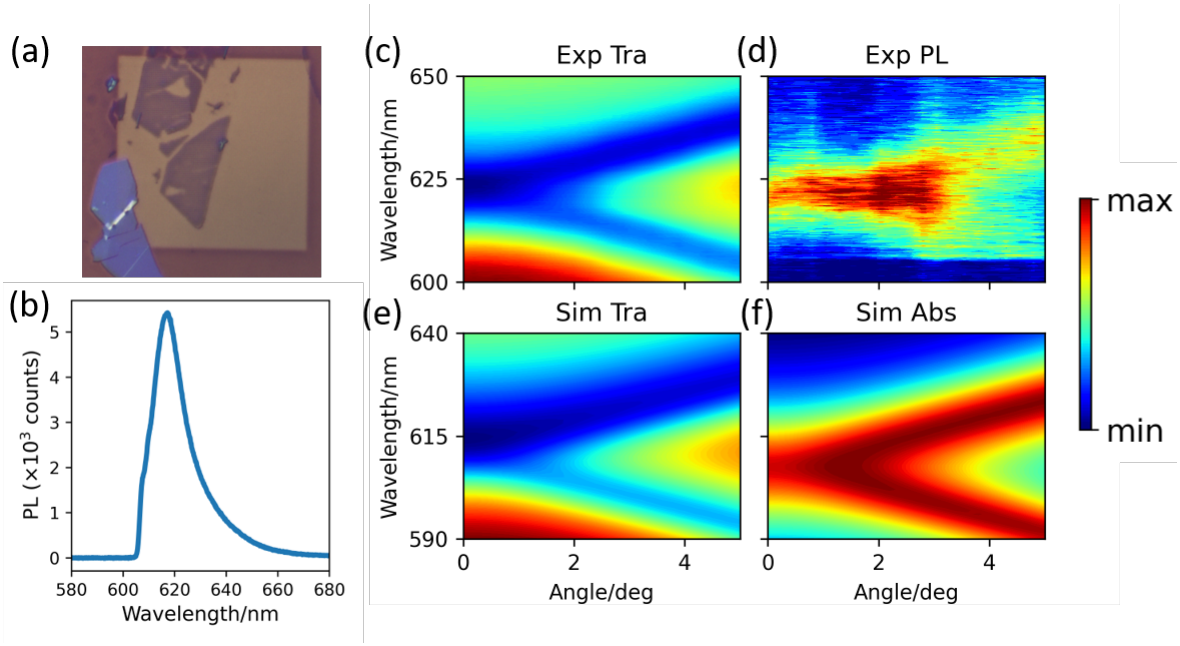

Figure 5.5. (a) Optical image of the WS_2/PhC sample. (b) PL spectrum from WS_2 on the photonic crystal slab. Experimental result of angle resolved (c) transmission and (d) PL spectra along Γ-M direction with p-polarized light are compared with simulated (e) transmission and (f) absorption spectra.

In our previous work, we showed that a near field emitter on a photonic crystal slab can not only show the band dispersion through angle-resolved measurement, but it also directly images the isofrequency contours in the far field [7]. Here, the back focal plane image of WS_2 PL reveals the contour of the exceptional ring in Fig. 5.6, at different polarization angles. The radius of the ring measured from this image is about 0.05 NA, or 2.9° in terms of angle, which is consistent with the angular span of PL in Fig. 5.4d. By rotating the linear polarizer in front of the detector, we verify that the winding number of the polarization vortex on the exceptional ring is -1, which is the same as the topological charge of the encircled BIC. For comparison, we also simulate the absorption map in the momentum space with different polarization directions at PL peak wavelength, which match the experiment results quite well.

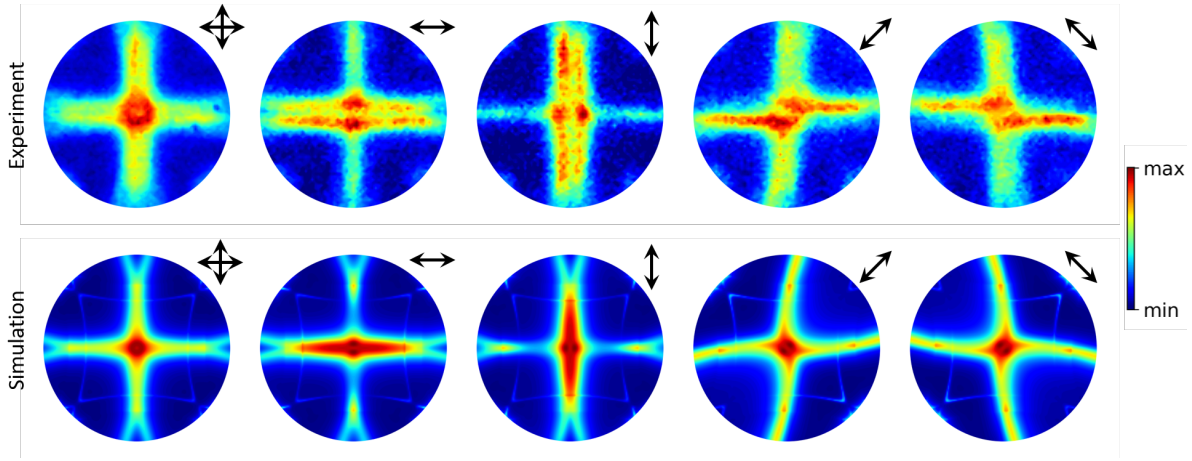

Figure 5.6. Top row: far-field excitonic emission pattern from the WS_2/PhC device. Directions of the polarizer in front of the detector are shown by the arrows. Bottom row: simulated absorption in momentum space at PL wavelength. Polarization of incident plane waves are shown by the arrows.

5.5 Conclusion

In conclusion, we have directly observed the polarization vortex around a BIC through far-field emission from a PhC/WS_2 hybrid device. The photoluminescence from WS_2 is emitted through a ring of exceptional points in the momentum space of the PhC slab, which is realized by tuning the BIC and a radiative channel into accidental degeneracy. This manipulation of photonic resonances not only creates a flat band that preserves the polarization field from the vortex core to a ring of coalesced resonances, but it also enables efficient coupling of a quadrupole-like band to the far-field. This provides a novel idea for building a vortex source from photonic structures that support BICs. Our results also contribute to the interdisciplinary study between non-Hermitian physics and atomically thin semiconductors.

5.6 Acknowledgements

Chapter 5, in full, is currently being prepared for submission for publication of the material with title “Direct observation of polarization vortex on exceptional ring using WS_2 photoluminescence”, by Wenzhuo Huang, Chawina De-Eknamkul, and Ertugrul Cubukcu. The dissertation author was the primary investigator and author of this paper.

Part III

Valleytronics and exciton-polaritonics in multi-layer WS_2

Chapter 6

Directing valley-polarized emission of 3L WS_2 by photonic crystal with directional circular dichroism

6.1 Abstract

The valley degree of freedom that results from broken inversion symmetry in two-dimensional (2D) transition-metal dichalcogenides (TMDCs) has sparked a lot of interest because of its huge potential in information processing. In this work, to optically address the valley-polarized emission from a three-layer (3L) WS_2 at room temperature, we employ a photonic crystal slab that supports delocalized guided mode resonances. By breaking the inversion symmetry of the photonic crystal slab via a perturbation, we can simultaneously manipulate s and p components of the radiating field so that these resonances correspond to circularly polarized emission. The emission of excitons from distinct valleys is coupled into different radiative channels and hence separated in the farfield. This directional exciton emission from selective valleys provides a potential option for valley-based light emitters, which is crucial for future valleytronic devices.

6.2 Introduction

In two-dimensional (2D) transition-metal dichalcogenides (TMDCs), broken inversion symmetry gives rise to a new valley degree of freedom, which has enormous implications for information processing [79, 130]. The indirect bandgaps in the bulk states of TMDCs transition to energy-degenerate direct bandgaps at K and K' valleys with contrasting Berry curvatures and orbital magnetic moments when they thin down to monolayers [131, 132, 133, 134]. Because of the strong spin-orbit coupling at K and K' valleys, valley-polarized excitons may be optically manipulated under optical selection rules [135, 136, 137, 138, 139, 140]: left-handed circularly polarized photons can only stimulate band-edge excitons at K valley, whose emission has the same helicity as the pump photons. This valley selective photoluminescence (PL) is critical for the development of valley-based light emitters, which will serve as the foundation for future valleytronic devices [141, 142].

However, at room temperature, intervalley coupling between excitons can drastically diminish valley coherence, making valley-dependent functions difficult to implement. Although changes in the environment, such as temperature [134, 136, 139], external fields [143, 144, 145], or mechanical strain [146], may be used to tune valley polarization, most of them are not optimal for practical applications. Few-layer TMDCs, on the other hand, offer a viable option for valleytronic devices since carrier mobility increases as the number of layers grows [147]. As a result, few-layer TMDCs have a shorter exciton lifetime and increased valley polarization [148]. In this work, we employ 3L WS_2 for our valleytronic device because of its decent valley polarization at room temperature.

To construct a valley-based emitter based on TMDCs, excitons from distinct valleys must be separated. By integrating TMDCs with nanostructures that response differently to valley pseudo-spin, excitons from distinct valley are coupled with different radiative channels [149, 150, 151]. Spin-momentum locked modes supported by nanowires [152, 153, 154], asymmetric grooves [154], or domain boundaries [155] are one approach to segregate valley excitons, although the light-matter interaction is generally restricted to a narrow region that is 1D. 2D photonic nanostructures with circular dichroism, such as chiral metasurface [49, 50, 33, 51] and asymmetric nanoantennae [156, 157], are proposed to increase the interaction volume. However, the resonances in these structures are still localized and have high material loss, preventing exciton emission from distant propagation. To address these issues, we integrate the 3L WS_2 with a dielectric photonic crystal (PhC) slab that supports delocalized guided mode resonances. Photonic crystals, as a perfect platform for modifying the polarization state of radiation [158, 71], have demonstrated high level of control over the emission rate and radiation pattern of near field emitters [95, 159, 112, 7, 37]. The photonic Fano resonances of delocalized nature, in particular, match well with the 2D TMDCs in the transverse direction. In this work, the radiative channels of the PhC slab are designed in such a way that they correspond to the helicity of circular polarization and only pair with the excitons from distinct valleys. Valley-polarized exciton emission is therefore separated in the far-field as a result.

6.3 Concept and Design

As an optical counterpart to solid state crystals, photonic crystals feature a periodic arrangement of unit cells with symmetry. Supported by the PhC slabs with finite thickness,

guided mode resonances with frequency above the light cone can couple to free-space plane waves with the same in-plane momentum. This coupling is well characterized by temporal couple-mode theory [158, 160], which not only predicts the Fano lineshapes of these resonances but also offers information on the polarization states of the outgoing waves. The phase difference between the out-coupling coefficients in s and p polarization, d_s and d_p, of a PhC slab in the xy plane with rotational symmetry around the z-axis (C_2) is constrained by the direct (non-resonant) scattering components via

$$\arg\left(\frac{d_s}{d_p}\right) = \frac{1}{2}\arg\left(\frac{r_s+\sigma t_s}{r_p+\sigma t_p}\right) + N\pi \tag{6.1}$$

where r_s, t_s, r_p and t_p are the s- and p-polarized non-resonant reflection and transmission coefficients at the resonance frequency when photonic crystal slab is treated as a homogeneous dielectric slab, and $\sigma = \pm 1$ are for TE-like and TM-like resonances respectively. Here we only consider TE-like resonances since excitons in WS_2 are in the transverse directions, hence $\sigma = 1$ in all cases. The far-field polarization vector is represented by $\vec{d} = d_s\hat{s} + d_p\hat{p}$. To get a resonance that can couple with circularly polarized light, d_s and d_p must have comparable amplitudes and a phase difference that is close to $\pm\pi/2$. However, these two conditions are barely satisfied simultaneously for most photonic crystal slabs with C_2 symmetry. For example, when direct scattering is on Fabry-Pérot resonance ($t_s = t_p = \pm 1$), the phase difference between d_s and d_p would be $N\pi$, which corresponds to a linearly polarized state. Nevertheless, by breaking the in-plane inversion symmetry, two opposite propagation directions $\pm\boldsymbol{k}_{\parallel}$ are no longer equivalent. This means a time-reversal operation will also flip the in-plane momentum,

and the out-coupling coefficients are jointly constrained by:

$$\arg\left[\frac{d_s\left(\boldsymbol{k}_{\parallel}\right)d_s\left(-\boldsymbol{k}_{\parallel}\right)}{d_p\left(\boldsymbol{k}_{\parallel}\right)d_p\left(-\boldsymbol{k}_{\parallel}\right)}\right]=\arg\left(\frac{r_s+\sigma t_s}{r_p+\sigma t_p}\right) \tag{6.2}$$

where d_s and d_p are now dependent on the in-plane momentum $\pm\boldsymbol{k}_{\parallel}$. Even if the right-hand side of the above equation is zero, the phase difference $\arg\left[d_s\left(\boldsymbol{k}_{\parallel}\right)/d_p\left(\boldsymbol{k}_{\parallel}\right)\right]$ may still be non-zero. Specifically, when the propagation vectors are perpendicular to the mirror surface of the persisted reflection symmetry, $d_s\left(\boldsymbol{k}_{\parallel}\right)=-d_s\left(-\boldsymbol{k}_{\parallel}\right)$ and $d_p\left(\boldsymbol{k}_{\parallel}\right)=d_p\left(-\boldsymbol{k}_{\parallel}\right)$ should hold. In this situation, we get

$$\arg\left[\frac{d_s\left(\pm\boldsymbol{k}_{\parallel}\right)}{d_p\left(\pm\boldsymbol{k}_{\parallel}\right)}\right]=\frac{1}{2}\arg\left(\frac{r_s+\sigma t_s}{r_p+\sigma t_p}\right)\pm\frac{1}{2}\pi \tag{6.3}$$

where the extra $\pm\pi/2$ phase shift originates from the negative sign of d_s in opposite directions. As a result, the far-field polarization field can be elliptically polarized in $\left(\pm\boldsymbol{k}_{\parallel},\boldsymbol{k}_{\perp}\right)$ directions with opposing helicity, where $\boldsymbol{k}_{\perp}$ denotes the out-of-plane momentum. An out-going wave with directional circular polarization can be achieved by tweaking the parameters of a photonic crystal, which is ideal for separating valley-polarized excitons.

We start with a Si_3N_4 photonic crystal slab that has two sets of holes in a square lattice. Each smaller hole is at the center of four neighboring larger holes, making this structure C_2 symmetric. By shifting the smaller hole by $2c$ along x direction in Fig. 6.1a, the in-plane inversion symmetry is broken as the larger holes and the smaller holes are not interchangeable; nevertheless, the mirror symmetry at the xz surface is retained. In the First Brillouin zone of this

photonic crystal, Γ-Y and Γ-Y' directions that are perpendicular to the mirror surface become non-equivalent. Y(Y') points in this context are defined as $\boldsymbol{k}_{\parallel} = (0, \pm\pi/a)$, where a is the lattice constant. This relative shifting of the air holes, if is small compared to the lattice constant, could act as a perturbation to the lattice that splits an isolated s band into energy-degenerate s and p bands as calculated by Rigorous Couple Wave Analysis (RCWA) in Fig. 6.1b. As reported in many literatures, we also verified that the radiative decay γ_p of generated p band at Γ point is proportional to the square of the shifting length c. This monotonic increase of p-polarized coupling coefficient $\left|d_p\right|$ (which is equal to $\sqrt{\gamma_p}$ at Γ point) guarantees an interception of $|d_s(\theta)|$ and $\left|d_p(\theta)\right|$ at certain angle if the shifting length c is properly chosen. Moreover, since shifting the holes will not change the effective index of the slab, the phase difference between d_s and d_p remains unchanged by equation (3). Here, the parameters of the PhC slab are as follows: refractive index $n = 2.17$, slab thickness $t = 100$ nm, lattice constant $a = 440$ nm, large hole radius $R = 120$ nm, small hole radius $r = 60$ nm, and shifting length $c = 12$ nm. In Fig. 6.1c, the angular dependence of the relative phase between d_s and d_p is calculated using the effective index of the slab, i.e. the square root of the spatial-averaged permittivity. The amplitudes of d_s and d_p are extracted from the lineshapes of the resonances in Fig. 6.1b. Within a wide range along Γ-Y direction where d_s and d_p have comparable amplitudes and close to $\pi/2$ phase difference, the out-going wave would present a near circular polarization. This is verified by the simulated angle-resolved transmission spectra of a left-hand circularly polarized (σ^+) plane wave in Fig. 6.1d. The large resonance amplitude in Γ-Y' direction displays that the resonance is σ^+ polarized, while the diminishing amplitude of resonance in Γ-Y direction indicates a resonance with opposite helicity (σ^- polarized). If pumped with

σ^- polarized plane wave, the corresponding angle-resolved spectra will be mirrored against Γ point, as shown in Fig. 6.1e. As comparison, we also simulate the transmission spectra of PhC slabs without shifting the holes in Supplement 1, and they always present symmetric patterns against the Γ point regardless of the pump polarization. This reveals the unparalleled capability of a photonic crystal slab with broken inversion symmetry in controlling circular polarization in the momentum space.

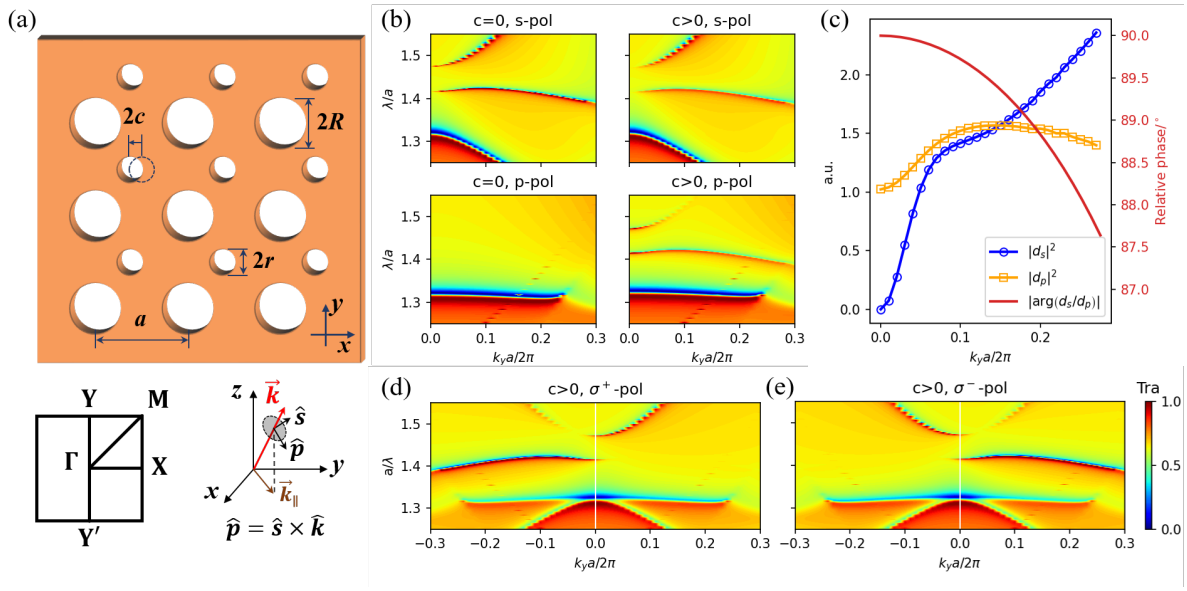

Figure 6.1. (a) Breaking the inversion symmetry of a PhC slab by a perturbation. The smaller holes are shifted by $2c$ along x-axis, making Γ-Y and Γ-Y' directions inequivalent. (b) Transmission spectra of photonic bands before and after the perturbation versus k_y. A p-polarized band appears at the same location as the pre-existed s-polarized band. (c) Amplitudes and relative phase of coupling coefficients d_s and d_p versus k_y. Transmission spectra of (d) σ^+ and (e) σ^- polarized incident plane waves. The asymmetric patterns reflect directional circular dichroism in this PhC slab.

To further explore the ability of our design in separating valley excitons, we place a dipole emitter at the top surface of a photonic crystal slab in FDTD solutions to mimic the valley excitons at the near field. The PhC slab in this simulation has 20-by-20 unit-cells. The

farfield radiation pattern is calculated at the resonant wavelength using electrical field at a near field monitor that is slightly above the top surface of the slab. First, the dipole emitter is set to be y-polarized. The farfield intensity, given by $|E_x|^2 + |E_y|^2$, is equally distributed in $+y$ and $-y$ directions as shown in Fig. 6.2a. Because the out-going wave from this PhC slab has directional circular dichroism in Γ-Y(Y') directions, we can also extract the circularly polarized components through $E_\pm = (E_x \pm iE_y)/\sqrt{2}$ in the farfield. The farfield emission pattern of $|E_+|^2$ in Fig. 6.2b shows a stark contrast between out-going waves in $\pm k_y$ directions, which proves that the polarization states of these radiative channels are indeed circular. Next, we create a chiral emitter by placing two orthogonal dipoles at $\pm 90^\circ$ phase difference for left or right circular polarization. The farfield intensity $|E_x|^2 + |E_y|^2$ for both polarizations are shown in Figs. 6.2c and 6.2d. When excitons from one valley are selectively pumped, they tend to couple into the guided resonance that has circularly polarized farfield with same helicity. Finally, considering the broadband nature of the excitonic emission, we sum up the farfield intensities of all wavelength components near A exciton peak to get a more realistic radiation pattern. In Figs. 6.2e and 6.2f, these comprehensive farfield patterns from a broadband left and right circularly polarized emitters exhibit an emission strip along negative and positive k_y directions, respectively.

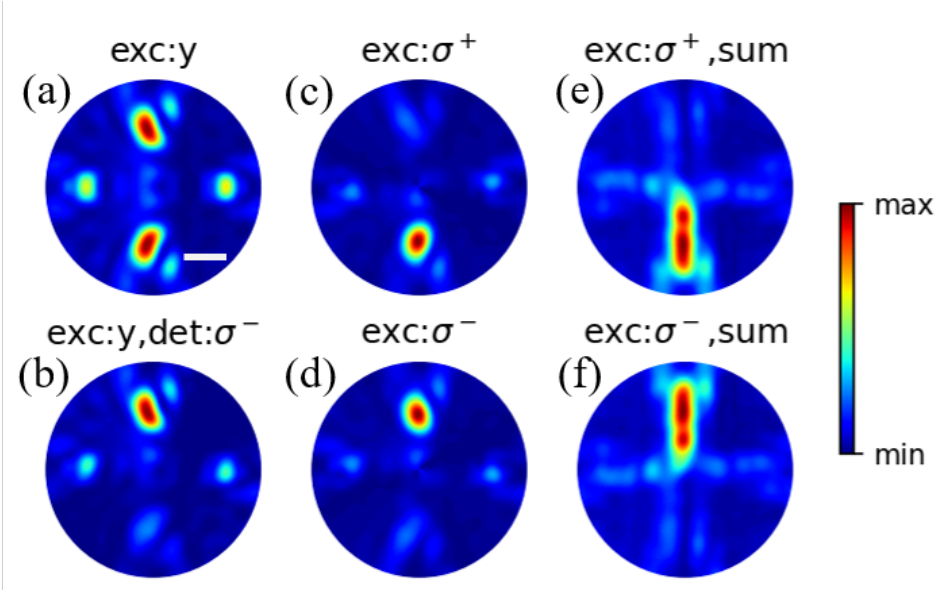

Figure 6.2. (a) Farfield radiation pattern from a y-polarized local dipole emitter at resonant wavelength. The scale bar is 0.2 NA. (b) σ^- polarized component of the farfield emission in (a). Farfield radiation patterns from a chiral emitter with (c) positive and (d) negative helicity at resonant wavelength. Farfield radiation pattern from a broadband chiral emitter with (e) positive and (f) negative helicity.

6.4 Result and Discussion

To experimentally observe the directional circular dichroism in a photonic crystal slab with broken inversion symmetry, we fabricated the Si_3N_4 photonic crystal slabs with the proposed parameters using electron beam lithography. We then measured the angle-resolved transmission spectra of the PhC slab by putting the sample on a rotational stage under collimated white light. Here, we chose a PhC sample with a slightly larger shifting length ($c = 20$ nm) than that in the simulation. There are two considerations. First, a larger separation angle is preferred for better observation. This requires $\left|d_p\right|^2$ to intercept with $|d_s|^2$ at a larger angle, which corresponds to a larger $\left|d_p\right|$. Second, the farfield components in angle-resolved transmission simulation/measurement are defined in the $(\hat{s},\hat{p})$ coordinate system, which is different from the

in-plane polarization field where an ($\hat{x}$,$\hat{y}$) coordinate system is used. For polarization field in Γ-Y(Y') direction, the p-polarized component is projected onto y direction by a factor of $\cos(\theta)$, where θ is the incidence angle. This means that to get a circularly polarized farfield from a near field chiral emitter, $\left|d_p\right| / |d_s| = 1/\cos(\theta)$ needs to be satisfied. Both considerations will need a stronger perturbation to the original PhC slab to get larger $\left|d_p\right|$, thus a larger shifting length was chosen experimentally. In Figs. 6.3a and 6.3b, the angle-resolved transmission spectra under s- and p-polarized incident plane waves were measured for both Γ-Y and Γ-Y' directions. These spectra are symmetric to the Γ point as expected. We also observed a deeper resonance in p-polarization in accordance with our expectation of greater $\left|d_p\right|$. We then measured σ^+ and σ^- polarized transmission spectra and the results are shown in Figs. 6.3c and 6.3d. Here, the transmission spectra demonstrate an asymmetric pattern in $\pm k_y$ directions as a result of the broken inversion symmetry in the PhC slab. This directional coupling of circularly polarized resonance agrees well with our simulation, showing its promising ability in controlling the radiation pattern with helicity.

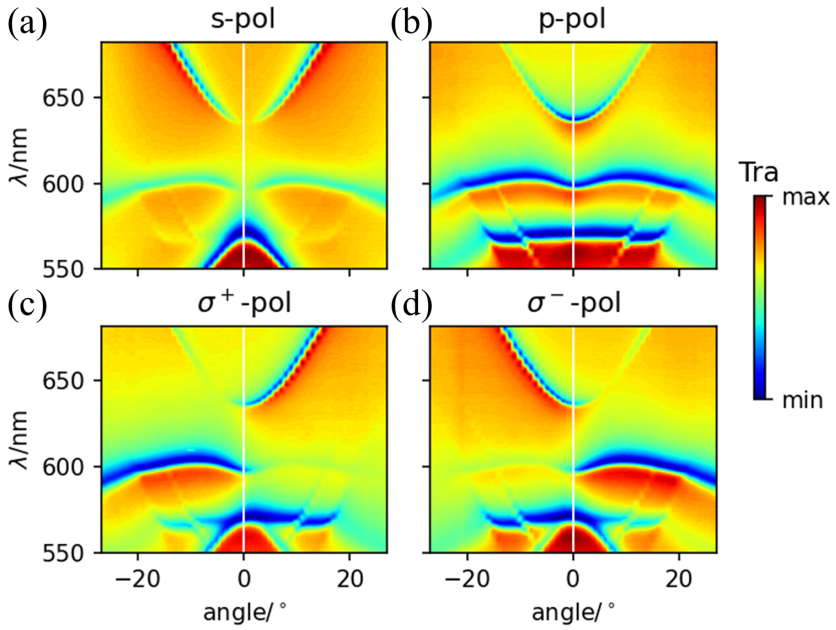

Figure 6.3. Experimental angle-resolved transmission spectra of the PhC slab with broken inversion symmetry. The measurement is along Y'-Γ-Y direction. The spectra are symmetric against Γ point for (a) *s* and (b) *p* polarizations due to the mirror symmetry by the *xz* plane; but they are asymmetric for (c) σ^+ and (d) σ^- polarizations because of the opposite helicity of the supported circularly polarized states in Γ-Y and Γ-Y' directions.

We then transferred a mechanically exfoliated 3L WS_2 onto the PhC slab. The optical image of the WS_2/PhC sample is shown in Fig. 6.4a. The sample was pumped by a 594 nm laser with linear polarization, and the PL was detected after a polarizer for co- and cross-polarized spectra, respectively (Fig. 6.4b). The valley polarization at the A exciton resonance is around 30%∼40%. This is slightly lower than a suspended 3L WS_2 due to the PL from the SiN PhC slab. As WS_2 is a lossy material, the PhC slab with 3L WS_2 absorbs more laser power than a bare PhC slab, which results in stronger PL from SiN that cannot be completely removed by subtraction. We expect the valley polarization to be higher with a TMDC that has higher quantum yield. Another peak at roughly 780 nm is a distinct characteristic of exciton emission from the indirect bandgap of 3L WS_2 [161], which has zero valley polarization as expected.

The peaks around 608 nm are Raman peaks from phonon modes in WS_2, which are irrelevant to the purpose of this paper. To verify the ability of the PhC slab in modifying the farfield polarization, we performed polarization resolved PL measurements in the back focal plane. With a linearly polarized laser in y direction, excitons from K and K' valleys are equally stimulated. Using a quarter waveplate and a linear polarizer on the detection side, σ^+ and σ^- polarized components of PL can be resolved and separated in the farfield. In Figs. 6.4c and 6.4d, angle-resolved PL with $k_x = 0$ and k_y ranging from $-0.5k_0$ to $0.5k_0$ were measured with σ^+ and σ^- detectors, where $k_0 = 2\pi/\lambda$ is the momentum in free-space. The spatial dispersion of PL corresponds to the band structure of the PhC slab, which is consistent with the asymmetric transmission spectra. A redshift in resonance wavelength was observed because the addition of 3L WS_2, whose real part of the index is around 5 in the visible range, increases the effective mode index. This measurement confirms that the directional emission from the radiative channels are circularly polarized, and their helicity is correlated to the momentum in y direction. The degree of circular polarization, as calculated by $(I_{\sigma^+} - I_{\sigma^-}) / (I_{\sigma^+} + I_{\sigma^-})$, reaches up to 66% within PL wavelengths. In addition to the angle-resolved spectra, we also recorded the farfield radiation pattern from the back focal plane. A 650 nm low-pass filter was used to remove the exciton emission from the indirect bandgap. The pump laser at 594 nm was still y-polarized. As shown in Figs. 6.4e-g, back focal plane images with y, σ^+ and σ^- polarized components were taken. Clearly, these images show that the exciton emission from 3L WS_2 is separated in the farfield according to the helicity of their circular polarization: left (right) handed circularly polarized component is mainly directed to the free-space with a negative (positive) momentum in y direction.

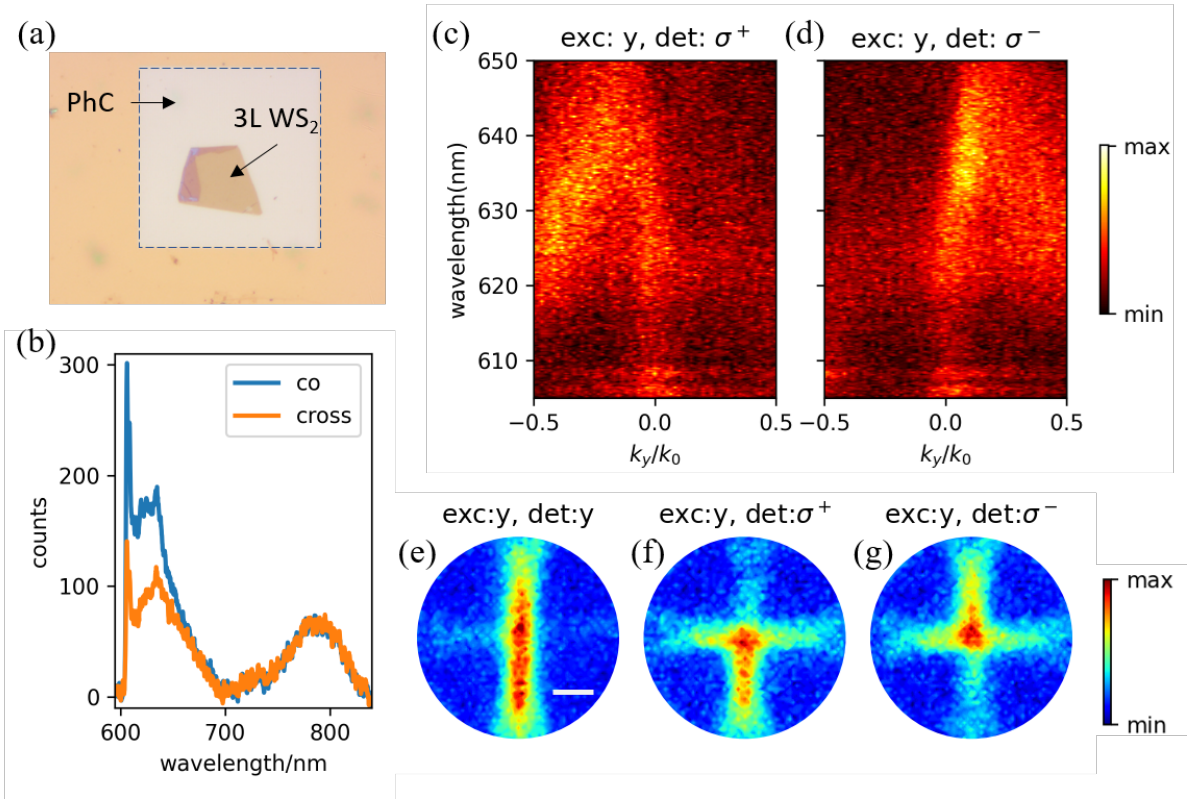

Figure 6.4. (a) Optical image of the 3L WS_2/PhC sample. The PhC is fabricated in the dashed square with a side length of 44 μm (100×100 unit-cells). (b) Polarization resolved PL spectra of the 3L WS_2 on PhC. (c) σ^+ and (d) σ^- polarized components of PL spectra versus k_y. The sample is pumped by a linearly polarized laser in y direction. Farfield radiation patterns of (e) y, (f) σ^+ and (g) σ^- polarized components. The scale bar is 0.2 NA.

Last but not least, because the valley coherence in 3L WS_2 allows us to control the polarization of the exciton emission, the farfield pattern from our WS_2/PhC device could be solely modulated by the polarization state of the pump. In Figs. 6.5a-d, the polarization states of the pump laser were set to be x, y, σ^+ and σ^-, respectively; and there was no polarizer on the detection side. To remove the Raman signals, the PL is filtered by a band pass filter centered at 630 nm with full width at half maximum (FWHM) of 10 nm. When the pump laser was linearly polarized, excitons from both valleys are stimulated equally; thus, the farfield pattern is symmetric in $\pm k_y$ directions as shown in Figs. 6.5a and 6.5b. When the pump laser was

circularly polarized, however, excitons from one valley are more populated than from the other. This selective excitation of valley excitons leads to imbalanced circularly polarized components in the exciton emission. As circular polarizations with opposite helicity are separated in the momentum space by different radiative channels supported by the PhC slab, asymmetric farfield patterns are observed with circularly polarized pump in Figs. 6.5c and 6.5d. Here, the degree of circular polarization is determined not only by the circular polarization of the radiative channels, but also by the valley polarization of the 3L WS_2. Their product sets the upper limit of the circular polarization with a selective circularly polarized pump, assuming that the coupling between circularly polarized emission and the polarization-dependent radiative channels is perfect. In this device, the limit is calculated to be 23% from previous results, and we experimentally observed a circular polarization of around 8%. This proof-of-concept experiment demonstrated that a PhC slab with directional circular dichroism may be utilized to distinguish farfield emission with different circular helicity that originates from valley-polarized excitons. We argue that the degree of separation can be further improved by using 2D materials with higher valley polarization [162] and PhC slabs that exhibit larger circular dichroism through fine tuning of the parameters.

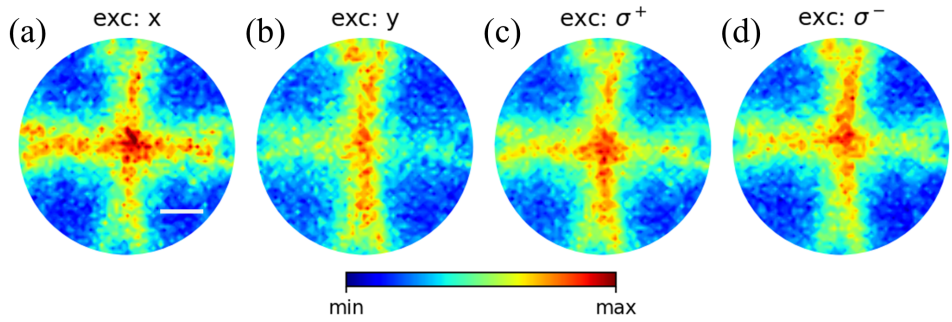

Figure 6.5. Farfield radiation patterns with (a) x, (b) y, (c) σ^+ and (d) σ^- polarized pump laser. The scale bar is 0.2 NA. The PL is filtered by a 630 nm band pass filter with FWHM of 10 nm. Valley-polarized exciton emission is coupled into different radiative channels depending on the polarization.

6.5 Conclusion

To summarize, we proposed a PhC slab with directional circular dichroism for separating valley-polarized exciton emission from a 3L WS_2 in the farfield. A perturbation is introduced to the PhC slab such that it breaks the in-plane inversion symmetry and creates directional circularly polarized radiative channels with opposite helicity. By integrating the 3L WS_2 with the PhC slab, valley-polarized exciton emission emits through the polarization-dependent radiative channels. As a result, this allows us to either separate the valley exciton emission on the detection side, or to selectively pump excitons from one valley to generate an asymmetric radiation pattern. Because of its capacity to direct exciton emission from distinct valleys into different directions, this PhC slab is an ideal platform for valley-based light emitters.

6.6 Acknowledgements

Chapter 6, in full, is currently being prepared for submission for publication of the material with title “Directing valley-polarized emission of 3L WS_2 by photonic crystal with

directional circular dichroism", by Wenzhuo Huang, Chawina De-Eknamkul, and Ertugrul Cubukcu. The dissertation author was the primary investigator and author of this paper.

Chapter 7

Self-resonant exciton-polaritonics in multi-layer WS_2

7.1 Overview

Room temperature stable excitons in layered 2D TMDCs offer a unique route for engineering light and matter interactions. The strong coupling between excitons in TMDCs and photons in an optical resonator generates a half-matter, half light quasiparticle called exciton-polariton. This hybridization brings about unique physical phenomena that includes large propagation distances, long-range coherence, and valley-coherent coupling. However, conventional approach in realizing exciton-polariton in TMDCs is through coupling with external resonators, which usually have a large volume that fundamentally limits the light–matter interaction with the atomically thin TMDCs [97, 163, 164].

In this chapter, we propose a monolithic 2D TMDC platform that uses the layered TMDCs themselves as the photonic resonator, which supports self-resonant exciton-polaritons. There are two major advantages. First, the strong excitonic effects in the layered 2D TMDCs give rise to a large excitonic oscillator strength [165], which in turn leads to extremely high refractive indices near the excitonic transition ($n > 5$). This provides an effective, yet unexplored

way to confine and manipulate light on the deep subwavelength scale in a dielectric platform. Secondly, the self-coupling scheme maximizes the exciton–photon coupling strength and pushes the resonant photonic device thickness down to few nanometers, which is beyond the cut-off thickness for resonators made out of conventional materials. In particular, there is no limit for the cut-off thickness in a symmetric waveguide with air on both side. This means that suspended 2D TMDCs can support guided mode even at monolayer limit.

7.2 Exciton-Polaritons in ultrathin WS_2 Photonic Crystal

In this section, we proposed an ultrathin ($\approx$ 12 nm) WS_2 photonic crystal directly fabricated on glass. As shown in Fig. 7.1a, an ultrathin WS_2 layer is patterned with a square array of air holes to construct the PhC slab, where the tightly bound excitons couple to the Fano-type photonic resonances in the patterned WS_2 itself and form self-resonant exciton-polaritons. Fig. 7.1b shows the optical microscopy and scanning electron microscopy (SEM) images of the sample. The excitonic and photonic resonances in the WS_2 PhC with a period Λ = 480 nm and a hole radius r = 120 nm can be seen from the transmission spectrum in Fig. 7.1c. Calculated spatial field profile for the photonic resonance (inset in Fig. 7.1c) indicates a large spatial overlap ($\approx$ 77%) with the WS_2 itself, which allows for the large exciton–photon coupling.

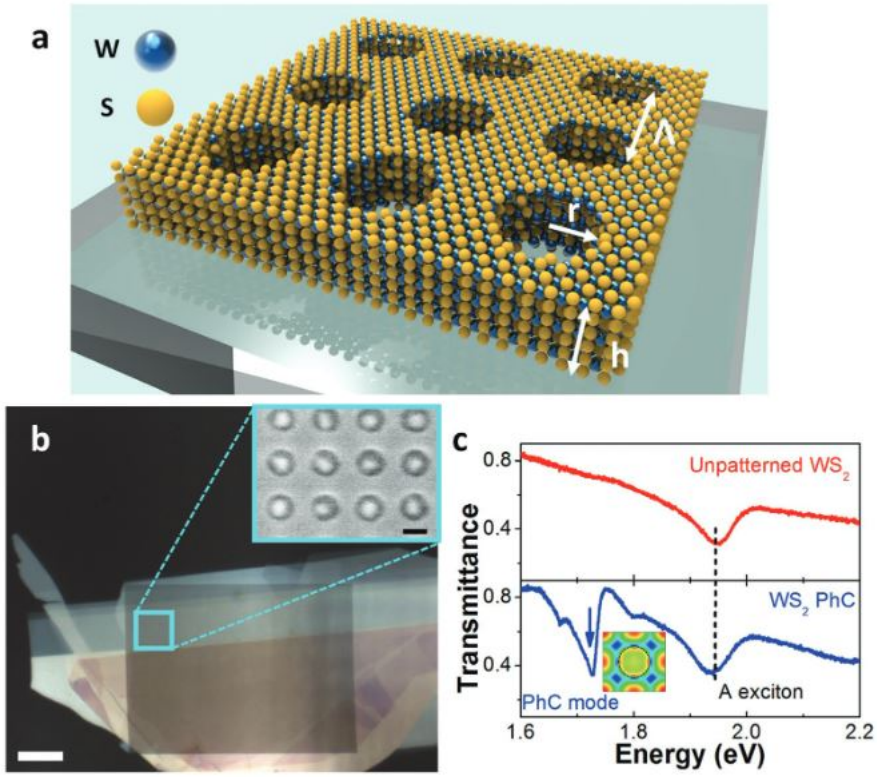

Figure 7.1. (a) Schematic of the WS_2 PhC slab. (b) Optical micrograph and SEM of the WS_2 PhC. (c) Transmittance of an unpatterned WS_2 slab and a WS_2 PhC slab with the same thickness (h = 13 nm).

The large refractive index is indispensable for light manipulation on the deep subwavelength scale. We first compare WS_2 with traditional materials for light guiding at λ = 640 nm (Fig. 7.2a). Because of the existence of the glass substrate, there is cut-off limit for the slab thickness, where WS_2 exhibits the smallest at around 8 nm. Moreover, compared with GaP at the same thickness of 15 nm, WS_2 presents higher effective index and a more confined electric field distribution (Fig. 7.2b). In addition, the large refractive index of WS_2 enables a shorter field decay length into air than that from the surface plasmon polariton mode of a gold-air interface, which is typically used as the "gold standard" for optical confinement of a guided mode (Fig. 7.2c).

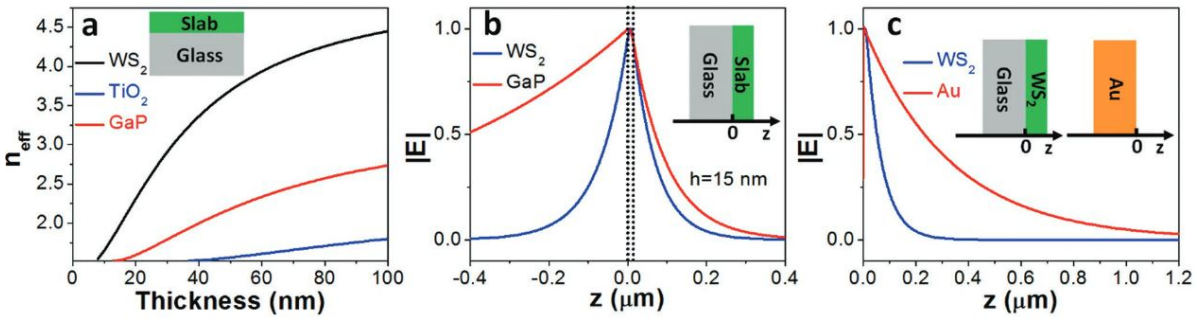

Figure 7.2. (a) Effective index as a function of thickness for slab waveguides of different materials. (b) Cross-sectional mode profiles at $\lambda = 640$ nm for slab waveguides. (c) Comparison to surface plasmon polariton (SPP) mode at gold-air interface.

As guided mode resonances in PhC depend on the incidence angle, we can study the coupling between the excitons and photons via angle-resolved transmission measurements. We first analyzed the angle resolved transmission spectra of a unpatterned WS_2 flake (Fig. 7.3a), whose A exciton absorption (1.94 eV) is angle independent. Because the WS_2 is only 12 nm thick, Fabry-Pérot resonances are within the ultraviolet range which is far way from the A exciton peak. Then we continue with a WS_2 PhC slab patterned with an array of holes (h = 12 nm, Λ = 300 nm, r = 120 nm). As we change the incidence angle from 20° to 40°, an anti-crossing behavior is clearly visible in Fig. 7.3b, which indicates the hybridization and self-resonant exciton-polaritons. We specifically focus on the spectrum in Fig. 7.3c measured at 33°, which corresponds to the anti-crossing of the photonic dispersion in Fig. 7.3d and the A exciton. By fitting the experimental data with three Lorentzian lineshapes, we can extract the upper (P+) and lower (P-) polariton components, plus a excitonic background. In Fig. 7.3e, we use the coupled-mode theory (Eq. 2.5) to calculate the Rabi splitting, a measure of coupling strength, which is as large as 100 meV. Because exciton-polariton is a part exciton, part photon quasiparticle, the composition of each component is also extracted from the dispersion. As

shown in Fig. 7.3f, the upper polariton mode changes from primarily photon-like at 20° to primarily exciton-like at 40°, indicating the energy exchange between excitons and photons.

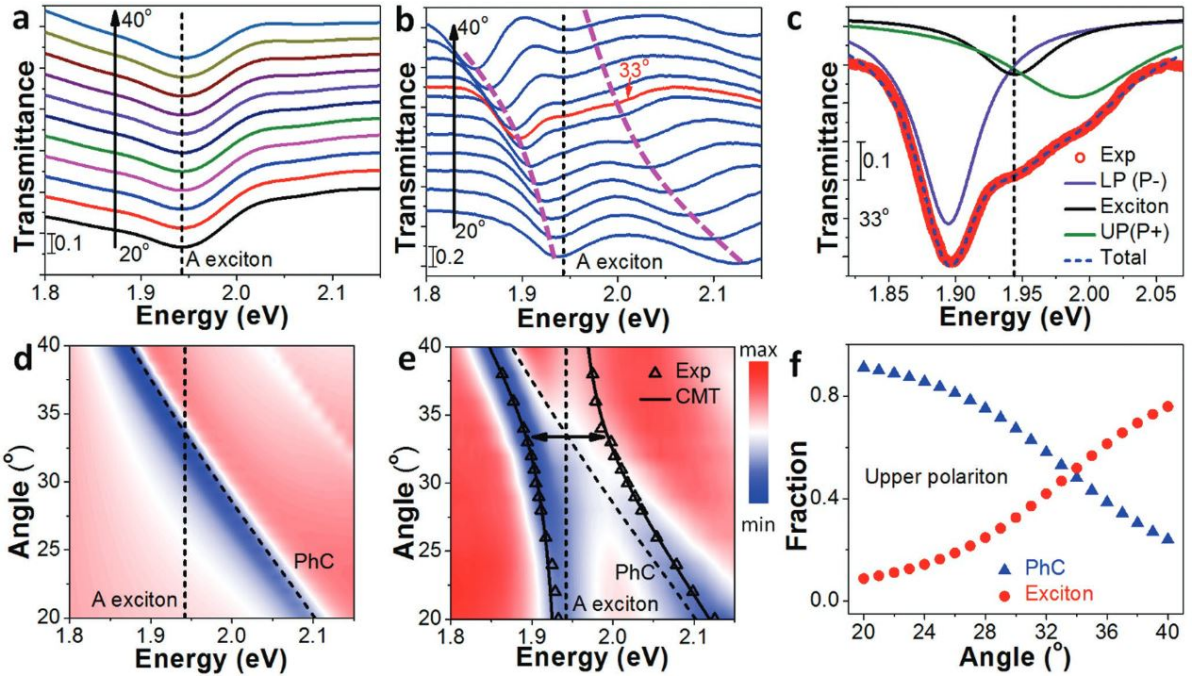

Figure 7.3. (a) Calculated transmittance for an unpatterned WS_2 slab (h = 12 nm). (b) Measured angle-resolved transmittance for the WS_2 PhC. (c) Fitting polariton peaks from transmittance. (d) Calculated transmittance for WS_2 PhC slab without excitonic resonance. (e) Avoided crossing in measured angle-resolved transmittance. (f) Composition of upper polariton.

Lastly, we demonstrated the ability of such WS_2 PhC with deep subwavelength thickness in enhancing 2D excitonic emission from a WSe_2 monolayer as shown in Fig. 7.4a. The transmission dip of the WS_2 PhC and the PL peak of the WSe_2 are aligned in Fig. 7.4b, which indicates a spectral overlap between the exciton mode in WSe_2 and the polariton mode (mostly photon-like) in the WS_2 PhC. The overall emission intensity is enhanced by eight times compared with the monolayer WSe_2 on glass (Fig. 7.5c). The angle-resolved transmission (Fig. 7.4d) and PL (Fig. 7.4e) spectra are measured to show that the PL from WSe_2 indeed couples with the photonic bands supported by the WS_2 PhC.

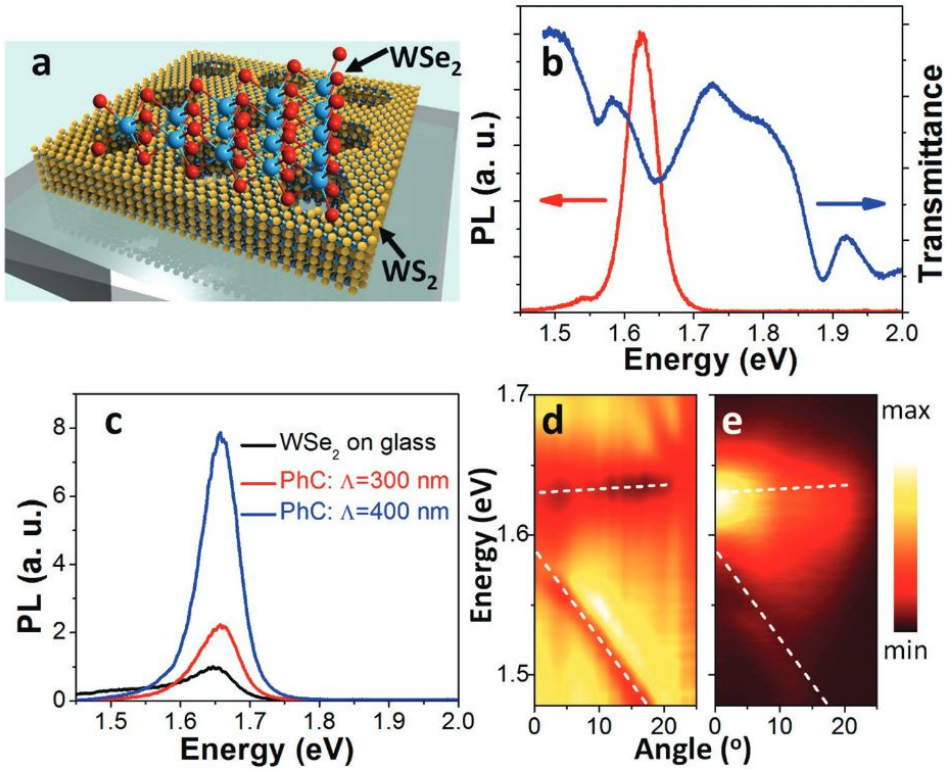

Figure 7.4. (a) Schematic of monolayer WSe_2 on an ultrathin WS_2 PhC. (b) The measured transmittance (blue) and the corresponding PL spectrum (red) from the integrated device. (c) The monolayer WSe_2 PL spectra on bare glass (black) and on WS_2 PhCs with Λ = 300 nm (red) and Λ = 400 nm (blue). Measured angle resolved (d) transmittance and (e) PL for the WS_2 PhC with Λ = 400 nm.

In summary, we proposed a monolithic 2D TMDC platform which is promising in manipulating exciton-polaritons at the subwavelength scale. This truly TMDC-based ultra-thin photonic structures will unfold the potential of exciton–polariton devices and provide new insights into the polaritonic phenomena in layered 2D TMDCs.

7.3 Directing exciton-polaritons in 3L WS_2 waveguide

In this section, we investigated the characteristics of 2D propagating exciton-polariton in a three-layer (3L) WS_2 waveguide. Because of the valley coherence in 3L WS_2, the linear

polarization of the excitation source is preserved by the coherent superposition of K and K' valley-polarized excitons, and the resulting PL emission possesses a preferred direction which corresponds to the transverse electric (TE) mode of the suspended flake.

Symmetric waveguide that is made out of suspended atomically thin WS_2 was proven to support guided mode in the visible spectrum. By adding a periodic array of holes to the suspended WS_2, the dispersion of the guided modes is folded back into the first Brillouin zone, which transform the guided modes into guided mode resonances that are available for farfield excitation and detection. By this means, we are not only able to observe the dispersion of the supported exciton-polaritons from transmission measurement, but we can also investigate the scattering properties of the guided mode resonance through farfield PL.

Fig. 7.5a illustrates a square array of air holes etched into the freestanding 2-nm-thick WS_2 supported by a SiN/Si window. Fig. 7.5b shows a scanning electron micrograph (SEM) of such suspended 3L WS_2 photonic crystal. The number of layers of the suspended WS_2 was confirmed via PL measurement in Fig. 7.5c, where two peaks at 630 nm and 785 nm correspond to direct and indirect bandgap transitions, respectively. With a period of 700 nm and hole diameter of 340 nm, we observe the guided mode resonance in transmission spectrum at normal incidence angle in Fig. 7.5d.

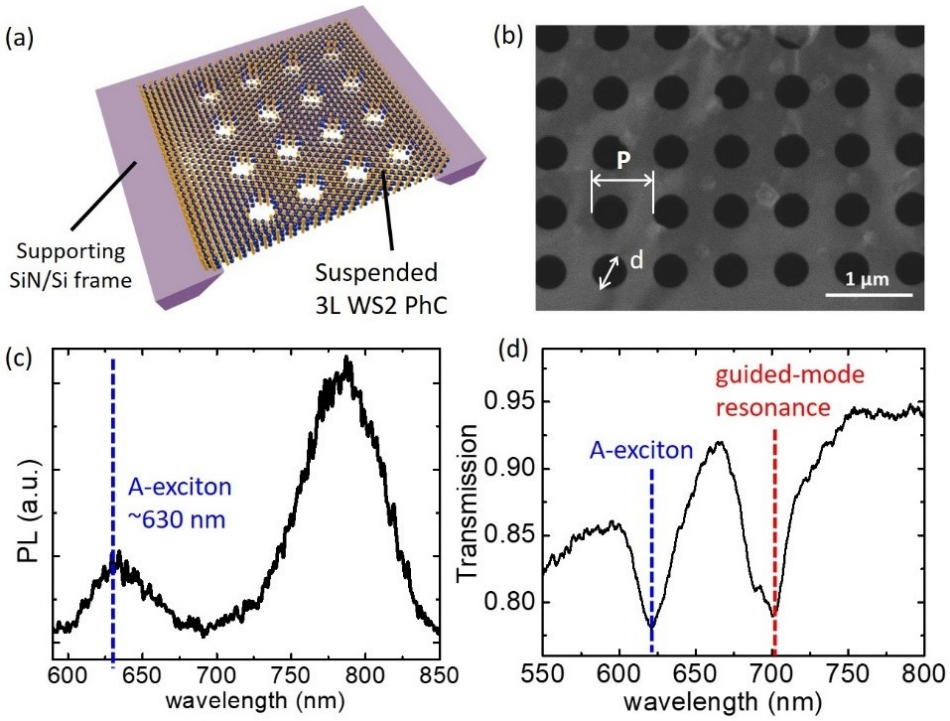

Figure 7.5. Schematic and sample characterization. (a) Free-standing 3L WS_2 PhC supported by a SiN/Si frame. (b) SEM of the suspended WS_2 PhC. (c) PL of suspended 3L WS_2 excited using a 532 nm laser. (d) Transmission spectrum of 3L WS_2 PhC with P = 700 nm and d = 340 nm.

We first performed angle-resolved transmission measurements using a collimated white light source to observe the dispersion of guided exciton-polaritonic resonances. Fig. 7.6a shows the transmission spectra measured at varying angles of incidence from 0° to 17°. As the guided mode resonance go across the excitonic resonance at 2.0 eV with an increased angle, the dispersion exhibits an anti-crossing behavior (black solid lines) which is a telltale of the strong light-matter interaction. We further analyzed the exciton-polariton dispersion in the color maps of simulated and experimental transmission spectra shown in Figs. 7.6b and 7.6c, respectively. The positions of exciton-polariton resonance were determined from Fig. 7.6c by fitting a Lorentzian curve over the angular spectrum at a fixed energy (black solid line). With

the momentum matching condition

$$n_{\text{eff}}^2 = \left(\frac{k_x}{k_0} + m\frac{2\pi}{\Lambda k_0}\right)^2 + \left(\frac{k_y}{k_0} + n\frac{2\pi}{\Lambda k_0}\right)^2, m,n = 0,\pm1,\pm2,\ldots \tag{7.1}$$

where Λ is the period of the WS_2 PhC, we can extract the effective index $\text{Re}\,(n_{\text{eff}})$ of the photon-like exciton-polariton mode as a function of wavelength in Fig. 7.6d.

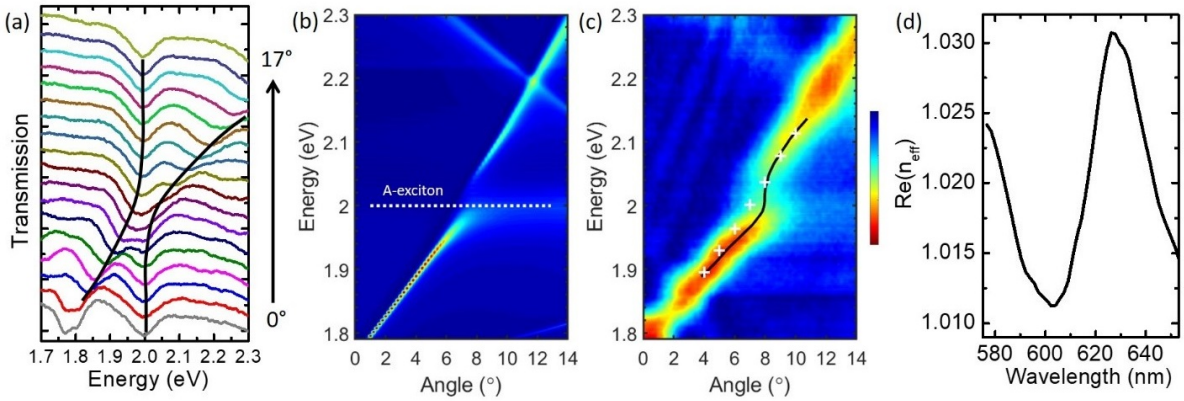

Figure 7.6. (a) Avoided crossing in transmission spectra of 3L WS_2 PhC at varying incidence angles. (b) Simulated and (c) experimental angle-resolved transmission spectra. (d) Real part of the effective index extracted from the dispersion in (c).

Next, we directly probed the propagation lengths of exciton-polariton in the 3L WS_2 waveguide using its own PL as a near-field emitter. As illustrated in Fig. 7.7a, an unpatterned area of suspended WS_2 was excited by a focused 532 nm laser with a spot size of approximately 500 nm. At a distance of r_1 away from the laser spot, we opened a narrow real-space aperture across the WS_2 PhC with a slit width of $\Delta r = r_2 - r_1 \approx 2\mu$m. As we fixed the aperture in the central area in the back focal plane (BFP), only the PL propagating within a certain angle was collected, regardless of the distance r_1. Because of the 2D nature of the guided propagation, the intensity distribution of the exciton-polariton from a point source should follow that of

a decaying cylinder wave by $\exp(-r/L_p)/r$, where L_p is the propagation length and r is the distance to the source. The total power of the scattered photons is proportional to the surface integral of the exciton-polariton intensity in the BFP by

$$I_{\mathrm{BFP}} \propto \int_{r_1}^{r_2} \frac{e^{-r/L_p}}{r} 2\theta r \mathrm{d}r \approx 2\theta \Delta r e^{-\bar{r}/L_p} \tag{7.2}$$

where r_1, r_2 and θ are as defined in Fig. 7.7a and $\bar{r} = (r_1 + r_2)/2$.

Fig. 7.7b shows the measured PL spectra collected from varying distances away from the pump spot. The PL intensity decreases exponentially as the distance increases, with each wavelength exhibiting varying decay constant which directly relates to the propagation length of the exciton-polaritons (Fig. 7.7c). As seen in Fig. 7.7d, L_p decreases to a minimum of $\sim 2\mu$m near the A-exciton energy and increases rapidly with decreased energy. The imaginary part of the effective index is extracted in Fig. 7.7e, as it is inversely proportional to the propagation length L_p of exciton-polariton by

$$\mathrm{Im}\,(n_{\mathrm{eff}}) = \frac{\lambda}{4\pi L_p}. \tag{7.3}$$

Having established the exciton-polariton dispersion, we continued to examine the polarization of the guided-mode resonance. The atomically WS_2 waveguide is TE in nature, with its electric field polarized in the plane of the material and perpendicular to the direction of propagation. By opening an aperture at a distance to the pump spot (Fig.7.8a), emission from propagating exciton-polaritons is measured at the back focal plane. As indicated by Eq. 7.1, the

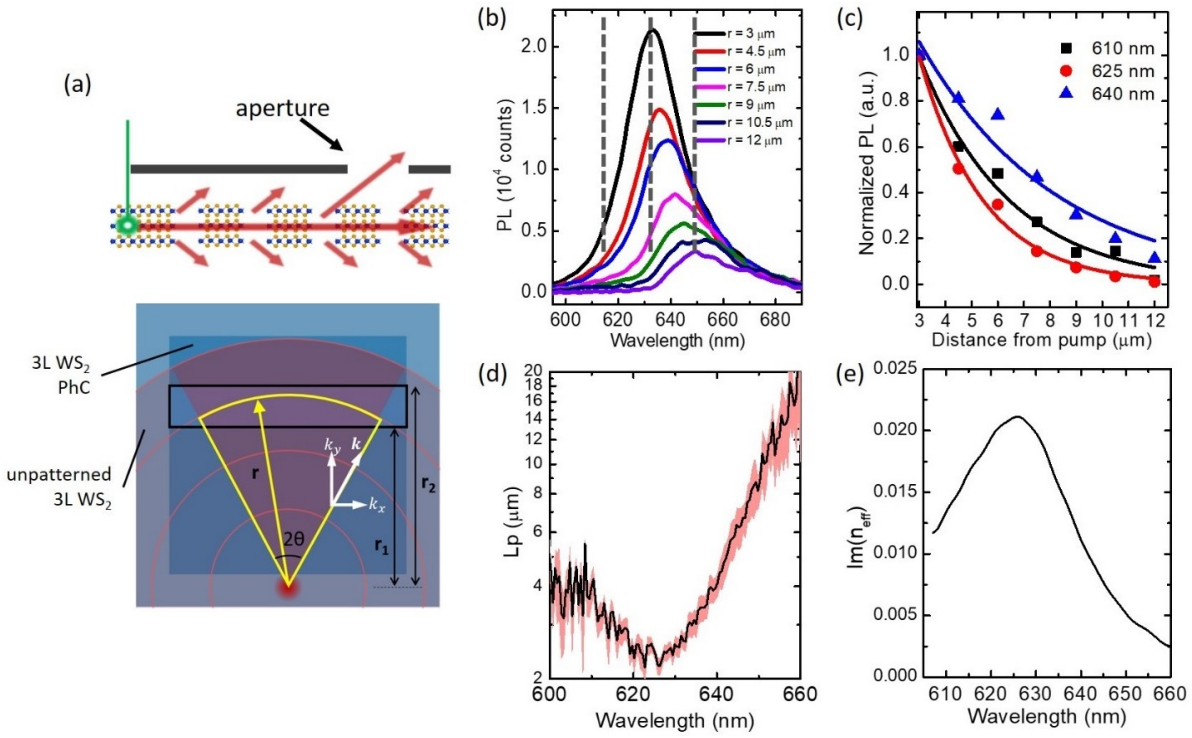

Figure 7.7. Propagation of exciton-polariton. (a) Experiment setup. (b) PL spectra measured away from the excitation spot. (c) PL intensities at 610 nm, 625 nm and 640 nm as a function of distance to the excitation spot. (d) Experimental propagation length (L_p) of exciton-polariton. (e) Imaginary part of the effective index calculated from (d).

back focal plane image of the scattered PL should be an arc centered at $(-m\frac{2\pi}{\Lambda k_0}, -n\frac{2\pi}{\Lambda k_0})$ with radius of n_{eff}. In Figs. 7.8b and 7.8c, the propagated PL in y direction shows an x polarized state indicated by the polarization of the analyzer, which agrees with its TE nature. Because of the valley coherence in 3L WS_2 as shown in Fig. 7.8d, the polarization of the propagating exciton-polaritons is mainly determined by the polarization state of the pump laser. Hence, x polarized pump should generate coherent exciton-polaritons whose emission is also x polarized, which propagates in y direction. This is verified in Figs. 7.8e and 7.8f, where pump polarization determines the major propagation direction of the excited exciton-polaritons.

In summary, we have demonstrated directional propagation of valley-coherent exciton-

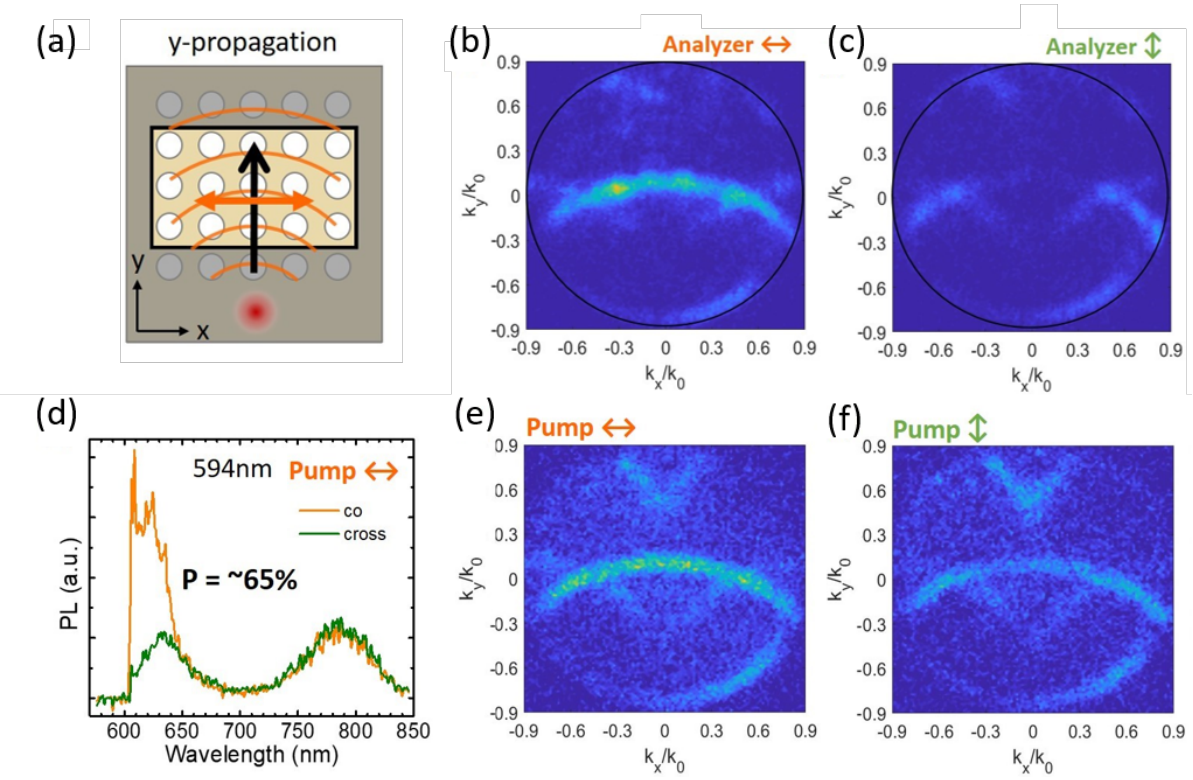

Figure 7.8. (a)Schematic of the measurement for *y* propagation. Measured back-focal plane emission with an (b) *x* and (c) *y* polarized analyzer, respectively. Measured back-focal plane emission with an (d) *x* and (e) *y* polarized pump, respectively.

polariton via guided mode resonance in a suspended 3L WS_2 PhC. This work provides a platform for manipulating valley excitons in coherent light-matter states in order to create exciton-polaritonic and valleytronic devices.

7.4 Acknowledgements

Chapter 7, in part, is a reprint of the material as it appears in Advanced Optical Materials, 2020, with title "Ultrathin WS_2-on-glass photonic crystal for self-resonant exciton-polaritonics", by Xingwang Zhang, Xiaojie Zhang, Wenzhuo Huang, Kedi Wu, Mengqiang Zhao, A. T. Charlie Johnson, Sefaattin Tongay, and Ertugrul Cubukcu. The dissertation author

was the co-investigator and co-author of this paper, with contribution in optical simulation and experimental data analysis.

Chapter 7, in part, is currently being prepared for submission for publication of the material with title “Directional propagation of self-resonant exciton-polariton in atomically thin WS_2 waveguide”, by Chawina De-Eknamkul, Wenzhuo Huang, Xingwang Zhang, and Ertugrul Cubukcu. The dissertation author was the co-investigator and co-author of this paper, with contribution in optical simulation, L_p measurement and experimental data analysis.

Chapter 8

Summary and outlook

8.1 Summary

In summary, this dissertation has demonstrated the enhanced light-matter interaction between excitons in 2D TMDCs and photonic resonances supported by photonic resonators. The integration of layered semiconductor materials and the 2D photonic crystal slabs has enabled enhanced light absorption and emission, as well as the control over the scattering properties that includes farfield directionality and polarization. This prototype of combining excitonic resonance and guided mode resonance in Chapter 4 can be brought to higher level with the development of new concepts such as bound states in continuum, singular optics and non-Hermiticity, and new designs such as photonic quasicrystals and topological photonic crystals. Chapter 5 provides an example along this path. By encircling a BIC with a ring of exceptional points, the polarization vortex is preserved while the dispersion of the PhC slab is drastically changed. 2D excitonic emission from these exotic states brings up possibilities of building an excitonic vortex laser.

In addition, Chapter 6 shows that the polarization dependent photonic resonances in PhC slabs can incorporate with the valley-polarized excitons, enabling valley selective emissions.

The ability of PhC slabs in controlling the spin degree of freedom of photons will benefit the light-matter coupling with excitons that carry valley pseudo-spin. On the one hand, photonic crystal can also be designed to present valley degree of freedom, whose interaction with valley excitons can be interesting. On the other hand, 2D semiconductors with other crystal structures such as SnS and SnSe have anisotropic electronic and optical properties, which may be leveraged by the photonic crystals that lack the same symmetry.

Finally, we demonstrated in Chapter 7 that 2D TMDCs themselves can also be made into resonant structures to support exciton-polaritons, a quasiparticle that characterizes the strong interaction between excitons and photons. This idea provides a solution to the limited spatial overlap between 2D TMDCs and photonic resonators in the out-of-plane direction. With the development of nanofabrication, resonators with higher complexity can be designed directly on the 2D TMDCs, which enables more compact nanodevices with added functionalities. For example, the high index of 2D TMDC is beneficial for wavefront engineering by flat optics, such as Mie resonators, metasurfaces and metalenses.

8.2 Outlook

Working in the interdisciplinary field between 2D materials and photonics for the past few years, I believe there is much undeveloped area that can be explored. Certainly, any major findings or advances on either side could lead to an evolution in this field, but the cross area is also worth devoting efforts to. Here, I will give a more comprehensive outlook beyond this dissertation in the following three perspectives: 2D semiconductors, photonics and their interception.

8.2.1 2D semiconductors

Although 2D semiconductors, or 2D materials in general have been studied for few decades, their real world applications still remain illusive. 2D semiconductors already show their advantages in certain aspects, but the high cost and hard-to-control quality hinder them from replacing traditional materials in the semiconductor industry. Nevertheless, they are still the building blocks for low dimensional devices and have been found to offer great potentials in chemical engineering, neuroscience and biology. Applications of 2D semiconductors in these areas mostly focus on their material properties, but rarely touch the state-of-the-art techniques in photonics. For example, in a TMDC-based sensor that monitors changes in optical signals (often transmission or reflection), the optical readout is usually not optimized. This means the sensing limit could benefit from the coupling with a photonic resonator nearby, as it can provide stronger intensity, higher spatial and spectral resolution, and faster interaction speed.

Another direction for TMDC-based sensors is to utilize excitonic emission from the material. As nanoscale interactions change the properties of the excitons, such as different A exciton/trion ratio or shift in binding energy, these information can be observed through the changes in PL intensity, lineshape or even valley coherence. Again, these designs can be optimized via incorporation of photonic resonators.

Dark excitons in 2D TMDCs do not need to follow optical selection rules as they are scattered by other particles or interactions. This makes prohibited states available for optical transitions and multi-photon processes. By integrating with optical resonators, these light-matter interactions can be enhanced at preferred wavelength for better device performance.

8.2.2 Photonics

Strong binding energy of excitons result in high refractive index and excitonic emission in 2D TMDCs, which are much used in TMDC-based photonic devices such as sensors, modulators and light emitters. With the emergence of non-Hermitian physics, the intrinsic loss and tuning capabilities in 2D TMDCs could be integrated with photonic devices with PT (anti-)symmetry, non-reciprocity, and exceptional points. For example, by tuning the loss in an integrated 2D TMDC, a non-Hermitian system could transition from PT symmetric phase to PT symmetry broken phase, which can be a prototype for non-reciprocal optical diodes. Topological photonics is another hot topic that attracts a lot of attention. By carefully designing the topology in the wavevector space, new photonic states that are topologically protected can be spawned in the interface. In particular, this suggests a unidirectional waveguide that is immune to perturbations and defects. By combining two photonic crystals with different Chern number, topological edge modes are supported at the interface, which present spin-momentum locking effect. This can be coupled with 2D TMDCs with valley pseudo-spin so that the excitonic emission from one valley can only propagate in one direction. Moreover, the ideas in topological photonics can be easily transferred to other Bosonic systems such as excitons and exciton-polaritons where 2D TMDCs are much involved.

8.2.3 Light-matter interaction

For light-matter interaction discussed in this dissertation, the emitters are not limited to 2D TMDCs, but they can also be quantum dots/wells, dye molecules, and other 2D semiconductors such as black phosphorus and tin sulfide. This provides more possibilities as

each emitter may have its own unique properties that can interact with the optical resonators. For instance, the integration of black phosphorus and photonic resonators can lead to infrared photodetectors with higher sensitivity, while the basic physical idea would be rather similar.

Exciton-polariton emerges when the light-matter interaction falls in the strong coupling regime. As both excitons in 2D TMDCs and photonic resonators have strong tuning capabilities, exciton-polariton can be explored in multiple ways. First, the excitonic resonance can be changed by temperature, chemical doping, external field and mechanical strain. These mechanisms can be associated with the exciton-polaritons for studies in condensed matter physics and possible sensing applications. Secondly, the tuning of photonic resonances could significantly modify the behaviors of the exciton-polaritons, such as dispersion relation and coherence length of the propagating polaritons. Lastly, the interplay of multiple mechanisms is of great importance to fundamental physics such as Bose-Einstein condensates and 2D superfluid behaviour.

At the end, recent advances in van der Waals heterostructures have enabled interlayer excitons that can also be studied via coupling with photonic resonances. Furthermore, by twisting the relative angle of stacked 2D materials, unusual electronic band structure can be observed at ”magic” angles. These crystals present a Moiré pattern (and Moiré superlattice) that has much larger scale than the crystal lattice, which could interact with photons with comparable wavelength. The associated Moiré excitons in twisted bilayer TMDCs may lead to unprecedented quantum phenomena.

Appendix A

Extracting refractive index and excitonic resonances of TMDCs

A.1 Transfer matrix method

For a multilayer structure, the transmission/reflection spectra can be calculated by Transfer-Matrix Method (TMM) given the complex refractive index $\widetilde{n}_m$ and thickness d_m of each layer:

$$\boldsymbol{T} = \boldsymbol{D}_0^{-1}\left[\prod_{m=1}^{N}\boldsymbol{D}_m\boldsymbol{P}_m\boldsymbol{D}_m^{-1}\right]\boldsymbol{D}_{N+1} = \begin{bmatrix} T_{11} & T_{12} \\ T_{21} & T_{22} \end{bmatrix} \tag{A.1}$$

where

$$\boldsymbol{D}_{m-1}^{-1}\boldsymbol{D}_m = \begin{bmatrix} 1 & r_{m-1,m} \\ r_{m-1,m} & 1 \end{bmatrix} / t_{m-1,m}$$

is the transmission matrix, and

$$\boldsymbol{P}_m = \begin{bmatrix} \exp(i\delta_m) & 0 \\ 0 & \exp(-i\delta_m) \end{bmatrix}$$

is the propagation matrix where $\delta_m = 2\pi\omega\widetilde{n}_m d_m/c$ is the complex phase. $r_{m-1,m}$ and $t_{m-1,m}$ are the reflection and transmission coefficients from $(m-1)^{\text{th}}$ to m^{th} layer, which are given by the generalized Fresnel's law:

$$r_{m-1,m} = \frac{\widetilde{n}_{m-1} - \widetilde{n}_m}{\widetilde{n}_{m-1} + \widetilde{n}_m} \tag{A.2}$$

$$t_{m-1,m} = \frac{2\widetilde{n}_{m-1}}{\widetilde{n}_{m-1} + \widetilde{n}_m} \tag{A.3}$$

The complex reflection and transmission coefficients of the multilayer can be expressed in terms of the system transfer matrix elements T_{ij} as

$$r = r_{0,N+1} = \frac{T_{21}}{T_{11}} \tag{A.4}$$

$$t = t_{0,N+1} = \frac{1}{T_{11}} \tag{A.5}$$

from which the reflectance R and transmittance T can be obtained by the absolute square of the complex coefficients r and t, respectively.

For short, the transmission and reflection spectra of a multilayer structure that includes a 2D TMDC can be expressed as a function of the flake's refractive index

$$T = T\left(\widetilde{n}(\omega), \omega\right) \tag{A.6}$$

$$R = R\left(\widetilde{n}(\omega), \omega\right) \tag{A.7}$$

where $\widetilde{n} = n + i\kappa = \sqrt{\widetilde{\varepsilon}_r(\omega)}$ can be modeled by Lorentz oscillator model

$$\widetilde{\varepsilon}_r(\omega) = 1 + \sum_n \frac{A_n}{\omega_n^2 - \omega^2 - i\gamma_n\omega} \tag{A.8}$$

where A_n, ω_n and γ_n are the strength, central frequency and width of the n^{th} oscillator, respectively.

In the experiment, we can measure the reflection spectrum of the multilayer structure $R_{\exp}(\omega_i)$ and the thickness d of the flake (for example by Atomic Force Microscope). By minimizing the Mean Square Error (MSE $= \sum_i \left[R_{exp}(\omega_i) - R\left(\widetilde{\widehat{n}}(\omega_i), \omega_i\right)\right]^2$) of the reflectance, we can find the optimal values of the parameters $\widehat{A}_n$, $\widehat{\omega}_n$ and $\widehat{\gamma}_n$, which uniquely determine the extracted refractive index $\widehat{n}(\omega)$ and the extinction coefficient $\widehat{\kappa}(\omega)$ by

$$\hat{n}(\omega) + i\hat{\kappa}(\omega) = \sqrt{1 + \sum_n \frac{\hat{A}_n}{\hat{\omega}_n^2 - \omega^2 - i\hat{\gamma}_n\omega}} \tag{A.9}$$

A.2 Point-by-point fitting

Transfer matrix method can also be used to calculate transmission/reflection when there is an incidence angle. Depending on the polarization, we can replace the matrix element by

$$r^s_{m-1,m} = \frac{\widetilde{n}_{m-1}\cos(\theta_{m-1}) - \widetilde{n}_m\cos(\theta_m)}{\widetilde{n}_{m-1}\cos(\theta_{m-1}) + \widetilde{n}_m\cos(\theta_m)} \tag{A.10}$$

$$t^s_{m-1,m} = \frac{2\widetilde{n}_{m-1}\cos(\theta_{m-1})}{\widetilde{n}_{m-1}\cos(\theta_{m-1}) + \widetilde{n}_m\cos(\theta_m)} \tag{A.11}$$

and

$$r^{p}_{m-1,m} = \frac{\widetilde{n}_{m-1}\cos(\theta_m) - \widetilde{n}_m\cos(\theta_{m-1})}{\widetilde{n}_{m-1}\cos(\theta_m) + \widetilde{n}_m\cos(\theta_{m-1})} \tag{A.12}$$

$$t^{p}_{m-1,m} = \frac{2\widetilde{n}_{m-1}\cos(\theta_{m-1})}{\widetilde{n}_{m-1}\cos(\theta_m) + \widetilde{n}_m\cos(\theta_{m-1})}, \tag{A.13}$$

where the incidence angle for each layer is determined by law of refraction

$$\widetilde{n}_{m-1}\sin(\theta_m) = \widetilde{n}_1\sin(\theta_1). \tag{A.14}$$

Note that because $\widetilde{n}$ is complex, θ is also complex.

Now the reflection and transmission spectra are functions of incidence angle and flake thickness

$$T = T(\widetilde{n}(\omega), \omega, \theta, h) \tag{A.15}$$

$$R = R(\widetilde{n}(\omega), \omega, \theta, h). \tag{A.16}$$

By measuring same sample at multiple angles, or multiple samples with different thickness, we can fit $\widetilde{n}$ at each frequency point.

A.2.1 Fitting by angle

We find $\widetilde{n}$ by minimizing MSE $= \sum_i \left[T(\varepsilon_1, \varepsilon_2, \theta_i) - T_{\exp}(\theta_i)\right]^2$ through ε_1 and ε_2.

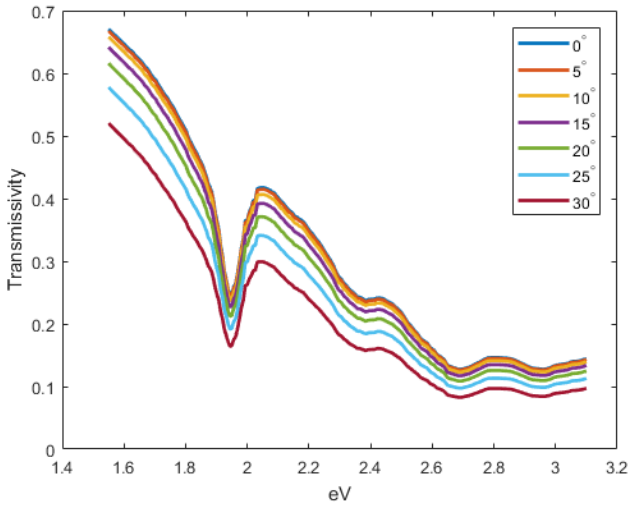

Figure A.1. Transmission spectra at 0° to 30°.

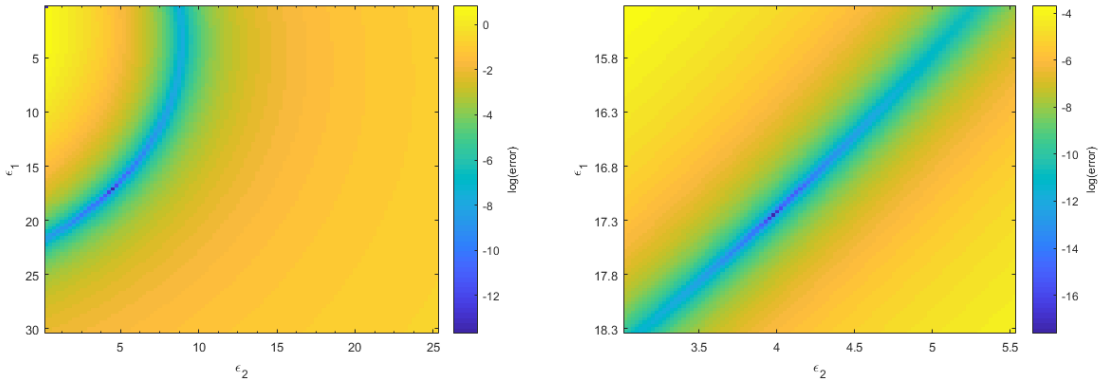

Figure A.2. Map of MSE with different ε_1 and ε_2 at 2.06 eV. The minimum MSE appears at $\widehat{\varepsilon}_1$ = 17.172 and $\widehat{\varepsilon}_2$ = 3.985.

A.2.2 Fitting by thickness

Similarly, for bulk WS_2, we can measure normal transmission/reflection spectra of samples with different thickness, and extract ε_1 and ε_2 by minimizing $\text{MSE} = \sum_i \left[T(\varepsilon_1, \varepsilon_2, h_i) - T_{\text{exp}}(h_i)\right]^2$. The extracted results show good agreement with the reference permittivity from 1.7 eV to 2.3 eV (540 nm to 730 nm).

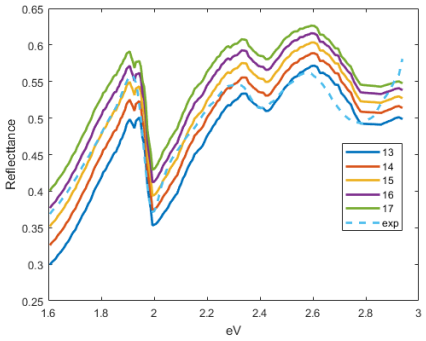

(a) $h_{\mathrm{AFM}} = 16$ nm.

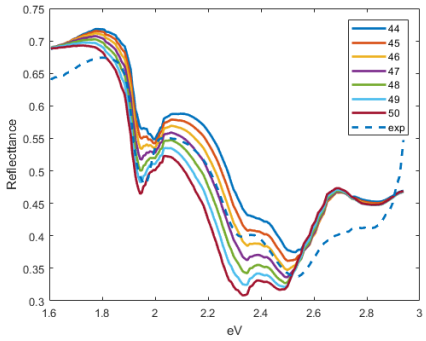

(b) $h_{\mathrm{AFM}} = 48$ nm.

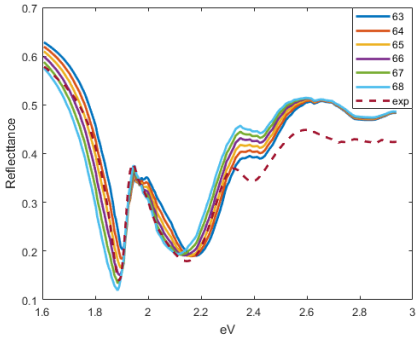

(c) $h_{\mathrm{AFM}} = 70$ nm.

Figure A.3. Thin film reflection spectra measured at different thickness compared with calculated reflectance with reference refractive index.

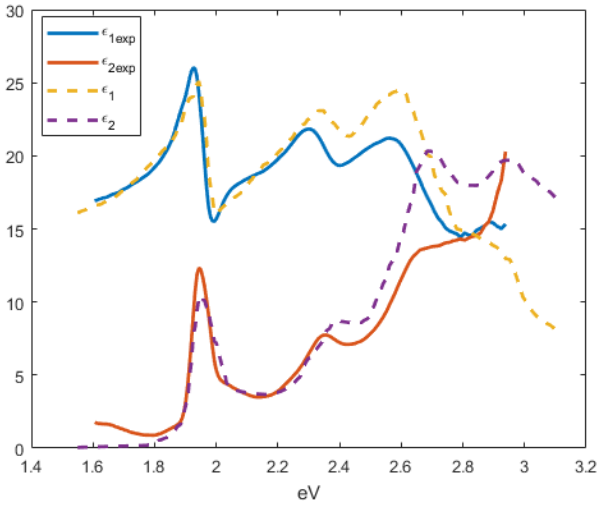

Figure A.4. Fitted permittivity from experimental result versus reference permittivity.

Appendix B

More on temporal coupled-mode theory

B.1 Transmission spectrum

B.1.1 Multiple resonances without non-radiative loss

In PhC slabs, there are usually multiple modes within the spectral range of interest. In this subsection, we consider a general case with n resonances and m ports. The resonance amplitudes become a vector $\boldsymbol{a} = (a_1, a_2, ..., a_n)^T$, and the resonance frequencies become a $n \times n$ matrix, which can be diagonalized to $\Omega = \text{diag}(\omega_1, \omega_2, ..., \omega_n)$. The dynamic equations for such system are written as

$$\frac{\mathrm{d}\boldsymbol{a}}{\mathrm{d}t} = (j\Omega - \Gamma)\boldsymbol{a} + K^T|s_+\rangle \tag{B.1}$$

$$|s_-\rangle = C|s_+\rangle + D\boldsymbol{a} \tag{B.2}$$

where $|s_\pm\rangle$ are the incoming and outgoing waves defined in the same way as subsection 3.2.1, K and D are $m \times n$ coupling matrices defined as $K = [k_{ij}]_{m\times n}$ and $D = [D_{ij}]_{m\times n}$ with $i = 1, 2, ...m$

and $j = 1, 2, ..., n$. The constraints for K and D still apply

$$D^{\dagger} D = 2\Gamma \tag{B.3}$$

$$K = D \tag{B.4}$$

$$CD^{*} = -D \tag{B.5}$$

The scattering matrix is thus

$$S = C + D[j(\omega I - \Omega) + \Gamma]^{-1} K^{T}. \tag{B.6}$$

As an example, for a system with two ports and two resonances with the same symmetry, we have

$$\Omega = \begin{bmatrix} \omega_1 & 0 \\ 0 & \omega_2 \end{bmatrix}, \Gamma = \begin{bmatrix} \gamma_1 & \gamma_0 \\ \gamma_0^{*} & \gamma_2 \end{bmatrix}, C = \begin{bmatrix} r_d & t_d \\ t_d & r_d \end{bmatrix}, D = \begin{bmatrix} d_{11} & d_{12} \\ d_{21} & d_{22} \end{bmatrix}. \tag{B.7}$$

The transmission coefficient is calculated as

$$t = t_d \mp \frac{(r_d \pm t_d)[\gamma_1(j\omega - j\omega_2) + \gamma_2(j\omega - j\omega_1)]}{(j\omega - j\omega_1 + \gamma_1)(j\omega - j\omega_2 + \gamma_2) - \gamma_1\gamma_2}. \tag{B.8}$$

B.1.2 Two coupled resonances with non-radiative loss

In Chapter 5, we considered a dipolar mode and a quadrupolar mode with complex frequencies $\widetilde{\omega}_{1,2} = \omega_{1,2} + i\gamma_{1,2}$ respectively at the Γ point. When in-plane momentum $\boldsymbol{k}$ deviates

from the Γ point, the coupling between these two modes come into play. A general Hamiltonian for the system is written as[1]

$$\mathscr{H} = \begin{pmatrix} \omega_1 & \kappa \\ \kappa & \omega_2 \end{pmatrix} - i \begin{pmatrix} \gamma_1 & \gamma_{12} \\ \gamma_{12} & \gamma_2 \end{pmatrix} - i \begin{pmatrix} \eta_1 & 0 \\ 0 & \eta_2 \end{pmatrix} \tag{B.9}$$

where $\kappa = \beta|\boldsymbol{k}|$ is the coupling strength which is proportional to the deviation $\boldsymbol{k}$, $\gamma_{1,2}$ is the radiative loss ($\gamma_{12} = \sqrt{\gamma_1\gamma_2}$) and $\eta_{1,2}$ is the non-radiative loss for each mode.

The eigenvalues for this generalized Hamiltonian are solved as

$$\begin{aligned} \omega_\pm = & \frac{\omega_1 + \omega_2}{2} - i\frac{\gamma_1 + \gamma_2 + \eta_1 + \eta_2}{2} \\ & \pm \sqrt{(\kappa - i\gamma_{12})^2 - \left(\frac{\gamma_1 - \gamma_2 + \eta_1 - \eta_2}{2} - i\frac{\omega_1 - \omega_2}{2}\right)^2} \end{aligned} \tag{B.10}$$

At an exceptional point, $\omega_1 = \omega_2$. This requires a zero inside the square root, which yields

$$\kappa = \frac{\gamma_1 - \gamma_2 + \eta_1 - \eta_2}{2} \tag{B.11}$$

$$\gamma_{12} = \frac{\omega_1 - \omega_2}{2} \tag{B.12}$$

these are the strict conditions for an exceptional point. Practically, because the first condition happens at a very small $\boldsymbol{k}$, the radiative loss for the quadrupole-like mode is close to zero, and γ_{12} is negligible.

Similar to Eq. B.8, the transmission and reflection spectra can be calculated through

[1] In this subsection, we use the physic notation i for the complex number.

TCMT,

$$T(\omega) = |t_d + (t_d + r_d)g(\omega)|^2 \tag{B.13}$$

$$R(\omega) = |r_d + (t_d + r_d)g(\omega)|^2 \tag{B.14}$$

where $g(\omega)$ is given by

$$g(\omega) = i\frac{\gamma_1(\omega_2 - i\eta_2 - \omega) + \gamma_2(\omega_1 - i\eta_1 - \omega) - 2\gamma_{12}\kappa}{(\omega_1 - i\gamma_1 - i\eta_1 - \omega)(\omega_2 - i\gamma_2 - i\eta_2 - \omega) - (\kappa - i\gamma_{12})^2} \tag{B.15}$$

or equivalently

$$g(\omega) = \frac{(\omega'_+ - \omega)(\omega'_- - \omega)}{(\omega_+ - \omega)(\omega_- - \omega)} - 1 \tag{B.16}$$

where $\omega'_\pm$ are the eigenvalues of the Hamiltonian without radiative loss ($\gamma = 0$):

$$\omega'_\pm = \frac{\omega_1 + \omega_2}{2} - i\frac{\eta_1 + \eta_2}{2} \pm \sqrt{\kappa^2 - \left(\frac{\eta_1 - \eta_2}{2} - i\frac{\omega_1 - \omega_2}{2}\right)^2} \tag{B.17}$$

Then we can rewrite the transmission spectrum in a more compact way:

$$\begin{aligned} T(\omega) =& \left|(t_d + r_d)\frac{(\omega'_+ - \omega)(\omega'_- - \omega)}{(\omega_+ - \omega)(\omega_- - \omega)} - r_d\right|^2 \\ =& \frac{\left|(t_d + r_d)(\omega'_+ - \omega)(\omega'_- - \omega) - r_d(\omega'_+ - \omega)(\omega'_- - \omega)\right|^2}{\left|(\omega_+ - \omega)(\omega_- - \omega)\right|^2} \\ =& A\frac{(\omega - \omega_a)^2}{|\omega - \omega_+|^2} + B\frac{(\omega - \omega_b)^2}{|\omega - \omega_-|^2} + C \end{aligned} \tag{B.18}$$

where A, B, C, $\omega_{a,b}$ are all real numbers. Because the numerator in the second line is a

polynomial of ω with degree of 4, which has five coefficients (from ω^0 to ω^4), we should in general be able to replace them with the expression in the third line which also creates a polynomial with the same degree of 4. Here $|\omega-\omega_\pm|^2=(\omega-\mathrm{Re}\{\omega_\pm\})^2+(\mathrm{Im}\{\omega_\pm\})^2$. The reason why we write $T(\omega)$ in this way is that it consists of two independent Fano lineshapes, whose centers and linewidths yield exactly the complex eigenvalues of the system, regardless of the fitting parameters A, B, C and $\omega_{a,b}$.

For reflection and absorption, since they both have a 4$^{\text{th}}$ degree polynomial in the numerator, they can be written as

$$R(\omega)=A'\frac{(\omega-\omega_a')^2}{|\omega-\omega_+|^2}+B'\frac{(\omega-\omega_b')^2}{|\omega-\omega_-|^2}+C' \tag{B.19}$$

$$A(\omega)=A''\frac{(\omega-\omega_a'')^2}{|\omega-\omega_+|^2}+B''\frac{(\omega-\omega_b'')^2}{|\omega-\omega_-|^2}+C'' \tag{B.20}$$

To justify this hypothesis, we randomly generate a set of parameters in the Hamiltonian and simulate the T/R/A spectra using realistic t_d and r_d. Then, we fit these spectra using two Fano lineshapes plus a constant background. The fitted curves show perfect match with all three spectra, and the fitted eigenvalues for both Fano resonances are exactly the same from the spectra.

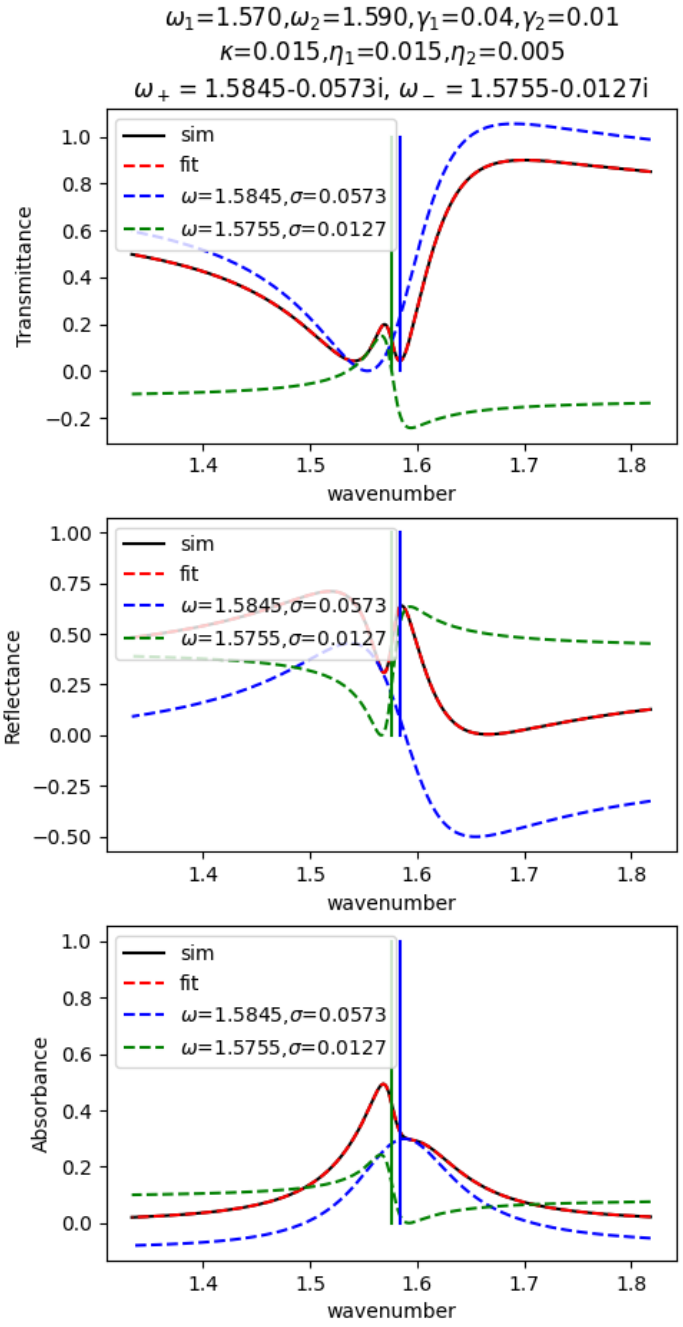

Figure B.1. Fitting a hypothetical resonator with two coupled modes by two Fano resonances.

These results demonstrate the feasibility to fit the transmission spectra of two coupled resonances, even if there exists non-radiative loss in the resonator.

B.2 Farfield polarization

Previously we focus on the scattering spectra associated with the guided mode resonances in PhC slabs. By separating orthogonal polarizations as independent ports, TCMT can also be used to predict the farfield polarization of the outgoing waves.

B.2.1 PhC slab with C_2 symmetry

We start with a PhC slab with up-down symmetry (σ_z) and in-plane inversion symmetry (C_2). We consider two polarizations (s and p) and two directions in $\pm z$. So there are four ports in the system. The dynamic equations are given by Eqs. 3.18 and 3.19:

$$\frac{\mathrm{d}a}{\mathrm{d}t} = (j\omega_0 - \gamma)a + (\langle\kappa|^*)|s^+\rangle \tag{B.21}$$

$$|s^-\rangle = C|s^+\rangle + a|d\rangle \tag{B.22}$$

where $|s^\pm\rangle = (s_s^{u\pm}, s_s^{d\pm}, s_p^{u\pm}, s_p^{d\pm})^T$ are the incoming and outgoing waves in s and p polarizations in upper (up) and lower (down) space, $\langle k|^* = (k_s^u, k_s^d, k_p^u, k_p^d)^T$ and $|d\rangle = (d_s^u, d_s^d, d_p^u, d_p^d)^T$ the coupling coefficients for incoming and outgoing waves, respectively.

Due to the up-down symmetry, $d^u = \sigma d^d$ with $\sigma = \pm 1$ for TE-like and TM-like

resonances, respectively. So we can use d_s and d_p to represent $|d\rangle$ via

$$|d\rangle = \begin{pmatrix} 1 & 0 \\ \sigma & 0 \\ 0 & 1 \\ 0 & \sigma \end{pmatrix} \begin{pmatrix} d_s \\ d_p \end{pmatrix}. \tag{B.23}$$

The direct scattering matrix C is given by transmission and reflection coefficients in s and p polarizations:

$$C = \begin{pmatrix} r_s & t_s & 0 & 0 \\ t_s & r_s & 0 & 0 \\ 0 & 0 & r_p & t_p \\ 0 & 0 & t_p & r_p \end{pmatrix}. \tag{B.24}$$

Now we derive the conclusion in Eq. 3.24. When $|s^+\rangle = 0$, $|s^-\rangle = a|d\rangle$. In a time-reversal process, with incident field $(a|d\rangle)^*$ and resonance amplitude a^*, there should be no outgoing wave, which yields

$$C|d\rangle^* = -|d\rangle \tag{B.25}$$

or in matrix form,

$$\begin{pmatrix} r_s & t_s & 0 & 0 \\ t_s & r_s & 0 & 0 \\ 0 & 0 & r_p & t_p \\ 0 & 0 & t_p & r_p \end{pmatrix} \begin{pmatrix} 1 & 0 \\ \sigma & 0 \\ 0 & 1 \\ 0 & \sigma \end{pmatrix} \begin{pmatrix} d_s^* \\ d_p^* \end{pmatrix} = - \begin{pmatrix} 1 & 0 \\ \sigma & 0 \\ 0 & 1 \\ 0 & \sigma \end{pmatrix} \begin{pmatrix} d_s \\ d_p \end{pmatrix}. \tag{B.26}$$

Hence the coupling coefficients are related to the direct scattering coefficients

$$(r_s + \sigma t_s) d_s^* = d_s \tag{B.27}$$

$$(r_p + \sigma t_p) d_p^* = d_p. \tag{B.28}$$

After combining the above two equations, we get the relative phase between d_s and d_p via

$$\arg\left(\frac{d_s}{d_p}\right) = \frac{1}{2}\arg\left(\frac{r_s + \sigma t_s}{r_p + \sigma t_p}\right) + N\pi \tag{B.29}$$

B.2.2 PhC slab with broken C_2 symmetry

Now we consider a PhC slab without in-plane inversion symmetry (broken C_2). Similar to the previous subsection, we first calculate the outgoing wave from a guided resonance without any incoming wave. Because the PhC slab lacks inversion symmetry, two opposite propagation directions $\boldsymbol{k}_\parallel$ are nonequivalent. The outgoing wave is given by $|s^-(\boldsymbol{k}_\parallel)\rangle = a|d(\boldsymbol{k}_\parallel)\rangle$. Then we set its time-reversal as the incident wave, plus the time-reversal of the guided resonance to get a zero outgoing wave in $-\boldsymbol{k}_\parallel$ direction:

$$0 = C(-\boldsymbol{k}_\parallel)\left(a|d(\boldsymbol{k}_\parallel)\rangle\right)^* + a^*|d(-\boldsymbol{k}_\parallel)\rangle \tag{B.30}$$

which, after cancelling a^*, yields

$$(r_s + \sigma t_s) d_s^*(-\boldsymbol{k}_\parallel) = d_s(\boldsymbol{k}_\parallel) \tag{B.31}$$

$$(r_p + \sigma t_p) d_p^*(-\boldsymbol{k}_\parallel) = d_p(\boldsymbol{k}_\parallel). \tag{B.32}$$

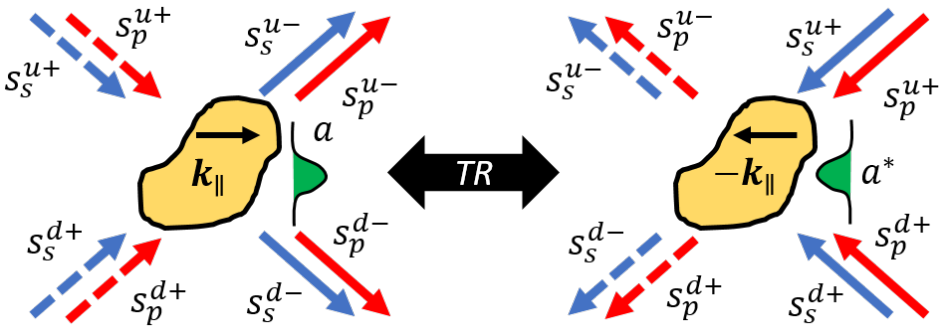

Figure B.2. Time reversal of a guided resonance and corresponding incoming/outgoing waves. Dashed lines mean zero amplitude.

Notice that for direct scattering matrix we have $C(\boldsymbol{k}_\parallel) = C(-\boldsymbol{k}_\parallel)$, because it treats the PhC slab as a homogeneous slab in which all directions with the same incidence angle are equivalent. Therefore, we can extract the phase constraints for d_s and d_p separately

$$\frac{d_s(\boldsymbol{k}_\parallel) d_s(-\boldsymbol{k}_\parallel)}{|d_s(-\boldsymbol{k}_\parallel)|^2} = r_s + \sigma t_s \tag{B.33}$$

$$\frac{d_p(\boldsymbol{k}_\parallel) d_p(-\boldsymbol{k}_\parallel)}{|d_p(-\boldsymbol{k}_\parallel)|^2} = r_p + \sigma t_p \tag{B.34}$$

or as a whole

$$\arg\left[\frac{d_s\left(\boldsymbol{k}_\parallel\right) d_s\left(-\boldsymbol{k}_\parallel\right)}{d_p\left(\boldsymbol{k}_\parallel\right) d_p\left(-\boldsymbol{k}_\parallel\right)}\right] = \arg\left(\frac{r_s + \sigma t_s}{r_p + \sigma t_p}\right) \tag{B.35}$$

which gives Eq. 6.3 in Chapter 6. This joint constraint of the polarization states gives us more

room to manipulate the farfield radiation as $d(\boldsymbol{k}_{\parallel})$ and $d(-\boldsymbol{k}_{\parallel})$ can change simultaneously by an opposite phase while total phase remains unaffected.

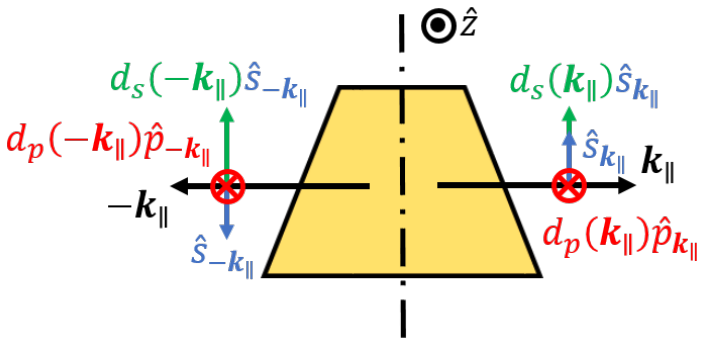

Figure B.3. $\pm\boldsymbol{k}_{\parallel}$ directions become nonequivalent under broken C_2 symmetry.

To prove Eq. 6.3, we create a hypothetical structure that has mirror symmetry but no inversion symmetry in Fig. B.3. $\hat{s}$ is the unit vector that is parallel with the plane (defined as $\hat{s} = \hat{z} \times \hat{k}_{\parallel}$) and $\hat{p}$ is defined as $\hat{p} = \hat{s} \times \hat{k}$, where $\hat{k}$ is the direction of the $\boldsymbol{k}$ vector. When the in-plane k vectors $\pm\boldsymbol{k}_{\parallel}$ are perpendicular to the mirror plane, there should be $d_s(\boldsymbol{k}_{\parallel})\hat{s}_{\boldsymbol{k}_{\parallel}} = d_s(-\boldsymbol{k}_{\parallel})\hat{s}_{-\boldsymbol{k}_{\parallel}}$ and $d_p(\boldsymbol{k}_{\parallel})\hat{p}_{\boldsymbol{k}_{\parallel}} = d_p(-\boldsymbol{k}_{\parallel})\hat{p}_{-\boldsymbol{k}_{\parallel}}$. Since there are $\hat{s}_{k_{\parallel}} = -\hat{s}_{-k_{\parallel}}$ and $\hat{p}_{\boldsymbol{k}_{\parallel}} = \hat{p}_{-\boldsymbol{k}_{\parallel}}$, d_s and d_p should satisfy

$$d_s(\boldsymbol{k}_{\parallel}) = -\, d_s(-\boldsymbol{k}_{\parallel}), \tag{B.36}$$

$$d_p(\boldsymbol{k}_{\parallel}) = d_p(-\boldsymbol{k}_{\parallel}). \tag{B.37}$$

Plug these in Eq. B.35, we get

$$\arg\left[-\left(\frac{d_s\left(\boldsymbol{k}_{\parallel}\right)}{d_p\left(\boldsymbol{k}_{\parallel}\right)}\right)^2\right] = \arg\left(\frac{r_s+\sigma t_s}{r_p+\sigma t_p}\right), \tag{B.38}$$

or

$$\arg\left[\frac{d_s\left(\boldsymbol{k}_{\parallel}\right)}{d_p\left(\boldsymbol{k}_{\parallel}\right)}\right]=\frac{1}{2}\arg\left(\frac{r_s+\sigma t_s}{r_p+\sigma t_p}\right)+\left(N+\frac{1}{2}\right)\pi \tag{B.39}$$

$$\arg\left[\frac{d_s\left(-\boldsymbol{k}_{\parallel}\right)}{d_p\left(-\boldsymbol{k}_{\parallel}\right)}\right]=\frac{1}{2}\arg\left(\frac{r_s+\sigma t_s}{r_p+\sigma t_p}\right)+\left(N-\frac{1}{2}\right)\pi. \tag{B.40}$$

This means when $\arg\left(\frac{r_s+\sigma t_s}{r_p+\sigma t_p}\right)\sim 0$, $d_s(\pm\boldsymbol{k}_{\parallel})$ and $d_s(\pm\boldsymbol{k}_{\parallel})$ would have $\pm\pi/2$ (or $\mp\pi/2$) phase difference, which represent elliptically polarized modes with opposite helicity.

Appendix C

Optical setup for experiment

C.1 Confocal microscopy and spectroscopy

For real space imaging, we place a 75 mm lens in between the back focal plane and the entrance slit of the spectrometer, whose distance is 150 mm. This is half of a $4f$ system (the other part is not shown in the Fig. C.1a for simplicity). Photons generated from *same position* in the sample plane are imaged onto a same spot on the charge-coupled device (CCD) camera which is conjugate to the entrance slit.

For back focal plane imaging, we use a Bertrand lens with shorter focal length instead, so that the back focal plane and the spectrometer entrance slit are now conjugate planes. Photons emitted at the *same angle* from the sample plane will be focused onto the same spot on the CCD camera.

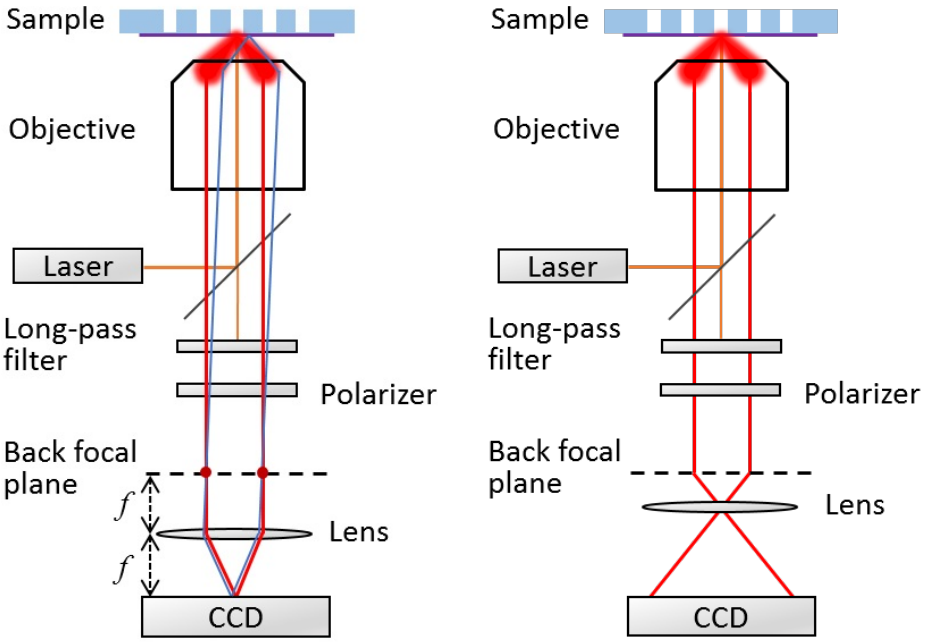

(a) Real space imaging. **(b)** Back focal plane imaging.

Figure C.1. Confocal system for real space and back focal plane imaging.

There are two modes in the spectrometer. When light comes into the spectrometer through entrance slit, it's dispersed by a reflection grating. In the imaging mode, the direct reflection (0^{th} order) goes into the CCD camera. In the spectral mode, the light with first diffractive order is reflected to the CCD camera. Different wavelength components of the incoming light are dispersed at different angles by the grating equation

$$d(\sin\theta_m - \sin\theta_0) = m\lambda \tag{C.1}$$

where $m = 0, \pm 1, \ldots$ is the order of the diffraction and θ_m the diffraction angle. The horizontal axis of the CCD image becomes the wavelength axis. To get better spectral resolution, the input image on the entrance slit should be as narrow as possible.

C.2 Angle resolved transmission

In angle resolved transmission measurement, a collimated white light is illuminated on to the sample at an angle. The sample is placed on a rotation stage whose rotational center is aligned with the light path. This way, when sample is rotated, it will not move out of the scene.

Transmitted photons are collected by a long focal length objective and focused to a single spot at the back focal plane (because they are collimated), which is then imaged at the spectrometer's entrance slit. Then we use the spectral mode of the spectrometer to obtain the spectrum of this spot.

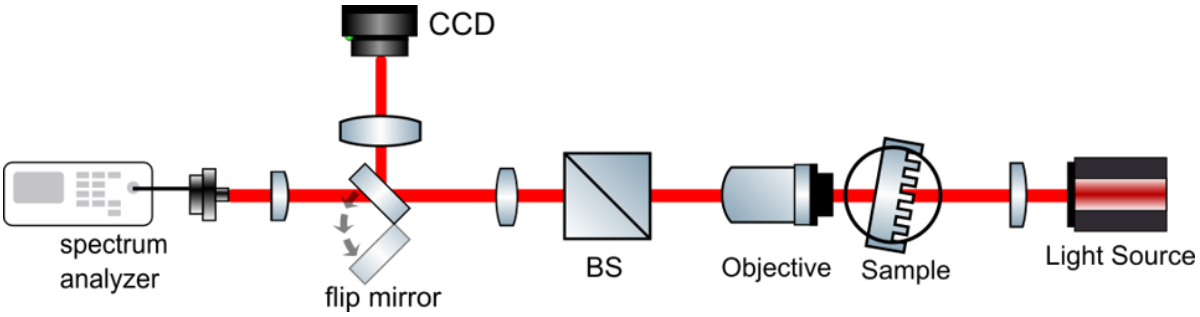

Figure C.2. Optical setup for angle resolved transmission measurement.

Bibliography

[1] Chawina De-Eknamkul, Jeonghoon Kim, **Wenzhuo Huang**, Yundong Ren, Madison Wilson, Francesca Puppo, Meena Patne, Alysson R. Muotri, Duygu Kuzum, and Ertugrul Cubukcu. Optical voltage sensing of electrophysiological signals with monolayer MoS_2. *In preparation*, 2022.

[2] **Wenzhuo Huang**, Chawina De-Eknamkul, and Ertugrul Cubukcu. Directing valley-polarized emission of 3L WS_2 by photonic crystal with directional circular dichroism. *In manuscript*, 2022.

[3] Chawina De-Eknamkul, **Wenzhuo Huang**, Xingwang Zhang, and Ertugrul Cubukcu. Directional propagation of self-resonant exciton-polariton in atomically thin WS_2 waveguide. *In manuscript*, 2022.

[4] **Wenzhuo Huang**, Chawina De-Eknamkul, and Ertugrul Cubukcu. Direct observation of polarization vortex on exceptional ring using WS_2 photoluminescence. *In manuscript*, 2022.

[5] Xingwang Zhang, **Wenzhuo Huang**, Chawina De-Eknamkul, Kedi Wu, Meng-qiang Zhao, Sefaattin Tongay, Alan T Charlie Johnson, and Ertugrul Cubukcu. Azimuthally polarized and unidirectional excitonic emission from deep subwavelength transition metal dichalcogenide annular heterostructures. *ACS Photonics*, 8(10):2861–2867, 2021.

[6] Xingwang Zhang, Xiaojie Zhang, **Wenzhuo Huang**, Kedi Wu, Mengqiang Zhao, AT Charlie Johnson, Sefaattin Tongay, and Ertugrul Cubukcu. Ultrathin WS_2-on-glass photonic crystal for self-resonant exciton-polaritonics. *Advanced Optical Materials*, 8(7):1901988, 2020.

[7] **Wenzhuo Huang**, Chawina De-Eknamkul, Xingwang Zhang, Eric Leewong, Meng-Qiang Zhao, AT Charlie Johnson, and Ertugrul Cubukcu. Monolayer excitonic emission for imaging spatial dispersion of photonic crystals. *ACS Photonics*, 6(9):2312–2319, 2019.

[8] Chawina De-Eknamkul, Xingwang Zhang, Meng-Qiang Zhao, **Wenzhuo Huang**, Renyu Liu, AT Charlie Johnson, and Ertugrul Cubukcu. MoS_2-enabled dual-mode

optoelectronic biosensor using a water soluble variant of μ-opioid receptor for opioid peptide detection. *2D Materials*, 7(1):014004, 2019.

[9] Xingwang Zhang, Nicolas Biekert, Shinhyuk Choi, Carl H Naylor, Chawina De-Eknamkul, **Wenzhuo Huang**, Xiaojie Zhang, Xiaorui Zheng, Dake Wang, AT Charlie Johnson, and Ertugrul Cubukcu. Dynamic photochemical and optoelectronic control of photonic Fano resonances via monolayer MoS_2 trions. *Nano Letters*, 18(2):957–963, 2018.

[10] Xingwang Zhang, Nicolas Biekert, Shinhyuk Choi, Carl H Naylor, Chawina De-Eknamkul, **Wenzhuo Huang**, Xiaorui Zheng, Dake Wang, AT Charlie Johnson, and Ertugrul Cubukcu. Coupling of photonic Fano resonances with MoS_2 excitons for enhanced light emission and optical modulation. In *2018 Conference on Lasers and Electro-Optics (CLEO)*, pages 1–2. IEEE, 2018.

[11] **Wenzhuo Huang**, Jing Yang, Xiao Xiao, and Jiasen Zhang. Surface plasmon polariton unidirectional nano-launcher based on the strong coupling effects in an asymmetric optical slot nanoantenna pair. *Plasmonics*, 10(6):1551–1556, 2015.

[12] Kostya S Novoselov, Andre K Geim, Sergei V Morozov, De-eng Jiang, Yanshui Zhang, Sergey V Dubonos, Irina V Grigorieva, and Alexandr A Firsov. Electric field effect in atomically thin carbon films. *Science*, 306(5696):666–669, 2004.

[13] Gordon W Semenoff. Condensed-matter simulation of a three-dimensional anomaly. *Physical Review Letters*, 53(26):2449, 1984.

[14] Jae Yoon Lee, Jun-Hwan Shin, Gwan-Hyoung Lee, and Chul-Ho Lee. Two-dimensional semiconductor optoelectronics based on van der waals heterostructures. *Nanomaterials*, 6(11):193, 2016.

[15] Tianshu Li and Giulia Galli. Electronic properties of MoS_2 nanoparticles. *The Journal of Physical Chemistry C*, 111(44):16192–16196, 2007.

[16] Kin Fai Mak, Changgu Lee, James Hone, Jie Shan, and Tony F Heinz. Atomically thin MoS_2: a new direct-gap semiconductor. *Physical Review Letters*, 105(13):136805, 2010.

[17] Andrea Splendiani, Liang Sun, Yuanbo Zhang, Tianshu Li, Jonghwan Kim, Chi-Yung Chim, Giulia Galli, and Feng Wang. Emerging photoluminescence in monolayer MoS_2. *Nano Letters*, 10(4):1271–1275, 2010.

[18] Gang Wang, Alexey Chernikov, Mikhail M Glazov, Tony F Heinz, Xavier Marie, Thierry Amand, and Bernhard Urbaszek. Colloquium: Excitons in atomically thin transition metal dichalcogenides. *Reviews of Modern Physics*, 90(2):021001, 2018.

[19] Jason S Ross, Philip Klement, Aaron M Jones, Nirmal J Ghimire, Jiaqiang Yan, DG Mandrus, Takashi Taniguchi, Kenji Watanabe, Kenji Kitamura, Wang Yao, David H. Cobden, and Xiaodong Xu. Electrically tunable excitonic light-emitting diodes based on monolayer WSe_2 p-n junctions. *Nature Nanotechnology*, 9(4):268–272, 2014.

[20] Zhipei Sun, Amos Martinez, and Feng Wang. Optical modulators with 2D layered materials. *Nature Photonics*, 10(4):227–238, 2016.

[21] Bowen Li, Shuai Zu, Jiadong Zhou, Qiao Jiang, Bowen Du, Hangyong Shan, Yang Luo, Zheng Liu, Xing Zhu, and Zheyu Fang. Single-nanoparticle plasmonic electro-optic modulator based on MoS_2 monolayers. *ACS Nano*, 11(10):9720–9727, 2017.

[22] Yueyang Chen, Shengnan Miao, Tianmeng Wang, Ding Zhong, Abhi Saxena, Colin Chow, James Whitehead, Dario Gerace, Xiaodong Xu, Su-Fei Shi, and Arka Majumdar. Metasurface integrated monolayer exciton polariton. *Nano Letters*, 20(7):5292–5300, 2020.

[23] Jorge Cuadra, Denis G Baranov, Martin Wersall, Ruggero Verre, Tomasz J Antosiewicz, and Timur Shegai. Observation of tunable charged exciton polaritons in hybrid monolayer WS_2-plasmonic nanoantenna system. *Nano Letters*, 18(3):1777–1785, 2018.

[24] Steven A Vitale, Daniel Nezich, Joseph O Varghese, Philip Kim, Nuh Gedik, Pablo Jarillo-Herrero, Di Xiao, and Mordechai Rothschild. Valleytronics: opportunities, challenges, and paths forward. *Small*, 14(38):1801483, 2018.

[25] Sina Najmaei, Adnen Mlayah, Arnaud Arbouet, Christian Girard, Jean Léotin, and Jun Lou. Plasmonic pumping of excitonic photoluminescence in hybrid MoS_2–Au nanostructures. *ACS Nano*, 8(12):12682–12689, 2014.

[26] Ying Yu, Ziheng Ji, Shuai Zu, Bowen Du, Yimin Kang, Ziwei Li, Zhangkai Zhou, Kebin Shi, and Zheyu Fang. Ultrafast plasmonic hot electron transfer in Au nanoantenna/MoS_2 heterostructures. *Advanced Functional Materials*, 26(35):6394–6401, 2016.

[27] Fei Yi, Mingliang Ren, Jason C Reed, Hai Zhu, Jiechang Hou, Carl H Naylor, AT Charlie Johnson, Ritesh Agarwal, and Ertugrul Cubukcu. Optomechanical enhancement of doubly resonant 2D optical nonlinearity. *Nano Letters*, 16(3):1631–1636, 2016.

[28] Gleb M Akselrod, Tian Ming, Christos Argyropoulos, Thang B Hoang, Yuxuan Lin, Xi Ling, David R Smith, Jing Kong, and Maiken H Mikkelsen. Leveraging nanocavity harmonics for control of optical processes in 2D semiconductors. *Nano Letters*, 15(5):3578–3584, 2015.

[29] Tobias Bucher, Aleksandr Vaskin, Rajeshkumar Mupparapu, Franz JF L ochner, Antony

George, Katie E Chong, Stefan Fasold, Christof Neumann, Duk-Yong Choi, Falk Eilenberger, Frank Setzpfandt, Yuri S. Kivshar, Thomas Pertsch, Andrey Turchanin, and Isabelle Staude. Tailoring photoluminescence from MoS_2 monolayers by mie-resonant metasurfaces. *ACS Photonics*, 6(4):1002–1009, 2019.

[30] Ahmet Fatih Cihan, Alberto G Curto, Søren Raza, Pieter G Kik, and Mark L Brongersma. Silicon mie resonators for highly directional light emission from monolayer MoS_2. *Nature Photonics*, 12(5):284–290, 2018.

[31] SRK Chaitanya Indukuri, Christian Frydendahl, Jonathan Bar-David, Noa Mazurski, and Uriel Levy. WS_2 monolayers coupled to hyperbolic metamaterial nanoantennas: broad implications for light–matter-interaction applications. *ACS Applied Nano Materials*, 3(10):10226–10233, 2020.

[32] Florian Spreyer, Ruizhe Zhao, Lingling Huang, and Thomas Zentgraf. Second harmonic imaging of plasmonic pancharatnam-berry phase metasurfaces coupled to monolayers of WS_2. *Nanophotonics*, 9(2):351–360, 2020.

[33] Guangwei Hu, Xuanmiao Hong, Kai Wang, Jing Wu, He-Xiu Xu, Wenchao Zhao, Weiwei Liu, Shuang Zhang, Francisco Garcia-Vidal, Bing Wang, Peixiang Lu, and Cheng-Wei Qiu. Coherent steering of nonlinear chiral valley photons with a synthetic Au–WS_2 metasurface. *Nature Photonics*, 13(7):467–472, 2019.

[34] Chunrui Han and Jianting Ye. Polarized resonant emission of monolayer WS_2 coupled with plasmonic sawtooth nanoslit array. *Nature Communications*, 11(1):1–9, 2020.

[35] Yasir J Noori, Yameng Cao, Jonathan Roberts, Christopher Woodhead, Ramon Bernardo-Gavito, Peter Tovee, and Robert J Young. Photonic crystals for enhanced light extraction from 2D materials. *Acs Photonics*, 3(12):2515–2520, 2016.

[36] Xiaochen Ge, Momchil Minkov, Shanhui Fan, Xiuling Li, and Weidong Zhou. Laterally confined photonic crystal surface emitting laser incorporating monolayer tungsten disulfide. *npj 2D Materials and Applications*, 3(1):1–5, 2019.

[37] J. Wang, H. Li, Y. Ma, M. Zhao, W. Liu, B. Wang, S. Wu, X. Liu, L. Shi, T. Jiang, and J. Zi. Routing valley exciton emission of a WS_2 monolayer via delocalized bloch modes of in-plane inversion-symmetry-broken photonic crystal slabs. *Light Sci Appl*, 9:148, 2020.

[38] Byunghoon Ryu, Hongsuk Nam, Bo-Ram Oh, Yujing Song, Pengyu Chen, Younggeun Park, Wenjie Wan, Katsuo Kurabayashi, and Xiaogan Liang. Cyclewise operation of printed MoS_2 transistor biosensors for rapid biomolecule quantification at femtomolar levels. *ACS Sensors*, 2(2):274–281, 2017.

[39] Kyung Yong Ko, Jeong-Gyu Song, Youngjun Kim, Taejin Choi, Sera Shin, Chang Wan Lee, Kyounghoon Lee, Jahyun Koo, Hoonkyung Lee, Jongbaeg Kim, Taeyoon Lee, Jusang Park, and Hyungjun Kim. Improvement of gas-sensing performance of large-area tungsten disulfide nanosheets by surface functionalization. *ACS Nano*, 10(10):9287–9296, 2016.

[40] Jaeseo Park, Jihun Mun, Jae-Soo Shin, and Sang-Woo Kang. Highly sensitive two-dimensional MoS_2 gas sensor decorated with pt nanoparticles. *Royal Society Open Science*, 5(12):181462, 2018.

[41] Oriol Lopez-Sanchez, Dominik Lembke, Metin Kayci, Aleksandra Radenovic, and Andras Kis. Ultrasensitive photodetectors based on monolayer mos 2. *Nature Nanotechnology*, 8(7):497–501, 2013.

[42] Dong-Ho Kang, Myung-Soo Kim, Jaewoo Shim, Jeaho Jeon, Hyung-Youl Park, Woo-Shik Jung, Hyun-Yong Yu, Chang-Hyun Pang, Sungjoo Lee, and Jin-Hong Park. High-performance transition metal dichalcogenide photodetectors enhanced by self-assembled monolayer doping. *Advanced Functional Materials*, 25(27):4219–4227, 2015.

[43] Weihuang Yang, Jingzhi Shang, Jianpu Wang, Xiaonan Shen, Bingchen Cao, Namphung Peimyoo, Chenji Zou, Yu Chen, Yanlong Wang, Chunxiao Cong, Wei Huang, and Ting Yu. Electrically tunable valley-light emitting diode (vled) based on cvd-grown monolayer WS_2. *Nano Letters*, 16(3):1560–1567, 2016.

[44] Chang-Hua Liu, Genevieve Clark, Taylor Fryett, Sanfeng Wu, Jiajiu Zheng, Fariba Hatami, Xiaodong Xu, and Arka Majumdar. Nanocavity integrated van der waals heterostructure light-emitting tunneling diode. *Nano Letters*, 17(1):200–205, 2017.

[45] Omid Salehzadeh, Mehrdad Djavid, Nhung Hong Tran, Ishiang Shih, and Zetian Mi. Optically pumped two-dimensional MoS_2 lasers operating at room-temperature. *Nano Letters*, 15(8):5302–5306, 2015.

[46] Sanfeng Wu, Sonia Buckley, John R Schaibley, Liefeng Feng, Jiaqiang Yan, David G Mandrus, Fariba Hatami, Wang Yao, Jelena Vučković, Arka Majumdar, and Xiaodong Xu. Monolayer semiconductor nanocavity lasers with ultralow thresholds. *Nature*, 520(7545):69–72, 2015.

[47] Lewis Reeves, Yue Wang, and Thomas F Krauss. 2D material microcavity light emitters: to lase or not to lase? *Advanced Optical Materials*, 6(19):1800272, 2018.

[48] Eunice Y Paik, Long Zhang, G William Burg, Rahul Gogna, Emanuel Tutuc, and Hui Deng. Interlayer exciton laser of extended spatial coherence in atomically thin heterostructures. *Nature*, 576(7785):80–84, 2019.

[49] Thibault Chervy, Stefano Azzini, Etienne Lorchat, Shaojun Wang, Yuri Gorodetski, James A. Hutchison, Stéphane Berciaud, Thomas W. Ebbesen, and Cyriaque Genet. Room temperature chiral coupling of valley excitons with spin-momentum locked surface plasmons. *ACS Photonics*, 5(4):1281–1287, 2018.

[50] Z. Li, C. Liu, X. Rong, Y. Luo, H. Cheng, L. Zheng, F. Lin, B. Shen, Y. Gong, S. Zhang, and Z. Fang. Tailoring MoS_2 valley-polarized photoluminescence with super chiral near-field. *Adv Mater*, page e1801908, 2018.

[51] S. Guddala, R. Bushati, M. Li, A. B. Khanikaev, and V. M. Menon. Valley selective optical control of excitons in 2D semiconductors using a chiral metasurface [invited]. *Optical Materials Express*, 9(2):536–543, 2019.

[52] Lucas C Flatten, Zhengyu He, David M Coles, Aurelien AP Trichet, Alex W Powell, Robert A Taylor, Jamie H Warner, and Jason M Smith. Room-temperature exciton-polaritons with two-dimensional WS_2. *Scientific Reports*, 6(1):1–7, 2016.

[53] Simone Latini, Enrico Ronca, Umberto De Giovannini, Hannes H ubener, and Angel Rubio. Cavity control of excitons in two-dimensional materials. *Nano Letters*, 19(6):3473–3479, 2019.

[54] Tim Byrnes, Na Young Kim, and Yoshihisa Yamamoto. Exciton–polariton condensates. *Nature Physics*, 10(11):803–813, 2014.

[55] Alberto Amo, Jérôme Lefrère, Simon Pigeon, Claire Adrados, Cristiano Ciuti, Iacopo Carusotto, Romuald Houdré, Elisabeth Giacobino, and Alberto Bramati. Superfluidity of polaritons in semiconductor microcavities. *Nature Physics*, 5(11):805–810, 2009.

[56] Alexander B Khanikaev, S Hossein Mousavi, Wang-Kong Tse, Mehdi Kargarian, Allan H MacDonald, and Gennady Shvets. Photonic topological insulators. *Nature Materials*, 12(3):233–239, 2013.

[57] Yuhao Kang, Xiang Ni, Xiaojun Cheng, Alexander B Khanikaev, and Azriel Z Genack. Pseudo-spin–valley coupled edge states in a photonic topological insulator. *Nature Communications*, 9(1):1–7, 2018.

[58] Yihao Yang, Zhen Gao, Haoran Xue, Li Zhang, Mengjia He, Zhaoju Yang, Ranjan Singh, Yidong Chong, Baile Zhang, and Hongsheng Chen. Realization of a three-dimensional photonic topological insulator. *Nature*, 565(7741):622–626, 2019.

[59] Biye Xie, Guangxu Su, Hong-Fei Wang, Feng Liu, Lumang Hu, Si-Yuan Yu, Peng Zhan, Ming-Hui Lu, Zhenlin Wang, and Yan-Feng Chen. Higher-order quantum spin hall effect in a photonic crystal. *Nature Communications*, 11(1):1–8, 2020.

[60] CE Whittaker, T Dowling, AV Nalitov, AV Yulin, B Royall, E Clarke, MS Skolnick, IA Shelykh, and DN Krizhanovskii. Optical analogue of dresselhaus spin–orbit interaction in photonic graphene. *Nature Photonics*, 15(3):193–196, 2021.

[61] Jian-Wen Dong, Xiao-Dong Chen, Hanyu Zhu, Yuan Wang, and Xiang Zhang. Valley photonic crystals for control of spin and topology. *Nature Materials*, 16(3):298–302, 2017.

[62] Yuting Yang, Hua Jiang, and Zhi Hong Hang. Topological valley transport in two-dimensional honeycomb photonic crystals. *Scientific Reports*, 8(1):1–7, 2018.

[63] Hironobu Yoshimi, Takuto Yamaguchi, Yasutomo Ota, Yasuhiko Arakawa, and Satoshi Iwamoto. Slow light waveguides in topological valley photonic crystals. *Optics Letters*, 45(9):2648–2651, 2020.

[64] Haoran Xue, Yihao Yang, and Baile Zhang. Topological valley photonics: Physics and device applications. *Advanced Photonics Research*, 2(8):2100013, 2021.

[65] Bo Zhen, Chia Wei Hsu, Yuichi Igarashi, Ling Lu, Ido Kaminer, Adi Pick, Song-Liang Chua, John D Joannopoulos, and Marin Soljačić. Spawning rings of exceptional points out of dirac cones. *Nature*, 525(7569):354–358, 2015.

[66] Hengyun Zhou, Chao Peng, Yoseob Yoon, Chia Wei Hsu, Keith A Nelson, Liang Fu, John D Joannopoulos, Marin Soljačić, and Bo Zhen. Observation of bulk fermi arc and polarization half charge from paired exceptional points. *Science*, 359(6379):1009–1012, 2018.

[67] Ramy El-Ganainy, Konstantinos G Makris, Mercedeh Khajavikhan, Ziad H Musslimani, Stefan Rotter, and Demetrios N Christodoulides. Non-hermitian physics and pt symmetry. *Nature Physics*, 14(1):11–19, 2018.

[68] Chia Wei Hsu, Bo Zhen, Jeongwon Lee, Song-Liang Chua, Steven G Johnson, John D Joannopoulos, and Marin Soljačić. Observation of trapped light within the radiation continuum. *Nature*, 499(7457):188–191, 2013.

[69] Bo Wang, Wenzhe Liu, Maoxiong Zhao, Jiajun Wang, Yiwen Zhang, Ang Chen, Fang Guan, Xiaohan Liu, Lei Shi, and Jian Zi. Generating optical vortex beams by momentum-space polarization vortices centred at bound states in the continuum. *Nature Photonics*, 14(10):623–628, 2020.

[70] Xingwang Zhang, Shinhyuk Choi, Dake Wang, Carl H Naylor, AT Charlie Johnson, and Ertugrul Cubukcu. Unidirectional doubly enhanced MoS_2 emission via photonic fano resonances. *Nano Letters*, 17(11):6715–6720, 2017.

[71] Wenzhe Liu, Bo Wang, Yiwen Zhang, Jiajun Wang, Maoxiong Zhao, Fang Guan, Xiaohan Liu, Lei Shi, and Jian Zi. Circularly polarized states spawning from bound states in the continuum. *Physical Review Letters*, 123(11):116104, 2019.

[72] Ruggero Verre, Denis G Baranov, Battulga Munkhbat, Jorge Cuadra, Mikael Käll, and Timur Shegai. Transition metal dichalcogenide nanodisks as high-index dielectric mie nanoresonators. *Nature Nanotechnology*, 14(7):679–683, 2019.

[73] J. A. Wilson and A. D. Yoffe. The transition metal dichalcogenides discussion and interpretation of the observed optical, electrical and structural properties. *Advances in Physics*, 18(73):193–335, 1969.

[74] Xingwang Zhang, Chawina De-Eknamkul, Jie Gu, Alexandra L Boehmke, Vinod M Menon, Jacob Khurgin, and Ertugrul Cubukcu. Guiding of visible photons at the ångström thickness limit. *Nature Nanotechnology*, 14(9):844–850, 2019.

[75] Weijie Zhao, Zohreh Ghorannevis, Leiqiang Chu, Minglin Toh, Christian Kloc, Ping-Heng Tan, and Goki Eda. Evolution of electronic structure in atomically thin sheets of WS_2 and WSe_2. *ACS Nano*, 7(1):791–797, 2013.

[76] YC Cheng, ZY Zhu, Muhammad Tahir, and Udo Schwingenschlögl. Spin-orbit–induced spin splittings in polar transition metal dichalcogenide monolayers. *EPL (Europhysics Letters)*, 102(5):57001, 2013.

[77] Gui-Bin Liu, Wen-Yu Shan, Yugui Yao, Wang Yao, and Di Xiao. Three-band tight-binding model for monolayers of group-vib transition metal dichalcogenides. *Physical Review B*, 88(8):085433, 2013.

[78] Jun Xiao, Mervin Zhao, Yuan Wang, and Xiang Zhang. Excitons in atomically thin 2D semiconductors and their applications. *Nanophotonics*, 6(6):1309–1328, 2017.

[79] Ting Cao, Gang Wang, Wenpeng Han, Huiqi Ye, Chuanrui Zhu, Junren Shi, Qian Niu, Pingheng Tan, Enge Wang, Baoli Liu, and Ji Feng. Valley-selective circular dichroism of monolayer molybdenum disulphide. *Nature Communications*, 3(1):1–5, 2012.

[80] Xiaoze Liu, Wei Bao, Quanwei Li, Chad Ropp, Yuan Wang, and Xiang Zhang. Control of coherently coupled exciton polaritons in monolayer tungsten disulphide. *Physical Review Letters*, 119(2):027403, 2017.

[81] John D. Joannopoulos, Steven G. Johnson, Joshua N. Winn, and Robert D. Meade. *Photonic Crystals: Molding the Flow of Light (Second Edition)*. Princeton University Press, second edition, 2008.

[82] Jian-Ming Jin. *The finite element method in electromagnetics*. John Wiley & Sons, 2015.

[83] D. M. Sullivan. *Electromagnetic simulation using the FDTD method*. IEEE Press, 2000.

[84] Allen Taflove, Susan C Hagness, and Melinda Piket-May. Computational electromagnetics: the finite-difference time-domain method. *The Electrical Engineering Handbook*, 3, 2005.

[85] Zhi-Yuan Li and Lan-Lan Lin. Photonic band structures solved by a plane-wave-based transfer-matrix method. *Physical Review E*, 67(4):046607, 2003.

[86] MG Moharam and TK Gaylord. Rigorous coupled-wave analysis of planar-grating diffraction. *JOSA*, 71(7):811–818, 1981.

[87] MG Moharam, Eric B Grann, Drew A Pommet, and TK Gaylord. Formulation for stable and efficient implementation of the rigorous coupled-wave analysis of binary gratings. *JOSA a*, 12(5):1068–1076, 1995.

[88] Kane Yee. Numerical solution of initial boundary value problems involving maxwell's equations in isotropic media. *IEEE Transactions on antennas and propagation*, 14(3):302–307, 1966.

[89] MEEP Developers. Yee lattice.

[90] Victor Liu and Shanhui Fan. S4: A free electromagnetic solver for layered periodic structures. *Computer Physics Communications*, 183(10):2233–2244, 2012.

[91] Philipp Tonndorf, Robert Schmidt, Robert Schneider, Johannes Kern, Michele Buscema, Gary A Steele, Andres Castellanos-Gomez, Herre SJ van der Zant, Steffen Michaelis de Vasconcellos, and Rudolf Bratschitsch. Single-photon emission from localized excitons in an atomically thin semiconductor. *Optica*, 2(4):347–352, 2015.

[92] Yanxia Ye, Xiuming Dou, Kun Ding, Yu Chen, Desheng Jiang, Fuhua Yang, and Baoquan Sun. Single photon emission from deep-level defects in monolayer WSe_2. *Physical Review B*, 95(24):245313, 2017.

[93] Britton WH Baugher, Hugh OH Churchill, Yafang Yang, and Pablo Jarillo-Herrero. Optoelectronic devices based on electrically tunable p-n diodes in a monolayer dichalcogenide. *Nature Nanotechnology*, 9(4):262–267, 2014.

[94] Yu Ye, Zi Jing Wong, Xiufang Lu, Xingjie Ni, Hanyu Zhu, Xianhui Chen, Yuan Wang, and Xiang Zhang. Monolayer excitonic laser. *Nature Photonics*, 9(11):733–737, 2015.

[95] Bo Zhen, Song-Liang Chua, Jeongwon Lee, Alejandro W Rodriguez, Xiangdong Liang, Steven G Johnson, John D Joannopoulos, Marin Soljačić, and Ofer Shapira. Enabling enhanced emission and low-threshold lasing of organic molecules using special Fano resonances of macroscopic photonic crystals. *Proceedings of the National Academy of Sciences*, 110(34):13711–13716, 2013.

[96] Sanfeng Wu, Sonia Buckley, Aaron M Jones, Jason S Ross, Nirmal J Ghimire, Jiaqiang Yan, David G Mandrus, Wang Yao, Fariba Hatami, Jelena Vučković, Arka Majumdar, and Xiaodong Xu. Control of two-dimensional excitonic light emission via photonic crystal. *2D Materials*, 1(1):011001, 2014.

[97] Serkan Butun, Sefaattin Tongay, and Koray Aydin. Enhanced light emission from large-area monolayer MoS_2 using plasmonic nanodisc arrays. *Nano Letters*, 15(4):2700–2704, 2015.

[98] Bumsu Lee, Joohee Park, Gang Hee Han, Ho-Seok Ee, Carl H Naylor, Wenjing Liu, AT Charlie Johnson, and Ritesh Agarwal. Fano resonance and spectrally modified photoluminescence enhancement in monolayer MoS_2 integrated with plasmonic nanoantenna array. *Nano Letters*, 15(5):3646–3653, 2015.

[99] Zhuo Wang, Zhaogang Dong, Yinghong Gu, Yung-Huang Chang, Lei Zhang, Lain-Jong Li, Weijie Zhao, Goki Eda, Wenjing Zhang, Gustavo Grinblat, Stefan A. Maier, Joel K. W. Yang, Cheng-Wei Qiu, and Andrew T. S. Wee. Giant photoluminescence enhancement in tungsten-diselenide–gold plasmonic hybrid structures. *Nature Communications*, 7(1):1–8, 2016.

[100] Haitao Chen, Stefan Nanz, Aimi Abass, Jingshi Yan, Tingge Gao, Duk-Yong Choi, Yuri S Kivshar, Carsten Rockstuhl, and Dragomir N Neshev. Enhanced directional emission from monolayer WSe_2 integrated onto a multiresonant silicon-based photonic structure. *ACS Photonics*, 4(12):3031–3038, 2017.

[101] B. Mukherjee, N. Kaushik, Ravi P. N. Tripathi, A. M. Joseph, P. K. Mohapatra, S. Dhar, B. P. Singh, G. V. Kumar, E. Simsek, and S. Lodha. Exciton emission intensity modulation of monolayer MoS_2 via Au plasmon coupling. *Scientific Reports*, 7(1):1–11, 2017.

[102] Taylor K Fryett, Yueyang Chen, James Whitehead, Zane Matthew Peycke, Xiaodong Xu, and Arka Majumdar. Encapsulated silicon nitride nanobeam cavity for hybrid nanophotonics. *ACS Photonics*, 5(6):2176–2181, 2018.

[103] Jonathan J Wierer, Aurelien David, and Mischa M Megens. Iii-nitride photonic-crystal light-emitting diodes with high extraction efficiency. *Nature Photonics*, 3(3):163–169, 2009.

[104] Shuai Yuan, Xingzhi Qiu, Chengcong Cui, Liangqiu Zhu, Yuxi Wang, Yi Li, Jinwen Song, Qingzhong Huang, and Jinsong Xia. Strong photoluminescence enhancement in all-dielectric fano metasurface with high quality factor. *ACS Nano*, 11(11):10704–10711, 2017.

[105] Niccoló Michieli, Boris Kalinic, Carlo Scian, Tiziana Cesca, and Giovanni Mattei. Emission rate modification and quantum efficiency enhancement of Er^{3+} emitters by near-field coupling with nanohole arrays. *ACS Photonics*, 5(6):2189–2199, 2018.

[106] Shanhui Fan and John D Joannopoulos. Analysis of guided resonances in photonic crystal slabs. *Physical Review B*, 65(23):235112, 2002.

[107] Yifei Yu, Yiling Yu, Chao Xu, Yong-Qing Cai, Liqin Su, Yong Zhang, Yong-Wei Zhang, Kenan Gundogdu, and Linyou Cao. Engineering substrate interactions for high luminescence efficiency of transition-metal dichalcogenide monolayers. *Advanced Functional Materials*, 26(26):4733–4739, 2016.

[108] CH Lui, AJ Frenzel, DV Pilon, Y-H Lee, X Ling, GM Akselrod, J Kong, and N Gedik. Trion-induced negative photoconductivity in monolayer mos_2. *Physical Review Letters*, 113(16):166801, 2014.

[109] Kin Fai Mak, Keliang He, Changgu Lee, Gwan Hyoung Lee, James Hone, Tony F Heinz, and Jie Shan. Tightly bound trions in monolayer MoS_2. *Nature Materials*, 12(3):207–211, 2013.

[110] Steven G Johnson and John D Joannopoulos. Block-iterative frequency-domain methods for maxwell's equations in a planewave basis. *Optics Express*, 8(3):173–190, 2001.

[111] Kyoung-Duck Park, Omar Khatib, Vasily Kravtsov, Genevieve Clark, Xiaodong Xu, and Markus B Raschke. Hybrid tip-enhanced nanospectroscopy and nanoimaging of monolayer WSe_2 with local strain control. *Nano Letters*, 16(4):2621–2627, 2016.

[112] Long Zhang, Rahul Gogna, Will Burg, Emanuel Tutuc, and Hui Deng. Photonic-crystal exciton-polaritons in monolayer semiconductors. *Nature Communications*, 9(1):1–8, 2018.

[113] Taylor K Fryett, Kyle L Seyler, Jiajiu Zheng, Chang-Hua Liu, Xiaodong Xu, and Arka Majumdar. Silicon photonic crystal cavity enhanced second-harmonic generation from monolayer WSe_2. *2D Materials*, 4(1):015031, 2016.

[114] Zhili Yang, Shahriar Aghaeimeibodi, and Edo Waks. Chiral light-matter interactions using spin-valley states in transition metal dichalcogenides. *Optics Express*, 27(15):21367–21379, 2019.

[115] Babak Bahari, Felipe Vallini, Thomas Lepetit, Ricardo Tellez-Limon, JH Park, Ashok Kodigala, Yeshaiahu Fainman, and Boubacar Kante. Integrated and steerable vortex lasers using bound states in continuum. *arXiv preprint. arXiv:1707.00181*, 2017.

[116] Marat Soskin, Svetlana V Boriskina, Yidong Chong, Mark R Dennis, and Anton Desyatnikov. Singular optics and topological photonics. *Journal of Optics*, 19(1):010401, 2016.

[117] Hugo M Doeleman, Francesco Monticone, Wouter den Hollander, Andrea Alù, and A Femius Koenderink. Experimental observation of a polarization vortex at an optical bound state in the continuum. *Nature Photonics*, 12(7):397–401, 2018.

[118] Yiwen Zhang, Ang Chen, Wenzhe Liu, Chia Wei Hsu, Bo Wang, Fang Guan, Xiaohan Liu, Lei Shi, Ling Lu, and Jian Zi. Observation of polarization vortices in momentum space. *Physical Review Letters*, 120(18):186103, 2018.

[119] Can Huang, Chen Zhang, Shumin Xiao, Yuhan Wang, Yubin Fan, Yilin Liu, Nan Zhang, Geyang Qu, Hongjun Ji, Jiecai Han, Li Ge, Yuri Kivshar, and Qinghai Song. Ultrafast control of vortex microlasers. *Science*, 367(6481):1018–1021, 2020.

[120] Han Zhao, Xingdu Qiao, Tianwei Wu, Bikashkali Midya, Stefano Longhi, and Liang Feng. Non-hermitian topological light steering. *Science*, 365(6458):1163–1166, 2019.

[121] Yi Yang, Chao Peng, Yong Liang, Zhengbin Li, and Susumu Noda. Analytical perspective for bound states in the continuum in photonic crystal slabs. *Physical Review Letters*, 113(3):037401, 2014.

[122] Bo Zhen, Chia Wei Hsu, Ling Lu, A Douglas Stone, and Marin Soljačić. Topological nature of optical bound states in the continuum. *Physical Review Letters*, 113(25):257401, 2014.

[123] Diego R Abujetas and José A Sánchez-Gil. Near-field excitation of bound states in the continuum in all-dielectric metasurfaces through a coupled electric/magnetic dipole model. *Nanomaterials*, 11(4):998, 2021.

[124] Liang Feng, Ramy El-Ganainy, and Li Ge. Non-hermitian photonics based on parity–time symmetry. *Nature Photonics*, 11(12):752–762, 2017.

[125] Mikhail F Limonov, Mikhail V Rybin, Alexander N Poddubny, and Yuri S Kivshar. Fano resonances in photonics. *Nature Photonics*, 11(9):543–554, 2017.

[126] Adi Pick, Bo Zhen, Owen D Miller, Chia W Hsu, Felipe Hernandez, Alejandro W Rodriguez, Marin Soljačić, and Steven G Johnson. General theory of spontaneous

emission near exceptional points. *Optics Express*, 25(11):12325–12348, 2017.

[127] Leran Lu, Quynh Le-Van, Lydie Ferrier, Emmanuel Drouard, Christian Seassal, and Hai Son Nguyen. Engineering a light–matter strong coupling regime in perovskite-based plasmonic metasurface: quasi-bound state in the continuum and exceptional points. *Photonics Research*, 8(12):A91–A100, 2020.

[128] Bikashkali Midya, Han Zhao, and Liang Feng. Non-hermitian photonics promises exceptional topology of light. *Nature Communications*, 9(1):1–4, 2018.

[129] AI Magunov, I Rotter, and SI Strakhova. Fano resonances in the overlapping regime. *Physical Review B*, 68(24):245305, 2003.

[130] R. Suzuki, M. Sakano, Y. J. Zhang, R. Akashi, D. Morikawa, A. Harasawa, K. Yaji, K. Kuroda, K. Miyamoto, T. Okuda, K. Ishizaka, R. Arita, and Y. Iwasa. Valley-dependent spin polarization in bulk MoS_2 with broken inversion symmetry. *Nat Nanotechnol*, 9(8):611–7, 2014.

[131] W. Zhao, R. M. Ribeiro, M. Toh, A. Carvalho, C. Kloc, A. H. Castro Neto, and G. Eda. Origin of indirect optical transitions in few-layer MoS_2, WS_2, and WSe_2. *Nano Lett*, 13(11):5627–34, 2013.

[132] H. Zeng, G. B. Liu, J. Dai, Y. Yan, B. Zhu, R. He, L. Xie, S. Xu, X. Chen, W. Yao, and X. Cui. Optical signature of symmetry variations and spin-valley coupling in atomically thin tungsten dichalcogenides. *Sci Rep*, 3:1608, 2013.

[133] Xiaodong Xu, Wang Yao, Di Xiao, and Tony F. Heinz. Spin and pseudospins in layered transition metal dichalcogenides. *Nature Physics*, 10(5):343–350, 2014.

[134] B. Zhu, H. Zeng, J. Dai, Z. Gong, and X. Cui. Anomalously robust valley polarization and valley coherence in bilayer WS_2. *Proc Natl Acad Sci U S A*, 111(32):11606–11, 2014.

[135] K. F. Mak, K. He, J. Shan, and T. F. Heinz. Control of valley polarization in monolayer MoS_2 by optical helicity. *Nat Nanotechnol*, 7(8):494–8, 2012.

[136] H. Zeng, J. Dai, W. Yao, D. Xiao, and X. Cui. Valley polarization in MoS_2 monolayers by optical pumping. *Nat Nanotechnol*, 7(8):490–3, 2012.

[137] A. M. Jones, H. Yu, N. J. Ghimire, S. Wu, G. Aivazian, J. S. Ross, B. Zhao, J. Yan, D. G. Mandrus, D. Xiao, W. Yao, and X. Xu. Optical generation of excitonic valley coherence in monolayer WSe_2. *Nat Nanotechnol*, 8(9):634–8, 2013.

[138] Ziliang Ye, Dezheng Sun, and Tony F. Heinz. Optical manipulation of valley pseudospin. *Nature Physics*, 13(1):26–29, 2016.

[139] Yen-Jung Chen, Jeffrey D. Cain, Teodor K. Stanev, Vinayak P. Dravid, and Nathaniel P. Stern. Valley-polarized exciton–polaritons in a monolayer semiconductor. *Nature Photonics*, 11(7):431–435, 2017.

[140] S. Dufferwiel, T. P. Lyons, D. D. Solnyshkov, A. A. P. Trichet, A. Catanzaro, F. Withers, Guillaume Malpuech, J. M. Smith, K. S. Novoselov, M. S. Skolnick, D. N. Krizhanovskii, and A. I. Tartakovskii. Valley coherent exciton-polaritons in a monolayer semiconductor. *Nature Communications*, 9(1):1–7, 2018.

[141] T. Mueller and E. Malic. Exciton physics and device application of two-dimensional transition metal dichalcogenide semiconductors. *Npj 2d Materials and Applications*, 2(1), 2018.

[142] Y. P. Liu, Y. J. Gao, S. Y. Zhang, J. He, J. Yu, and Z. W. Liu. Valleytronics in transition metal dichalcogenides materials. *Nano Research*, 12(11):2695–2711, 2019.

[143] Y. J. Zhang, T. Oka, R. Suzuki, J. T. Ye, and Y. Iwasa. Electrically switchable chiral light-emitting transistor. *Science*, 344(6185):725–8, 2014.

[144] Chitraleema Chakraborty, Arunabh Mukherjee, Liangyu Qiu, and A. Nick Vamivakas. Electrically tunable valley polarization and valley coherence in monolayer wse 2 embedded in a van der waals heterostructure. *Optical Materials Express*, 9(3), 2019.

[145] C. Rupprecht, E. Sedov, M. Klaas, H. Knopf, M. Blei, N. Lundt, S. Tongay, T. Taniguchi, K. Watanabe, U. Schulz, A. Kavokin, F. Eilenberger, S. Hofling, and C. Schneider. Manipulation of room-temperature valley-coherent exciton-polaritons in atomically thin crystals by real and artificial magnetic fields. *2d Materials*, 7(3), 2020.

[146] C. R. Zhu, G. Wang, B. L. Liu, X. Marie, X. F. Qiao, X. Zhang, X. X. Wu, H. Fan, P. H. Tan, T. Amand, and B. Urbaszek. Strain tuning of optical emission energy and polarization in monolayer and bilayer MoS_2. *Physical Review B*, 88(12), 2013.

[147] S. L. Li, K. Tsukagoshi, E. Orgiu, and P. Samori. Charge transport and mobility engineering in two-dimensional transition metal chalcogenide semiconductors. *Chem Soc Rev*, 45(1):118–51, 2016.

[148] L. Yuan and L. Huang. Exciton dynamics and annihilation in WS_2 2D semiconductors. *Nanoscale*, 7(16):7402–8, 2015.

[149] Alexander Krasnok and Andrea Alù. Valley-selective response of nanostructures coupled

to 2D transition-metal dichalcogenides. *Applied Sciences*, 8(7), 2018.

[150] R. M. Peng, C. M. Wu, H. Li, X. D. Xu, and M. Li. Separation of the valley exciton-polariton in two-dimensional semiconductors with an anisotropic photonic crystal. *Physical Review B*, 101(24), 2020.

[151] S. Li, H. Wang, J. Wang, H. Chen, and L. Shao. Control of light-valley interactions in 2D transition metal dichalcogenides with nanophotonic structures. *Nanoscale*, 13(13):6357–6372, 2021.

[152] Su-Hyun Gong, Filippo Alpeggiani, Beniamino Sciacca, Erik C Garnett, and L Kuipers. Nanoscale chiral valley-photon interface through optical spin-orbit coupling. *Science*, 359(6374):443–447, 2018.

[153] P. G. Chen, Z. Li, Y. Qi, T. W. Lo, S. Wang, W. Jin, K. Y. Wong, S. Fan, A. V. Zayats, and D. Lei. Long-range directional routing and spatial selection of high-spin-purity valley trion emission in monolayer WS_2. *ACS Nano*, 2021.

[154] L. Y. Sun, C. Y. Wang, A. Krasnok, J. Choi, J. W. Shi, J. S. Gomez-Diaz, A. Zepeda, S. Gwo, C. K. Shih, A. Alu, and X. Q. Li. Separation of valley excitons in a MoS_2 monolayer using a subwavelength asymmetric groove array. *Nature Photonics*, 13(3):180–+, 2019.

[155] W. Liu, Z. Ji, Y. Wang, G. Modi, M. Hwang, B. Zheng, V. J. Sorger, A. Pan, and R. Agarwal. Generation of helical topological exciton-polaritons. *Science*, 370(6516):600–604, 2020.

[156] H. Chen, M. Liu, L. Xu, and D. N. Neshev. Valley-selective directional emission from a transition-metal dichalcogenide monolayer mediated by a plasmonic nanoantenna. *Beilstein J Nanotechnol*, 9:780–788, 2018.

[157] H. T. Lin, C. Y. Chang, P. J. Cheng, M. Y. Li, C. C. Cheng, S. W. Chang, L. L. J. Li, C. W. Chu, P. K. Wei, and M. H. Shih. Circular dichroism control of tungsten diselenide (WSe_2) atomic layers with plasmonic metamolecules. *ACS Appl Mater Interfaces*, 10(18):15996–16004, 2018.

[158] Chia Wei Hsu, Bo Zhen, Marin Soljačić, and A Douglas Stone. Polarization state of radiation from a photonic crystal slab. *arXiv preprint. arXiv:1708.02197*, 2017.

[159] S. V. Lobanov, S. G. Tikhodeev, N. A. Gippius, A. A. Maksimov, E. V. Filatov, I. I. Tartakovskii, V. D. Kulakovskii, T. Weiss, C. Schneider, J. Geßler, M. Kamp, and S. H ofling. Controlling circular polarization of light emitted by quantum dots using chiral photonic crystal slabs. *Physical Review B*, 92(20), 2015.

[160] S. Fan, W. Suh, and J. D. Joannopoulos. Temporal coupled-mode theory for the fano resonance in optical resonators. *J Opt Soc Am A Opt Image Sci Vis*, 20(3):569–72, 2003.

[161] Ayse Berkdemir, Humberto R. Gutiérrez, Andrés R. Botello-Méndez, Néstor Perea-López, Ana Laura Elías, Chen-Ing Chia, Bei Wang, Vincent H. Crespi, Florentino López-Urías, Jean-Christophe Charlier, Humberto Terrones, and Mauricio Terrones. Identification of individual and few layers of WS_2 using raman spectroscopy. *Scientific Reports*, 3(1), 2013.

[162] Luojun Du, Jian Tang, Jing Liang, Mengzhou Liao, Zhiyan Jia, Qinghua Zhang, Yanchong Zhao, Rong Yang, Dongxia Shi, Lin Gu, Jianyong Xiang, Kaihui Liu, Zhipei Sun, and Guangyu Zhang. Giant valley coherence at room temperature in 3R WS_2 with broken inversion symmetry. *Research*, 2019, 2019.

[163] Xiaoze Liu, Tal Galfsky, Zheng Sun, Fengnian Xia, Erh-chen Lin, Yi-Hsien Lee, Stéphane Kéna-Cohen, and Vinod M Menon. Strong light–matter coupling in two-dimensional atomic crystals. *Nature Photonics*, 9(1):30–34, 2015.

[164] Wenjing Liu, Bumsu Lee, Carl H Naylor, Ho-Seok Ee, Joohee Park, AT Charlie Johnson, and Ritesh Agarwal. Strong exciton–plasmon coupling in MoS_2 coupled with plasmonic lattice. *Nano Letters*, 16(2):1262–1269, 2016.

[165] Kin Fai Mak and Jie Shan. Photonics and optoelectronics of 2D semiconductor transition metal dichalcogenides. *Nature Photonics*, 10(4):216–226, 2016.